2019-07-01

Development of a Simplified Performance-Based Procedure for Assessment of Post-Liquefaction Settlement Using the Cone Penetration Test

Jingwen He
Brigham Young University

Development of a Simplified Performance-Based Procedure for Assessment of Post-Liquefaction Settlement Using the Cone Penetration Test

Jingwen He

A thesis submitted to the faculty of
Brigham Young University
in partial fulfillment of the requirements for the degree of

Master of Science

Kevin W. Franke, Chair
Kyle M. Rollins
Gus P. Williams

Department of Civil and Environmental Engineering

Brigham Young University

ABSTRACT

Development of a Simplified Performance-Based Procedure for
Assessment of Post-Liquefaction Settlement
Using the Cone Penetration Test

Jingwen He
Department of Civil and Environmental Engineering, BYU
Master of Science

Earthquake-induced liquefaction can cause severe damage to infrastructure is a serious concern in civil engineering practice. Post-liquefaction settlement is one of the common effects of liquefaction. The ability to predict and quantify post-liquefaction free-field settlement is a crucial part of seismic design. Many approaches have been developed during the past 50 years to perform liquefaction hazard analysis. The performance-based earthquake engineering (PBEE) framework developed by the Pacific Earthquake Engineering Research (PEER) center is a probabilistic framework that can provide a more accurate and complete seismic hazard analysis than other traditional methods. However, the PBEE framework is not widely used in routine projects due to its complexity.

Previous researches have been performed to develop simplified performance-based procedures that can combine the simplicity of a traditional method and the accuracy of the full performance-based method. Unfortunately, these simplified performance-based procedures are only available for SPT. With the increase use of CPT, there is a need to develop simplified performance-based procedures for CPT. This study develops simplified performance-based procedures for the assessment of post-liquefaction free-field settlement for CPT, using the Boulanger and Idriss (2014) and the Ku et al. (2012) triggering models. The Juang et al. (2013) model, which is a probabilistic version of the Ishihara and Yoshimine (1992) model, is used in this study to performance free-field settlement calculations. The simplified procedure is based on the idea of liquefaction reference parameter maps. Reference values obtained from these parameter maps are then adjusted, using correction equations, to site-specific conditions.

This study presents the deviations of the correction equations for the simplified performance-based procedure. The simplified procedure will then be validated in which 18 cities across the United States are analyzed using both the simplified procedure and the full performance-based procedure. The simplified performance-based procedure is shown to reasonably estimate the results of the full performance-based procedure. Finally, a study is performed to compare the accuracy and consistency of the simplified performance-based and the conventional pseudo-probabilistic procedures. The simplified performance-based procedure is found to provide better approximations of the full performance-based procedure with more consistency and precision.

Keywords: liquefaction, settlement, performance-based earthquake engineering, probabilistic, CPT, map-based procedure

ACKNOWLEDGEMENTS

I thank Dr. Franke for his guidance and knowledge, which helped me through this incredible course. I am grateful that he was always understanding and patient when I was sick and pregnant with my child. I also thank my committee members, Dr. Rollins and Dr. Williams, who have been so kind to me. Thank you for providing your insights and being great examples.

I thank all of my lab mates: Donald Anderson, Alex Corob, Heidi Dacayanan, Delila Lasson, and Reed Reimschussel. They all have been great friends and have provided help with my research. A special thank you to Jenny Blonquist, who has gone through the ups and downs with me and provided me help when I needed technical support. I thank Mikayla Hatch, Tyler Coutu and Alex Arnt for building *CPTLiquefy*, which has performed all the complex computations for my research. I also want to thank all those who have participated in the SPT research projects, especially Braden Error; their works have been valuable resources for me.

Funding for this research was provided by Connecticut, Oregon, South Carolina, and Utah Department of Transportation. I gratefully acknowledge this support. This support was crucial in the development of the procedures presented herein.

Finally, I thank my husband, Kevin, who has been supporting my dreams and career with all his love and deed. Even while working on his own research project, he sacrificed his time to help me create VBA codes to compile all the data. Thank you for taking care of Sarah when I needed time to focus on my thesis. This would not have been possible without your support.

TABLE OF CONTENTS

LIST OF TABLES

LIST OF FIGURES

1 INTRODUCTION

Earthquake-induced liquefaction can cause significant damage to structures, infrastructure and lifelines. However, liquefaction phenomenon did not receive much attention until 1964, when the Alaska earthquake and Niigata, Japan earthquake, both caused massive liquefaction-induced damages. One of the common effects of liquefaction is free-field post-liquefaction settlement, where the soil sublayers are densified during and after seismic loading. Settlement of the ground surface can lead to cracking, distortion, and tilting of the structures. These effects may not be life threating, but they can cause tremendous economic losses. To minimize potential losses, engineers and researchers are consistently seeking better methods to predict free-field post-liquefaction settlement. One of these methods, performance-based earthquake engineering (PBEE), has gained popularity because of its ability to incorporate and account for uncertainties. Although the PBEE framework allows engineers to perform more complete, accurate, and objective seismic hazard analysis, the method is not commonly used in routine design projects due to its complexity.

Not until the past decade have researchers been able to simplify the performance-based procedure into an approximation approach. Mayfield et al. (2010) first suggested the framework for a simplified performance-based procedure for evaluating liquefaction initiation using the Cetin et al. (2004) triggering model. Since then, various simplified performance-based procedures have been developed at BYU to perform liquefaction calculations for SPT. However, no simplified performance-based procedures have been developed to for CPT.

The goal of this study is to develop a simplified performance-based procedure to perform post-liquefaction settlement calculations for CPT so that the benefits of a full performance-based procedure may become more accessible to practicing engineers. The simplified performance-based procedure is founded on the idea of liquefaction reference parameter maps. Full performance-based analyses are used to create these reference parameter maps, whose values can then be adjusted to reflect site-specific conditions using the correction equations derived in this study. The simplified volumetric strain can be quickly calculated with the appropriate liquefaction parameter map, site-specific soil data, and the correction equations, which can be programed into a spreadsheet.

This study presents the derivations of the simplified performance-based procedures using both of the Boulanger and Idriss (2014) and the Ku et al. (2012) triggering models. The Juang et al. (2013) model, which is the probabilistic version of the Ishihara and Yoshimine (1992) volumetric strain model, is used to perform settlement calculations. The development of the liquefaction reference parameter maps will be described. A validation study will then be presented to validate the effectiveness of the proposed simplified performance-based procedures. Finally, a comparison study will be performed to compare the accuracy of the simplified performance-based procedure and the traditional pseudo-probabilistic procedure.

2 EARTHQUAKES AND GROUND MOTIONS

The study of liquefaction hazards requires fundamental knowledge of earthquakes, which is a result of the release of energy within the earth's crust. Ground motions generated from an earthquake can develop undrained loadings on soils, which may potentially lead to liquefaction phenomenon. Because soil liquefaction is the focus of this study, the mechanics of liquefaction will be discussed in greater depth in Chapter 3. This chapter will provide some fundamental knowledge of earthquakes, including earthquake size, ground motion parameters, earthquake prediction, and seismic hazard analysis.

2.1 Earthquake Size

The oldest method of measuring earthquake size is earthquake intensity. Earthquake intensity is measured by the observed damage and human reaction at a certain location during and after the earthquake. Earthquake intensities are usually determined from effects on people, human structures and natural environments (USGS). Historical records may also be used to study past earthquakes. Different intensity scales are being used in different countries or regions. The one currently used in the United States is the Modified Mercalli Index (MMI), which can be found in Figure 2-1.

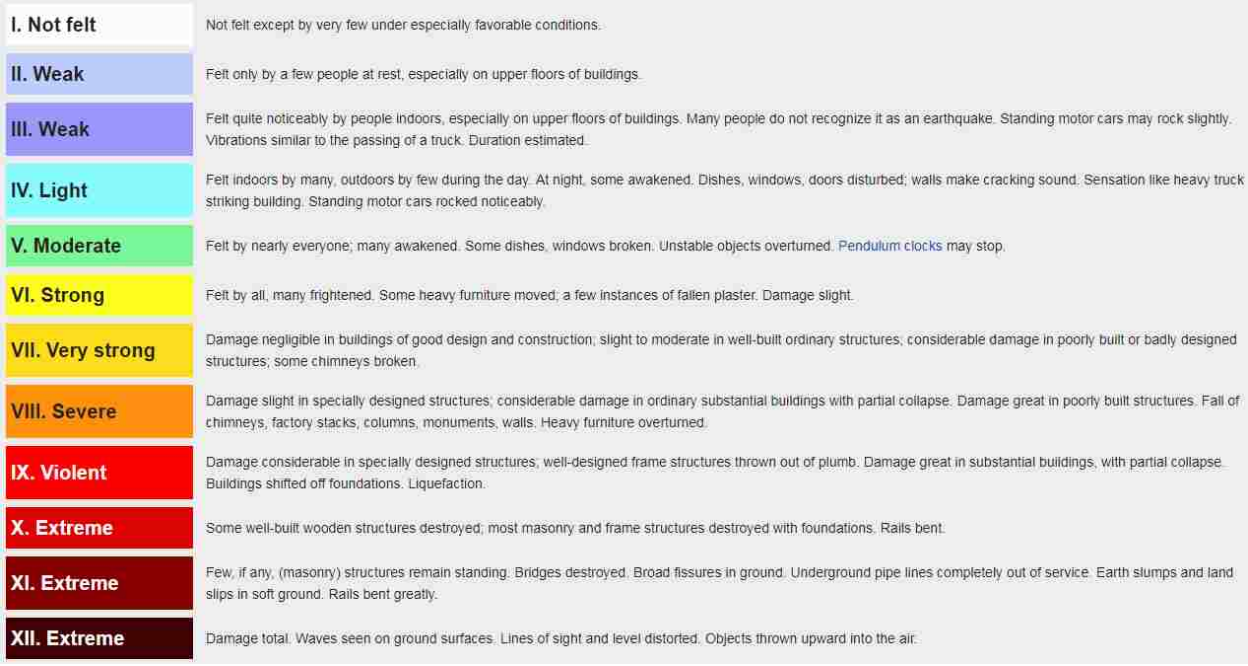

Figure 2-1: Modified Mercalli Intensity Scale (USGS, 1931).

Isoseismal maps are made by plotting earthquake intensities at different locations and drawing contours of equal intensities. While earthquake intensities are useful for approximating earthquake levels, comparing earthquake effects in different regions, and estimating earthquake losses, earthquake intensities are measured subjectively. The creation of these isoseismal maps are also very time consuming.

With the development of modern instrumentation, a more objective measure called earthquake magnitude became possible. Earthquake magnitudes are objective and quantitative measurements of earthquake size, and they are made based on the characteristics of earthquake shaking. Some of these earthquake magnitudes are Richter local magnitude, surface wave magnitude, and body wave magnitude. Unfortunately, none of these magnitudes account for a phenomenon called saturation, which says that ground shaking characteristics do not increase at the same rate as the increase of the total amount of energy released during an earthquake. Kanamori

(1977) and Hanks and Kanamori (1979) suggested using moment magnitude, which does not depend on ground shaking levels, and consequently does not saturate. Moment magnitude is based on seismic moment and it is calculated as:

$$M_w = \frac{\log M_0}{1.5} - 10.7 \tag{2-1}$$

where M_0 is the seismic moment in dyne-cm, which is given by:

$$M_0 = \mu A \overline{D} \tag{2-2}$$

where μ is the rupture strength of the material along the fault, A the rupture area, and $\overline{D}$ the average amount of slip.

2.2 Ground Motion Parameters

Ground motion parameters are also essential to study the characteristics of earthquakes. These parameters can be grouped into three main categories: (1) amplitude parameters, (2) frequency content, or (3) duration of ground motions. Because of the complexity of earthquake ground motions, it is nearly impossible to characterize an earthquake with one single ground motion parameter (Jennings, 1985; Joyner & Boore, 1988).

2.2.1 Time Histories

Ground motion parameters are often derived from earthquake time histories. On a time history, the motion parameter, which can be acceleration, velocity or displacement is plotted against time. A time history provides a visual image of the ground shaking and its effects in respect of time. Examples of acceleration, velocity and displacement time histories are shown in Figure

2-2. Note that the Gilroy No. 1 (rock) site experienced a higher peak acceleration, but the Gilroy No. 2 (soil) site experienced a longer time of ground acceleration and demonstrated higher velocity and displacement.

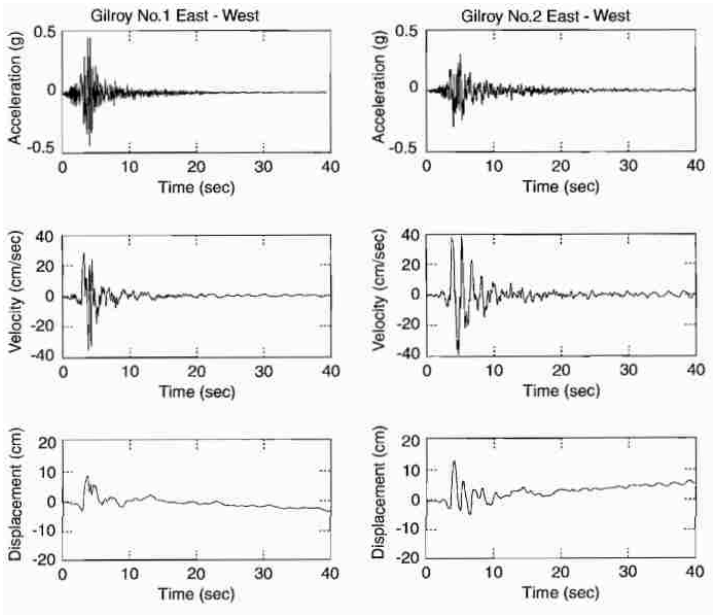

Figure 2-2: Acceleration, Velocity, and Displacement Time Histories for the E-W Components of the Gilroy No. 1 (rock) and Gilroy No.2 (soil) Strong Motion Records (Kramer, 1996).

2.2.2 Amplitude Parameters

Amplitude is the y-value on the time history plot. Among all amplitudes, peak ground acceleration (PGA), which is the maximum ground acceleration that occurred during earthquake shaking at a location, is widely used within earthquake engineering. It can be decomposed into two components: peak horizontal acceleration (PHA) and peak vertical acceleration (PVA). PVA is often determined to be 2/3 of PHA (Campbell, 1985; Abrahamson and Litehiser, 1989); but sometimes PVA can also be large; a PVA of 1.74 g was recorded for the 1979 Imperial Valley earthquake (Kramer, 1996).

2.2.3 Frequency Content Parameters

The damage caused by an earthquake can also be affected by the frequencies of the earthquake. The frequency content describes how the amplitude of an earthquake is distributed among different frequencies (Kramer, 1996). Ground motion spectra are often used to describe frequency content.

Fourier spectrum is one of the common ground motion spectra, which decomposes the ground motion into different frequencies that comprise it. A Fourier amplitude spectrum is a plot of Fourier amplitude versus frequency, which shows how the amplitude of the earthquake is distributed with respect to the frequency. Figure 2-3 presents the Fourier amplitude spectra for the E-W components of the Gilroy No. 1 (rock) and Gilroy No. 2 (soil) strong motion records.

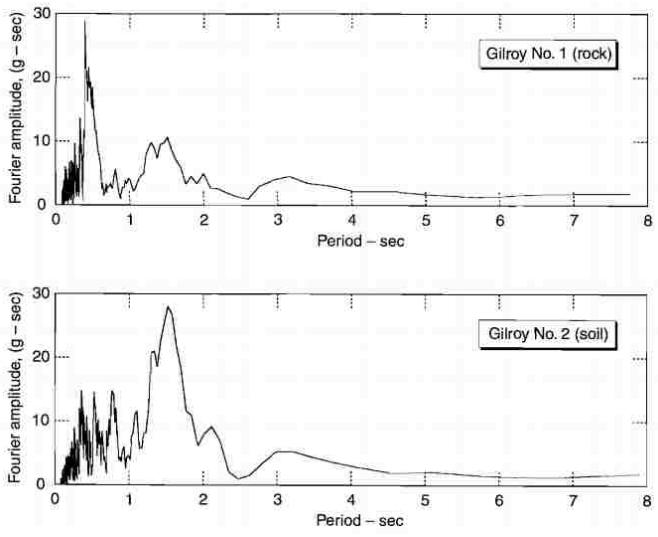

Figure 2-3: Fourier amplitude spectra for the E-W components of the Gilroy No. 1 (rock) and Gilroy No. 2 (Soil) strong motion records (Kramer, 1996).

Fourier amplitude spectra is a useful tool for earthquake engineering. From the Figure 2-3, engineers can predict that the critical frequency for the Gilroy No. 1 (rock) site is about 0.4s. To avoid resonance, where the natural period of the structure is same as the frequency of the shaking,

engineers could design the height and the mass distribution of the structure so that it does not have a natural period around 0.4s.

Response spectrum is also used extensively in earthquake engineering, which is a plot of the maximum response of many single-degree-of-freedom (SDOF) systems under a particular input motion and the natural frequency of the SDOF system. The computed response spectra for Gilroy No. 1 (rock) and Gilroy No. 2 (soil) are illustrated in Figure 2-4.

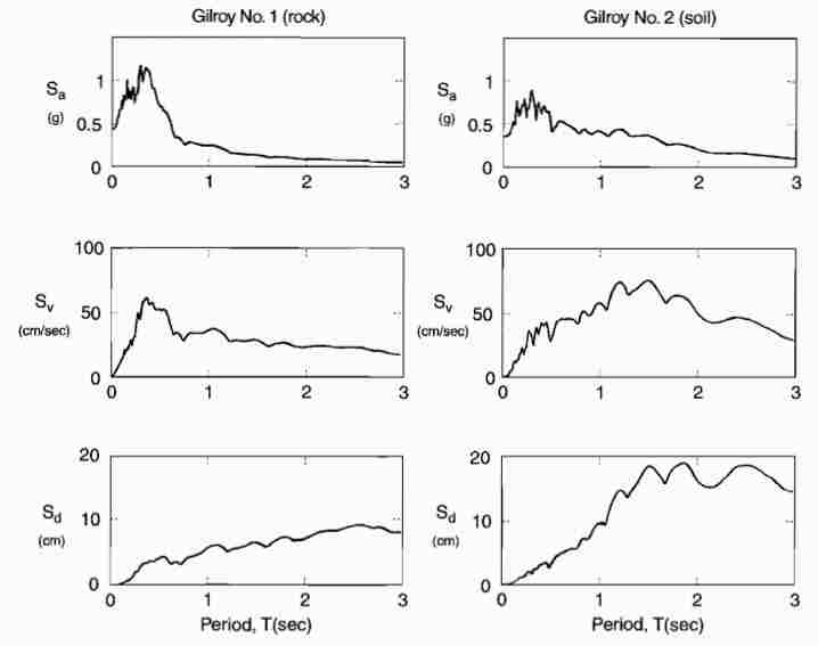

Figure 2-4: Response spetra (5% damping) for Gilroy No. 1 (rock) and Gilroy No. 2 (soil) strong motion records (Kramer, 1996).

With a response spectrum, engineers can easily identify the maximum acceleration, velocity, or displacement that a SDOF system experiences under the ground motion, knowing the natural frequency of the system. Even though response spectra only represent the maximum response of some structures, they are important and useful tools for characterizing strong ground motions.

2.2.4 Duration

The duration of an earthquake is also an important characteristic of strong ground motions. Soil weakening due to softening and reduction of strength can occur as excess pore pressure is generated during long duration of seismic loading. The duration of an earthquake is related to the time that is required to release the strain energy that has been built up in the fault that ruptures. Generally, engineers are only interested in the duration that strong ground motion is generated, which can be at a threshold acceleration at 0.05 g, which is called bracketed duration (Bolt, 1969). Figure 2-5 provides an example of the bracketed duration measurement.

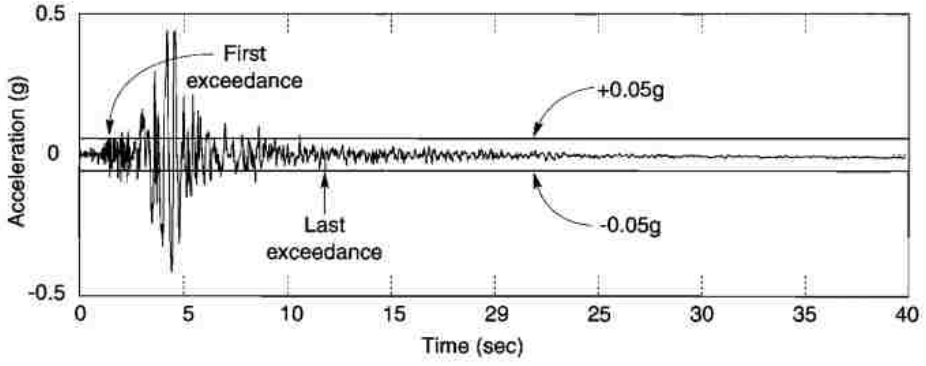

Figure 2-5: Bracketed Duration Measurement for the Gilroy No. 1 (rock) Ground Motions (Kramer, 1996).

2.3 Predicting Ground Motion Parameters

Engineers need to predict future ground motion parameters to design for earthquake-resistant structures. To address this need, predictive relationships called attenuation relationships or ground motion prediction equations (GMPEs) have been developed based on recorded time histories. For example, Campbell (1981), used worldwide data to develop an attenuation relationship to predict mean PHA for sites within 50 km of the fault rupture in magnitude 5.0 to 7.7 earthquakes. Youngs et al. (1988) used strong-motion measurements obtained on rock from 60

earthquakes and numerical simulations of $M_w \geq 8$ earthquakes to develop a subduction zone attenuation relationship for PHA. Joyner and Boore (1988) used strong-motion records from earthquakes of $5.0 \leq M_w \leq 7.7$ to develop the attenuation relationship for PHV.

With the increase of new earthquake data, a more unified database and updated relationships were needed. In 2008, the Pacific Earthquake Engineering Research center (PEER) released five new models (Abrahamson and Silva (2008); Boore and Atkinson (2008); Cambell and Bozorgnia (2008); Chiou and Youngs (2008); Idriss (2008)) that were developed from the same set of data. These new relationships were called the Next Generation Attenuation (NGA) relationships. Since then, a few ground motion research projects had been conducted by PEER.

In 2013, with the new ground motion data released by PEER, the NGA models were updated to NGA West2 (Ancheta et al., 2014), which was developed specially for the western United States and other high seismicity areas. The NGA West2 project included models for shallow crustal earthquakes in active tectonic regions and addressed several key issues in ground-motion seismic hazard (Abrahamson et al., 2014; Boore et al. 2014; Campbell and Bozorgnia, 2014; Chiou and Youngs, 2014; Idriss, 2014).

In 2014, the NGA East database was created for the Central and Eastern North-American (CENA) region. The NGA-East project developed a new ground motion characterization (GMC) model for CENA region (Goulet, 2014).

To address an outstanding type of seismic source - subduction zone, the NGA-Sub projected was created in 2012. The NGA-Sub project began by collecting empirical data from subduction earthquakes around the world including the 2011 Tohoku Earthquake in Japan and the 2010 Chile Earthquake, as well as earthquake ground motion recordings from many other historic

subduction earthquakes. The NGA-Sub database was developed in 2017 (Kishida, 2017). The new set of GMPEs will be released as the project progresses.

2.4 Seismic Hazard Analysis

Engineers perform seismic hazard analyses to estimate strong ground motions at a particular site using attenuation relationships. Seismic hazard analyses can be done deterministic (i.e., assuming a single earthquake scenario) or probabilistic (i.e., uncertainties in earthquake size, location and time of occurrence are explicitly considered) (Kramer, 1996).

2.4.1 Deterministic Seismic Hazard Analysis

Deterministic seismic hazard analysis (DSHA) involves the selection of one earthquake scenario that will produce the largest ground motion parameters. A typical DSHA procedure was summarized by Reiter (1990) and goes as follows:

1. Identification and characterization of all earthquake sources cable of producing significant ground motion at the site.
2. Selection of a source-to-site distance parameter for each source zone. Because a shorter distance generally results in a higher predicted ground motion, the shortest distance is typically selected. This distance may be the epicentral distance or the hypocentral distance, depending on the predictive relationship that is being used.
3. Selection of the controlling earthquake, which produces the strongest ground shaking. Earthquakes identified in step 1 are assumed to occur at the distances identified in step 2.
4. The hazard at the site is formally defined, usually in terms of the ground motion parameters (e.g., peak acceleration, peak velocity, response spectrum ordinates). (Kramer, 1996).

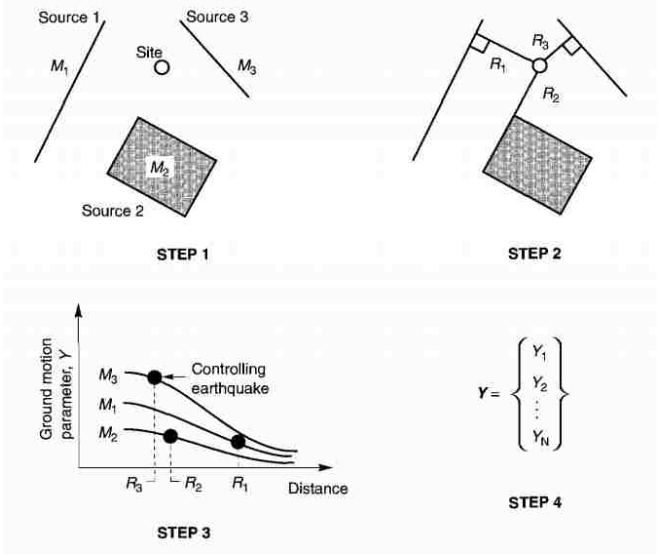

Figure 2-6: Four Steps of a Deterministic Seismic Hazard Analysis (Kramer, 1996).

The four steps of DSHA are illustrated in Figure 2-6. The DSHA provides a straightforward solution intended to represent the credible worst case scenario or the level of shaking that it could actually produce. Moreover, the DSHA involves subjective decisions from different stakeholders who may have different goals and considerations on the same parameter. This can lead to very different results of the analysis. Therefore, even though DSHA is easy to use, it does not account for uncertainties in an objective manner.

2.4.2 Probabilistic Seismic Hazard Analysis

Probabilistic seismic hazard analysis (PSHA) provides a framework that allows the uncertainties of earthquake size, location and rate of occurrence to be identified and qualified. This procedure requires understanding of some basic concepts of probabilistic theory. Same as the DSHA, Reiter (1990) summarized it in a four-step procedure:

1. Identification and characterization of all earthquake sources. For PSHA, the probability distribution of potential rupture locations also needs to be characterized. In most cases,

uniform probabilities are assigned to each source assuming that earthquakes have the same likelihood to occur at each source zone.

2. Characterization of seismicity or temporal distribution of earthquake recurrence. To characterize the seismicity of each source zone, a recurrence relationship, which specifies the average rate at which an earthquake of some size will be exceeded, is used. This allows a range of magnitude events to be considered, instead of only considering the largest event.
3. Determination of the ground motion produced at the site by earthquakes of any possible size occurring at any possible point in each source zone using predictive relationships. The uncertainty inherent in the attenuation relationship is also considered in a PSHA.
4. The uncertainties in earthquake size, location, rate of occurrence and ground motion parameter prediction are combined to obtain the probability that the ground motion parameter will be exceeded during a particular period (Kramer, 1996).

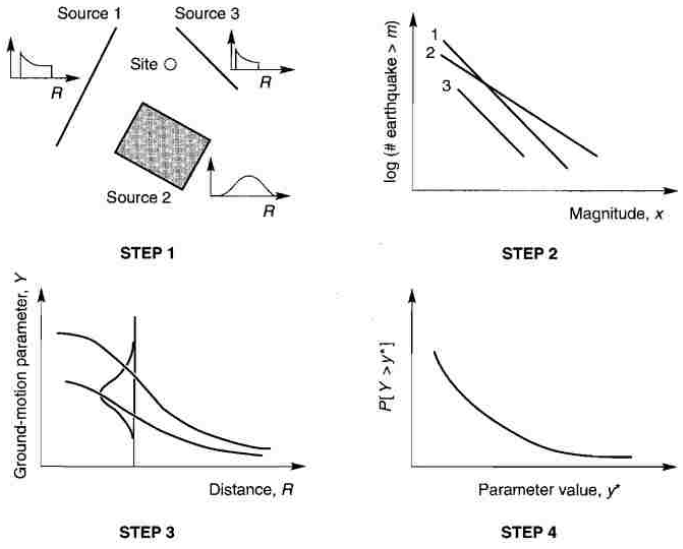

Figure 2-7: Four Steps of a Probabilistic Seismic Hazard Analysis (Kramer, 1996).

The four steps of PSHA are illustrated in Figure 2-7. The PSHA allows engineers to perform seismic hazard analysis in a more objective and complete manner, but it requires careful characterization of earthquake sources and calculation of probabilities in each of the steps. Knowledge of probabilistic theory and use of special software may be needed to perform this analysis.

2.5 Chapter Summary

Ground motion parameters are useful tools for understanding and quantifying seismic loading, which for crucial to predicting seismic hazards. Over the years, various attenuation relationships have been developed to estimate ground motion parameters for future earthquake events. These calculations can be done either deterministically (DSHA) or probabilistically (PSHA).

3 SOIL LIQUEFACTION

3.1 Introduction of Liquefaction

The term liquefaction was first used in 1953 by Mogami and Kubo, and historically it has been used to describe the phenomena that involve soil deformations caused by monotonic, transient, or repeated disturbance of saturated cohesionless soils under undrained conditions (Kramer, 1996). However, liquefaction phenomenon has not been closely studied until the past 50 years, when the Alaska earthquake and Niigata, Japan earthquake happened in 1964, both causing massive liquefaction-induced ground deformations and damage.

During an earthquake, the generation of excess pore water pressure leads to the decrease of effective stress. Eventually, the excess pore pressure can become so large that the effective stress becomes zero. In another words, soil particles are not confined by any stresses and can flow freely like a fluid. Liquefaction can manifest in two ways: flow liquefaction and cyclic mobility. Flow liquefaction is rare in the field, but can cause severe damage. Cyclic mobility occurs more commonly, but the effects can vary from insignificant to tremendous. Because understanding of liquefaction is the foundation for this study, the remaining sections of this chapter will discuss liquefaction susceptibility, liquefaction initiation and liquefaction effects.

3.2 Liquefaction Susceptibility

Because not all soils can liquefy, the first step of liquefaction hazard analysis is to evaluate the susceptibility of the soil. If the soil is not susceptible, no liquefaction hazard analysis is needed. On the contrary, if the soil is susceptible, liquefaction hazard analysis is essential to assess potential liquefaction effects. There are four main criteria to help judge liquefaction susceptibility: historical criteria, geologic criteria, compositional criteria and state criteria.

3.2.1 Historic Criteria

Study of liquefaction case histories have shown that liquefaction often occurs at the same location that soil and groundwater conditions have not changed (Youd, 1984). Thus historical liquefaction events can be an indication that a site is susceptible to liquefaction during future earthquakes.

Field investigations also show that liquefaction often occurs within a particular distance of the seismic source (Kramer, 1996). Ambraseys (1988) was able to use a worldwide data to discover the relationship between epicentral distance of sites at which liquefaction has been observed and moment magnitude for shallow earthquakes, as shown in Figure 3-1.

Figure 3-1 Shows that as earthquake magnitude increases, distance to which liquefaction may be found increases dramatically. Even though liquefaction may still occur at greater distance, this relationship provides an estimation of possible liquefaction locations.

3.2.2 Geologic Criteria

The depositional environment, hydrological environment and age of the soil deposit can all contribute to liquefaction susceptibility (Kramer, 1996).

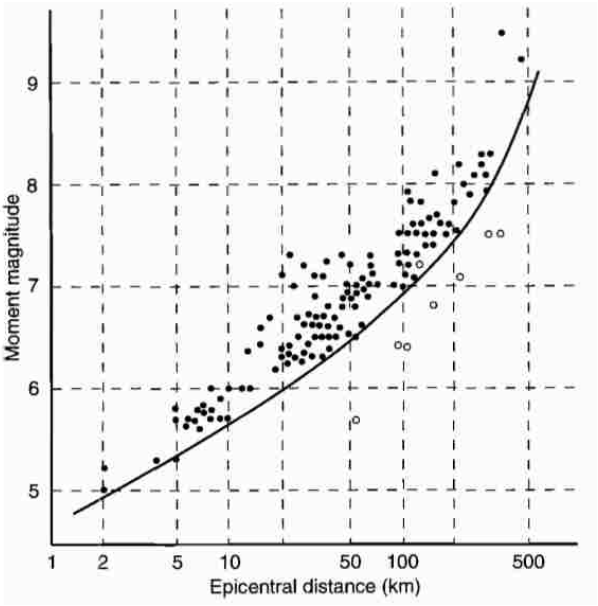

Figure 3-1: Relationship between Limiting Epicentral Distance of Sites at Which Liquefaction Has Been Observed and Moment Magnitude for Shallow Earthquakes (Ambraseys, 1988).

When a soil consists of uniform grain size and is deposited in loose state, it has a high liquefaction susceptibility (Youd & Hoose, 1977). Therefore, fluvial deposits, colluvial deposits and Aeolian deposits are more susceptible to liquefaction when they are saturated. Newer deposits also have a higher susceptibility compared to old deposits.

Because liquefaction only happens to saturated soils (Kramer, 1996), the depth of groundwater also influence liquefaction susceptibility. Liquefaction is often observed at sites where watertable is close the ground surface.

Anthropogenic soil deposits that are not well compacted are also susceptible to liquefaction. Thus, hydraulic fill dams and mine tailing piles, in which soils are loosely deposited, may be subjected to liquefaction hazards.

3.2.3 Compositional Criteria

Because liquefaction results from the buildup of excess pore pressure, which is a consequence of soil densification, high volume change potential can lead to high liquefaction susceptibility. Particle size, shape and gradation are all characteristics that can affect volume change potential.

Investigations of case histories have shown that not only sands are susceptible to liquefaction; both fine-grained soils, like silts (Ishihara, 1984; Ishihara, 1985), and coarse-grained soils, like gravels are also susceptible to liquefaction. Coarse silts with bulky particle shape are susceptible to liquefaction because they have low plasticity and cohesion, which lead to high volume change potential. Boulanger and Idriss (2005) categorized fine-grain soils into two behavior groups: sand-like and clay-like. Sand-like fines have low placidity and they are more susceptible to liquefaction (Boulanger and Idriss, 2005). For coarse-grained soils, liquefaction of gravels also has been observed both in the field and in the laboratory (Coulter and Migliaccio, 1966; Chang, 1978; Wong, 1984; Youd et al.,1985; Yegian et al., 1994; Wong et al. 1975; Evans and Seed, 1987).

Particle shape is another factor that can affect liquefaction susceptibility. Because rounded particles can be densified more easily, soils with rounded shapes are more susceptible to liquefaction compared to soils with angular shapes (Kramer, 1996).

Lastly, gradation can also influence soil liquefaction. For well-graded soils, the small particles can fill up the voids between the larger particles, which can result in a smaller volume change under undrained condition. Consequently, poorly-graded soils are more susceptible to soil liquefaction (Kramer, 1996).

3.2.4 State Criteria

Even if a soil meets all the criteria that have been discussed, a soil may still not liquefy. The initiation of liquefaction depends on the initial stress state of the soil, which determines if a soil will dilate or contract under earthquake loading. Because excess pore pressure is generated when an undrained soil is trying to contract, the study of the initial state of a soil is necessary. To better understand state criteria, concepts of critical void ratio (CVR), steady state line (SSL) and state parameter will be reviewed.

Casagrande (1936) first introduced the concept of CVR after performing drained, strain-controlled triaxial tests on initially loose and dense sand specimens. It was observed that the loose specimen contracted and the dense specimen first contracted but then quickly started to dilate during shearing. Eventually, both specimens ended up approaching the same relative density at large strains. The void ratio at which constant density is found is called critical void ratio, e_c, as shown in Figure 3-2.

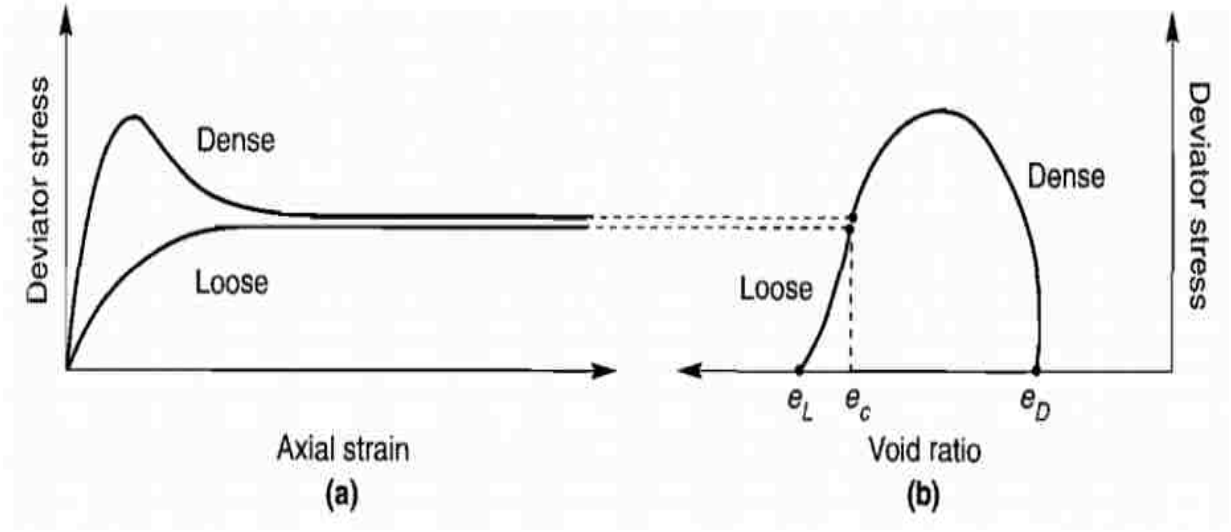

Figure 3-2: (a) Stress-Strain and (b) Stress-Void Ratio Curves for Loose and Dense Sands at the Same Effective Confining Pressure (Kramer, 1996).

Casagrande (1936) also found that this CVR is related to the confining pressure. Under different effective confining pressures, a different CVR was measured. By plotting different effective confining pressures and the corresponding CVR, a CVR line can be defined. Casagrande suggested that, under undrained conditions, soils that are plotted above the CVR line have the tendency to contract, which will generate positive pore pressure. Soils plotted below the CVR line have the tendency to dilate, which will generate negative pore pressure. This concept is illustrated in Figure 3-3. Thus, soils with initial state plotted above the CVR were contractive and are considered susceptible to liquefaction, and soils plotted below the CVR line were dilative and are not susceptible.

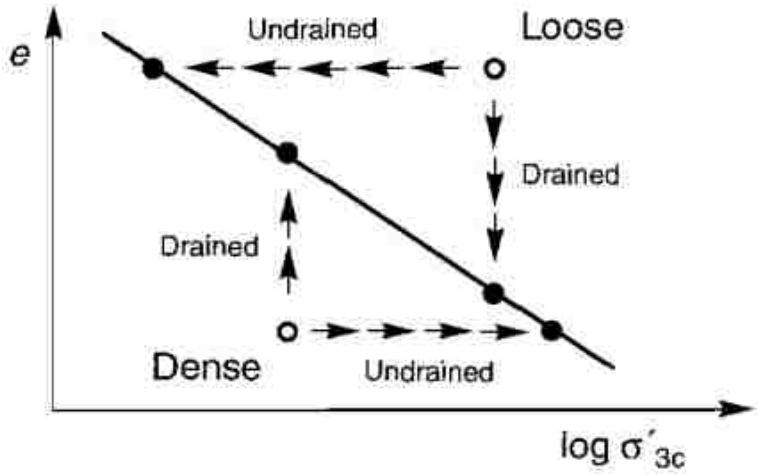

Figure 3-3: Behavior of Initially Loose and Dense Specimens under Drained and Undrained Conditions for Logarithmic Effective Confining Pressure Scales (Kramer, 1996).

Questions were posted against this theory in 1936 when the Fort Peck Dam in Montana failed due to a static flow liquefaction failure. Investigation showed that the soils at the site plotted below the CVR line, which should be in the nonsusceptible zone. This question was later answered by Casagrande's student, Castro.

Castro performed experiments on three different types of specimens: very loose specimens, dense specimens and intermediate density specimens. The behavior of the specimens shows that there is a unique relationship between void ratio and the effective confining pressure at large strains. The state in which the soil flowed continuously under constant shear stress and constant effective confining pressure at constant volume and constant velocity was defined as the *steady state of deformation* (Castro and Poulos, 1977; Poulos 1981). The line that describes the relationship between void ratio and effective confining pressure in the steady state of deformation is called the *steady-state line* (SSL). Generally, the SSL is a three-dimensional curve in *e*-σ'-τ space, as shown in Figure 3-4, but it can also be projected onto a plane of constant τ, constant σ' or constant density (*e* = constant).

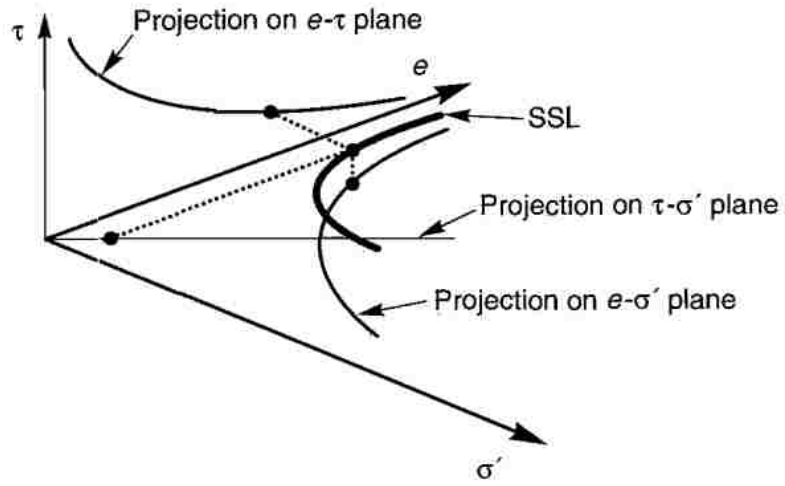

Figure 3-4: Three-dimensional Steady-state Line (Kramer, 1996).

The SSL is a useful tool for determining liquefaction susceptibility. For flow liquefaction, a soil is not susceptible if it plots below the SSL; and it is susceptible to liquefaction if it plots above the SSL and the static shear stress exceeds its steady state strength, as shown in Figure 3-5. However, for cyclic mobility, liquefaction can occur to soils plot either above or below the SSL.

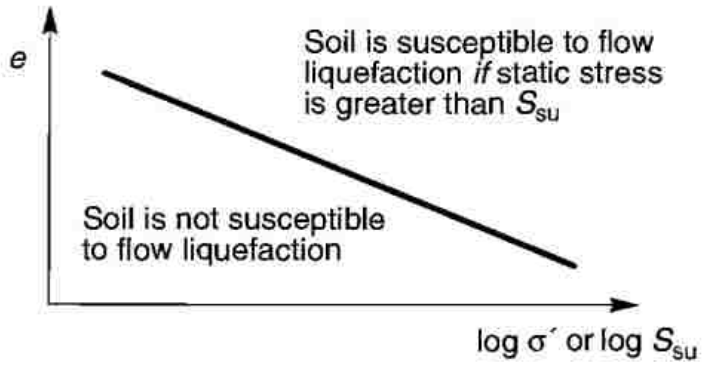

Figure 3-5: State Criteria for Flow Liquefaction Susceptibility (Kramer, 1996).

The SSL provides a limited way to determine liquefaction susceptibility with absolute density, because a soil with the same density can be susceptible to flow liquefaction under high effective confining pressure, but not susceptible under low effective confining pressure. To address this issue, Been & Jefferies (1985) suggested a term called *state parameter*, which is defined as:

$$\Psi = e - e_{ss} \tag{3-1}$$

where e_{ss} is the void ratio of the steady state line at the effective confining pressure of interest. When the state parameter is positive, the soil behaves in a contractive manner, which may be susceptible to flow liquefaction. When the state parameter is negative, the soil behaves in a dilative manner, which is not susceptible to flow liquefaction.

3.3 Liquefaction Initiation

Liquefaction will not occur until the loading is large enough to initiate. Evaluation of that loading is essential to liquefaction hazard analysis. Because cyclic mobility and flow liquefaction are initiated in different ways, the initiation of liquefaction for cyclic mobility and flow liquefaction will be discussed separately. A commonly used procedure for evaluating liquefaction initiation will then be presented.

3.3.1 Flow Liquefaction Surface

Hanzawa et al. (1979) first suggested that the effective stress conditions at which strain-softening behavior occurs can be described in stress path ($p' - q$) space. Consider the five specimens in Figure 3-6 , specimens A and B are below the SSL and they are dillative. Specimens C, D, and E are above the SSL and are all contractive. Flow liquefaction triggers at the peak of stress paths C, D, and E.

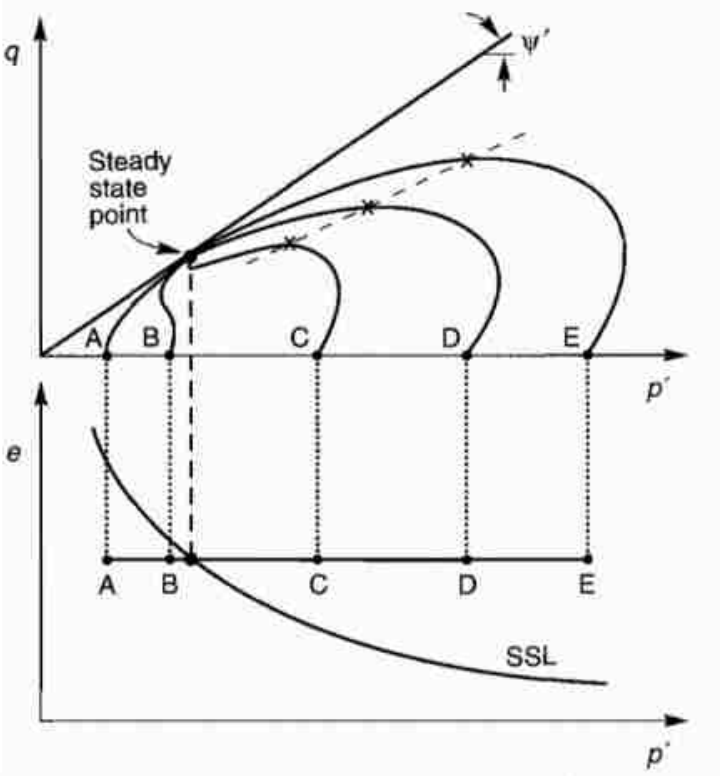

Figure 3-6: Response of Five Specimens Isotropically Consolidated to the Same Initial Void Ratio at Different Initial Effective Confining Pressures (Kramer, 1996).

Hanzawa et al (1979), Vaid and Chern (1983) have shown that the locus of points describing the effective stress conditions at the initiation of flow liquefaction is a straight line that projects through the origin of the stress path (Kramer, 1996). These points are used to define *flow liquefaction surface* (FLS). Because flow liquefaction cannot occur when the stress path is below

the steady state point, Vaid and Chern (1983) suggested that the FLS should be truncated at that level, as shown in Figure 3-7.

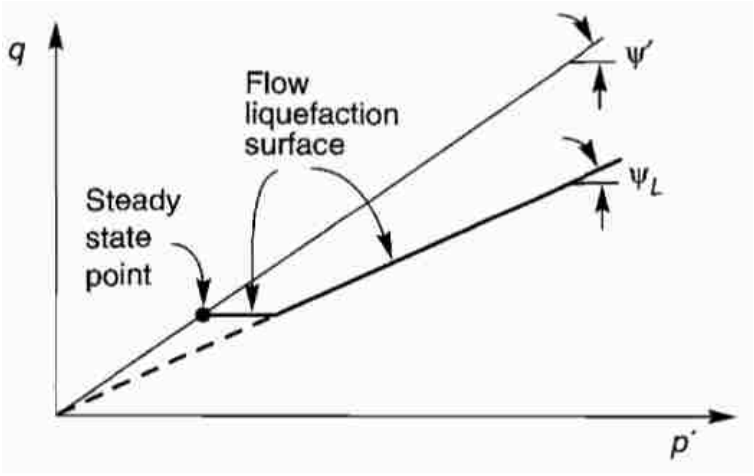

Figure 3-7: Flow Liquefaction Surface in Stress Path Space (Kramer, 1996).

3.3.2 Flow Liquefaction

Flow liquefaction only occurs when the shear stress required for static equilibrium is greater than the steady-state strength. This liquefaction phenomenon occurs in two stages. During the first stage, the stress path is pushed from its initial position to FLS by the accumulation of excess pore pressure. During the second stage, strain-softening is driven by the stresses required for static equilibrium. The second step is inevitable once the stress path reaches the FLS under undrained, stress-controlled conditions. Soils whose initial stress states plot in the shaded area shown in Figure 3-8 are susceptible to flow liquefaction. If the initial stress state is close to the FLS, flow liquefaction may be triggered more easily because only a small amount of excess pore pressure is needed to push the stress path to the FLS (Kramer and Seed, 1988).

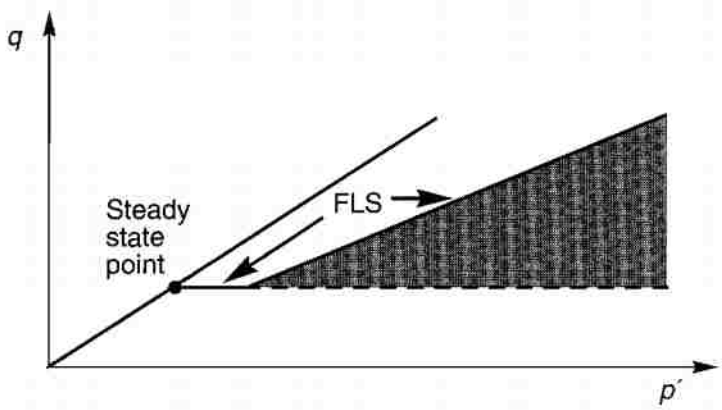

Figure 3-8: Zone of Susceptibility to Flow Liquefaction (Kramer, 1996).

3.3.3 Cyclic Mobility

Cyclic mobility can occur when the static shear stress is smaller than the steady state shear strength. Soils whose initial stress states plot in the shaded area shown in Figure 3-9 are susceptible to cyclic mobility.

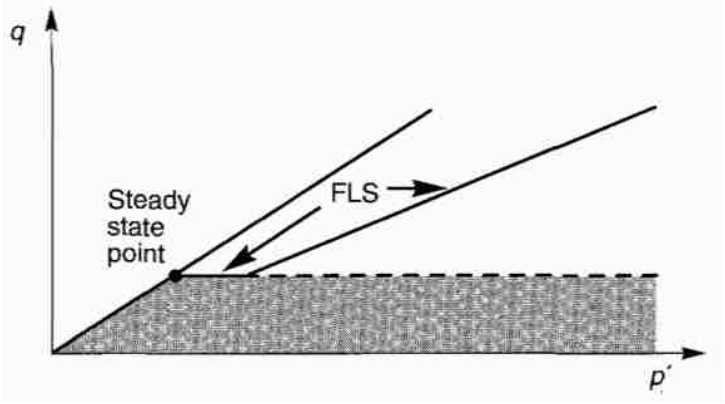

Figure 3-9: Zone of Susceptibility to Cyclic Mobility (Kramer, 1996).

There are three combinations of initial states and cyclic loading that can cause cyclic mobility (Kramer, 1996). The first condition is depicted in Figure 3-10(a), where there is no shear

stress reversal in the loading or exceedance of steady-state strength (i.e., $\tau_{static} - \tau_{cyc} > 0$ and $\tau_{static} + \tau_{cyc} < S_{su}$). In this case, the stress path moves to the left until it reaches the drained failure envelope. The extra loading cycles moves the stress path up and down the envelope. With the significant decrease of effective confining stress and reduction of stiffness, permanent strains are developed within each cycle.

The second condition is depicted in Figure 3-10(b), where the steady state strength is exceeded momentarily, but there is no stress reversal (i.e. $\tau_{static} - \tau_{cyc} > 0$ and $\tau_{static} + \tau_{cyc} > S_{su}$). As the stress path moves to the left, soil experiences instantaneous instability when the stress path touches the FLS. Large permanent strains may develop temporarily during these periods.

The third condition is depicted in Figure 3-10(c), where there is shear reversal and exceedance of steady-state strength (i.e., $\tau_{static} - \tau_{cyc} < 0$ and $\tau_{static} + \tau_{cyc} > S_{su}$). In this case, the shear stress alternates between compression and extension. The stress path moves quickly due to the rapid buildup of excess pore pressure, and eventually oscillates along the failure envelop. Each time the stress path passes through the origin, the soil mass is in a temporary state of zero effective stress. This is referred to as *initial liquefaction* (Seed & Lee, 1966). Significant permanent strains are developed during this state.

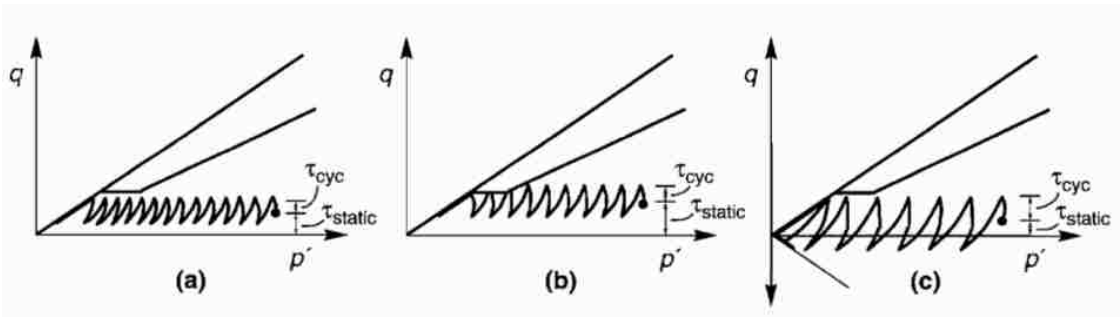

Figure 3-10: Three Cases of Cyclic Mobility.

3.4 CPT-Based Evaluation of Liquefaction Initiation

With the understanding of liquefaction susceptibility and liquefaction initiation, liquefaction triggering can be quantified by calculating a factor of safety against liquefaction (FS_L) or the probability of liquefaction (P_L).

FS_L is the ratio of the soil's ability to resist liquefaction to the earthquake loading, which can also be written as:

$$FS = \frac{capacity}{demend} = \frac{CRR}{CSR} \tag{3-2}$$

where *CRR* represents the cyclic resistance ratio and *CSR* represents cyclic stress ratio. A factor of safety smaller than 1 indicates that the soil's ability to resist liquefaction is smaller than the seismic loading demand from the earthquake. Soil liquefaction will be triggered.

In a cyclic stress approach, earthquake loading is represented by *CSR* and is quantified using cyclic shear stresses normalized by the vertical effective stress, as shown below:

$$CSR = \frac{\tau_{cyc}}{\sigma_v'} \tag{3-3}$$

where τ_{cyc} is the shear stress amplitude in a soil layer from a ground motion of interest, and it can be calculated numerically with site response analysis. Seed and Idriss (1971) developed a "simplified" procedure to estimate τ_{cyc} for level (or gently sloping) sites as:

$$\tau_{cyc} = 0.65 \frac{a_{\max}}{g} \sigma_v r_d \tag{3-4}$$

where $a_{\max}$ is the peak ground surface acceleration, *g* is the acceleration of gravity, σ_v is the total vertical stress, and r_d is a stress reduction factor at the depth of interest. Seed and Idriss (1971)

concluded that the cyclic shear stress was 65% of the maximum shear stress from a time history, and the "simplified" equation for *CSR* can be written as:

$$CSR = 0.65 \frac{a_{\max}}{g} \frac{\sigma_v}{\sigma'_v} (r_d) \tag{3-5}$$

Soil resistance to liquefaction is represented by *CRR*, which is the cyclic shear stress resistance, τ_{res}, normalized by vertical effective stress and can be expressed as:

$$CRR = \frac{\tau_{res}}{\sigma'_v} \tag{3-6}$$

The *CRR* is estimated using laboratory methods and is generally obtained by correlation to in-situ test results. For a CPT-based procedure, *CRR* can be represented by proxy using the normalized equivalent clean sand CPT resistance (q_{c1Ncs}). Because different correlations between *CRR* and q_{c1Ncs} are used in different triggering models, these relationships will be discussed in greater details in the next sections.

Many triggering models have been developed over the years, but this study will only focus on the Boulanger and Idriss (2014) model and the Ku et al. (2012) model, as they are the most widely used probabilistic models for CPT. Each of these models is explained in detail below.

3.4.1 Boulanger and Idriss (2014) Triggering Model

Many CPT-based liquefaction triggering procedures have been developed since the 1980s. Some of these procedures include Zhou (1980), Seed and Idriss (1981), Suzuki et al (1995, 1997), Robertson and Wride (1997,1998), and Idriss and Boulanger (2004,2008). With the increase of high-quality CPT case histories, Boulanger and Idriss (2014) updated their case history database to include earthquakes up through 2011. The Boulanger and Idriss (2014) model follows the

framework of the Boulanger and Idriss (2008) model, but it provides updated liquefaction triggering correlations using the new case history database. A probabilistic version of the CPT-based triggering procedure is also presented in the 2014 publication. A complete procedure of the Boulanger and Idriss (2014) is provided below.

3.4.1.1 Cyclic Stress Ratio (CSR)

Boulanger and Idrss (2008, 2010) developed a deterministic liquefaction triggering model using the following to estimate *CSR*:

$$CSR = 0.65 \frac{a_{\max}}{g} \frac{\sigma_v}{\sigma'_v} (r_d) \frac{1}{MSF} \frac{1}{K_\sigma} \tag{3-7}$$

where k_d is the overburden correction factor, and MSF is the magnitude scaling factor.

Boulanger and Idriss (2014) suggests that the magnitude scaling factor, *MSF*, is calculated as:

$$MSF = 1 + (MSF_{\max} - 1)(8.64 \exp(\frac{-M}{4}) - 1.325) \tag{3-8}$$

$$MSF_{\max} = 1.09 + (\frac{q_{c1Ncs}}{180})^3 \leq 2.2 \tag{3-9}$$

where M is the moment magnitude of the earthquake and q_{c1Ncs} is the corrected cone tip resistance obtained from the previous calculations.

The equations of Golesorkhi (1989) are used in the Boulanger and Idriss procedure to compute the shear stress reduction coefficient, r_d :

$$r_d = \exp[\alpha(z) + \beta(z) * \mathrm{M}] \tag{3-10}$$

$$\alpha(Z) = -1.012 - 1.126 \sin(\frac{z}{11.73} + 5.133) \tag{3-11}$$

$$\beta(z) = 0.106 + 0.118\sin(\frac{z}{11.28} + 5.142) \tag{3-12}$$

where z = depth below the ground surface in meters and the arguments inside the sin terms are in radians, *M* is the moment magnitude of the earthquake.

The overburden correction factor, K_σ, is calculated using the procedure developed by Boulanger (2003):

$$K_\sigma = 1 - C_\sigma \ln(\frac{\sigma_v^{'}}{P_a}) \le 1.1 \tag{3-13}$$

$$C_\sigma = \frac{1}{37.3 - 8.27(q_{c1Ncs})^{0.264}} \le 0.3 \tag{3-14}$$

The coefficient C_σ is limited to a maximum value of 0.3 by restricting $q_{c1Ncs} \le 211$ and $(N_1)_{60cs} \le 37$.

3.4.1.2 Cyclic Resistance Ratio (CRR)

The procedure begins with the iterative calculation for q_{c1Ncs} as follows:

$$q_{c1N} = C_N \frac{q_c}{P_a} \tag{3-15}$$

where q_c is the CPT cone tip resistance, P_a is atmospheric pressure, and C_N is the overburden correction factor, which can be calculated as:

$$C_N = (\frac{P_a}{\sigma'_v})^m \le 1.7 \tag{3-16}$$

where σ'_v is the vertical effective stress and m is calculated as:

$$m = 1.338 - 0.249(q_{c1Ncs})^{0.264} \tag{3-17}$$

and where $(q_{caN})_{cs}$ is limited between 21 and 254, and can be calculated as:

$$q_{c1Ncs} = q_{c1N} + \Delta q_{c1N} \tag{3-18}$$

Δq_{c1N} is the fines content adjustment factor, and is calculated as:

$$\Delta q_{c1N} = (11.9 + \frac{q_{c1N}}{14.6}) \exp(1.63 - \frac{9.7}{FC+2} - (\frac{15.7}{FC+0.01})^2) \tag{3-19}$$

where FC is the percentage of fines within the soil. Idriss and Boulanger suggest that *FC* should be calculated as:

$$FC = 80(I_c + C_{FC}) - 137 \quad 0\% \le \text{FC} \le 100\% \tag{3-20}$$

where I_c is the soil behavior type index calculated using the Robertson and Wride procedure, which is presented in Section 3.4.2, Equations (3-27) through (3-31), and C_{FC} is a regressing fitting parameter that can be adjusted based on site-specific data when available and can be calibrated to site specific data by regressing I_c against FC using the equation:

$$I_c = (FC + 137)/80 - C_{FC} \tag{3-21}$$

To begin the iteration, a seed value of q_{c1Ncs} is defined and Equations (3-15) through (3-19) are iterated until the change of q_{c1Ncs} is less than 0.5. The final calculated q_{c1Ncs} is the value that will be used to obtain *CRR*. The correlation between *CRR* and q_{c1Ncs} is as shown:

$$CRR_{M=7.5,\sigma'_{vo}=1atm} = \exp(\frac{q_{c1Ncs}}{113} + (\frac{q_{c1Ncs}}{1000})^2 - (\frac{q_{c1Ncs}}{140})^3 + (\frac{q_{c1Ncs}}{137})^4 - 2.8) \tag{3-22}$$

With the calculated values and case history data, liquefaction triggering curve for the Idriss and Boulanger deterministic model is presented in Figure 3-11. The *CRR* curve represents a boundary between cases that are expected to liquefy and those which are not expected to liquefy.

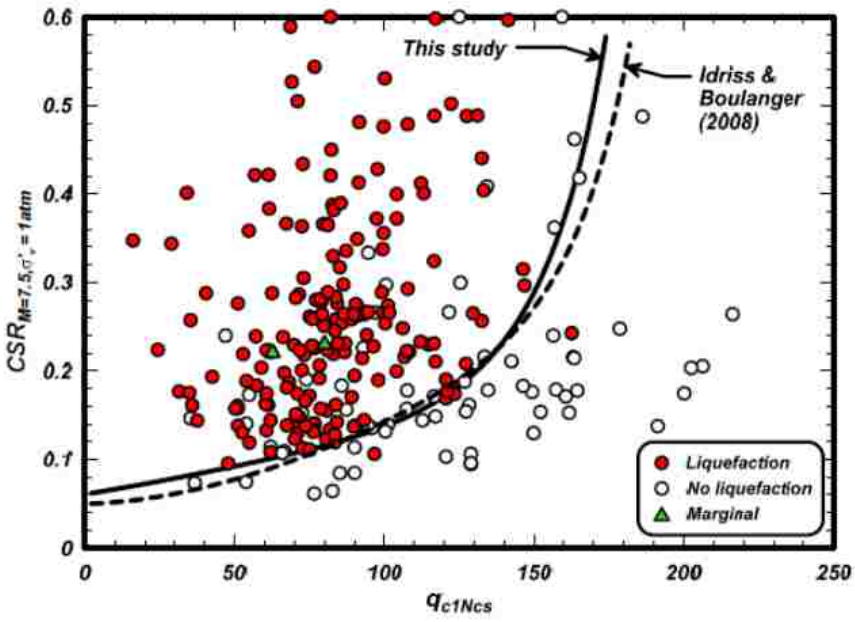

Figure 3-11: CRR Curves and Liquefaction Curves for the Deterministic Case History Database (Idriss and Boulanger, 2014).

3.4.1.3 Factor of Safety (FS_L) and Probability of Liquefaction (P_L)

Now, FS_L can be calculated using Equation (3-2).

Boulanger and Idriss (2014) also developed a probabilistic version of their liquefaction triggering procedure. P_L is expressed as:

$$\left(P_L\right) = \Phi\left[-\frac{\left(\frac{q_{c1Ncs}}{113}\right)+\left(\frac{q_{c1Ncs}}{1000}\right)^2-\left(\frac{q_{c1Ncs}}{140}\right)^3+\left(\frac{q_{c1Ncs}}{137}\right)^4-2.60-\ln\left(CSR_{M=7.5,\sigma'_v=1atm}\right)}{\sigma_{\ln(R)}}\right] \quad (3\text{-}23)$$

where Φ is the standard normal cumulative distribution function, q_{c1Ncs} is the clean sand corrected CPT resistance, $CSR_{M=7.5,\sigma'_v=1atm}$ is the corrected CSR value for the standardized magnitude and overburden pressure, and $\sigma_{\ln(R)}$ is the computed model uncertainty, which is 0.2 for their model. The liquefaction triggering P_L curves are shown in Figure 3-12.

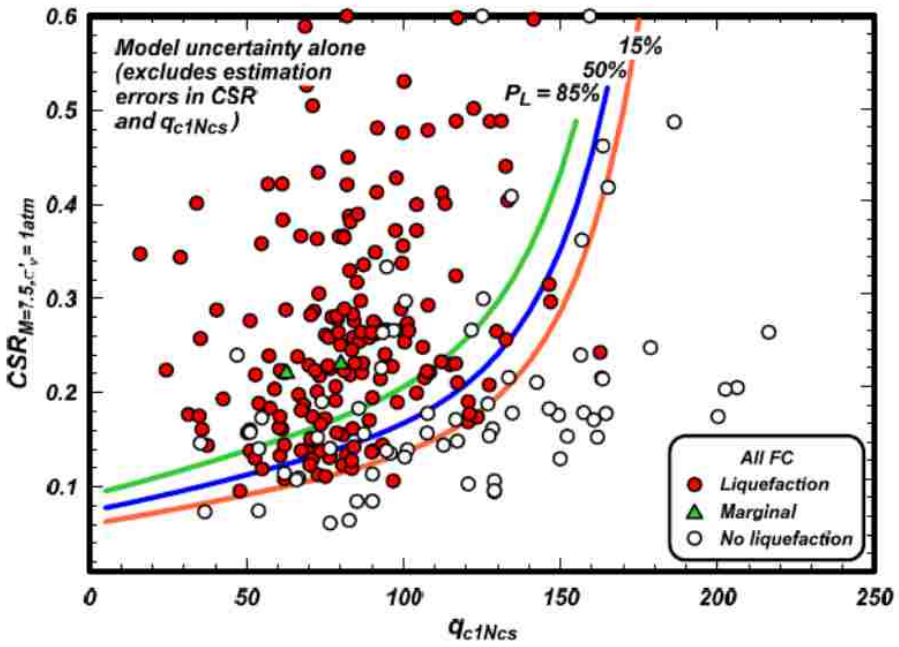

Figure 3-12: Liquefaction Triggering P_L Curves Compared to Case History Data (Idriss and Boulanger, 2014).

3.4.2 Ku et al. (2012) Triggering Model

The Ku et al. (2012) triggering model is the probabilistic version of the Robertson and Wride (2009) deterministic triggering model. The Ku et al. (2012) procedure also begins with the iterative calculation of q_{c1Ncs}, which is referred to as $Q_{tn,cs}$ for this model.

3.4.2.1 Cyclic Stress Ratio (CSR)

With the Ku et al. (2012) model, CSR is also calculated using Equation (3-7), but *MSF*, r_d, and K_σ are computed differently than with the Boulanger and Idriss (2014) model. In the Ku et al. (2012) and Robertson and Wride (2009) models, *MSF* is calculated using Youd et al. (2001) as:

$$MSF = \frac{10^{2.24}}{M_w^{2.56}} \tag{3-24}$$

r_d is based on the work of Liao and Whitman (1986) and Seed and Idriss (1971), and is computed as:

$$r_d = \begin{cases} 1.0 - 0.00765z & \text{for } z \le 9.15m \\ 1.174 - 0.0267z & \text{for } 9.15m < z \le 23m \\ 0.744 - 0.008z & \text{for } 23m < z \le 30m \\ 0.5 & \text{for } z > 30m \end{cases} \quad (3\text{-}25)$$

where z is the depth of interest in meters.

K_σ is calculated using the equation from Youd et al. (2001), as:

$$K_\sigma = \left(\frac{\sigma'_{vo}}{P_a}\right)^{(f-1)} \quad (3\text{-}26)$$

where f is the exponent that is a function of site conditions. The NCEER workshop further suggested that the value of f should be between 0.6 to 0.8 when soil densities are between 80 and 40 percent, respectively.

3.4.2.2 Cyclic Resistance Ratio (CRR)

To begin the iterative calculation, the stress component, n, is calculated as:

$$n = 0.381(I_c) + 0.05\left(\frac{\sigma'_v}{P_O}\right) - 0.15 \quad (3\text{-}27)$$

where I_c is the soil behavior index. Robertson (1990) found the correlation between I_c, q_c and f_s, which is summarized in the soil behavior chart (Jefferies and Davies, 1993; Robertson, 1990), as shown in Figure 3-13.

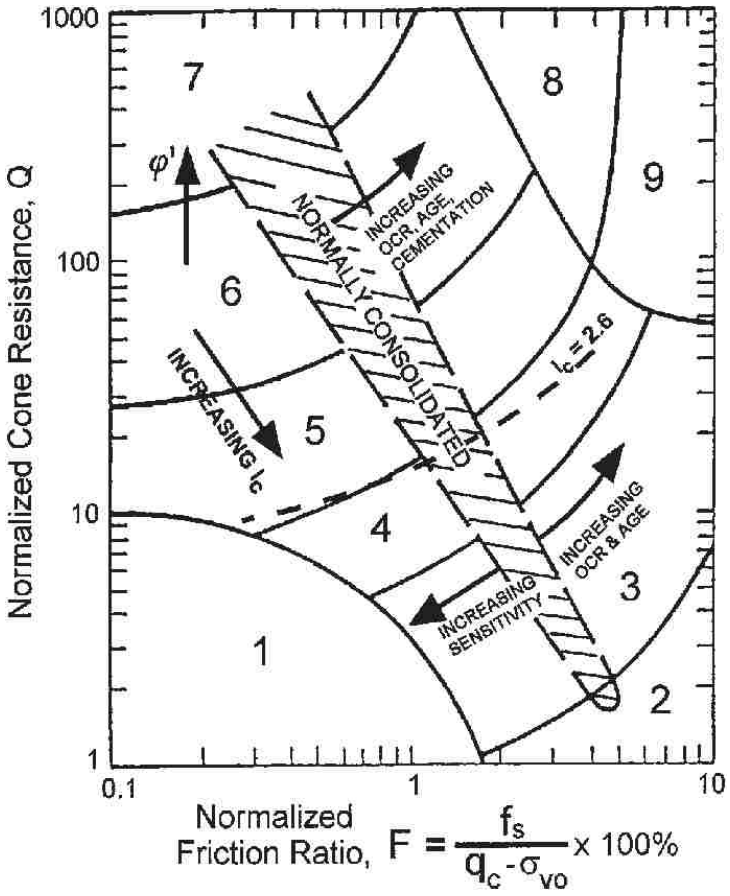

Figure 3-13: Normalized CPT Soil Behavior Type Chart (Robertson, 1990). Soil Types: 1, Sensitive, Fine Grained; 2, Peats; 3, Silty Clay to Clay; 4, Clayey Silt to Silty Clay; 5, Silty Sand to Sandy Silt; 6, Clean Sand to Silty Sand; 7, Gravelly Sand to Dense Sand; 8, Very Stiff Sand to Clayey Sand; 9, Very Stiff, Fine Grained.

n is then used to calculate the overburden stress correction factor, C_N, as:

$$C_N = (\frac{P_a}{\sigma_{vo}})^n < 2.0 \tag{3-28}$$

I_c is now calculated as:

$$I_c = [(3.47 - \log(Q_{tn}))^2 + (\log(F) + 1.22)^2]^{0.5} \tag{3-29}$$

where

$$Q_{tn} = (\frac{q_t - \sigma_{vo}}{P_a}) * C_N \tag{3-30}$$

and

$$F_r = \frac{f_s}{(q_t - \sigma_{vo})} * 100 \tag{3-31}$$

n is now re-calculated using this newly calculated I_c and Equation (3-27). This process is repeated until the change of n is smaller than 0.01, and the current values of I_c and Q_{tn} can be used to obtain $Q_{tn,cs}$ as shown:

$$Q_{tn,cs} = K_c * Q_{tn} \tag{3-32}$$

where K_c is calculated as:

$$K_c = \begin{Bmatrix} 1.0 & \text{if } I_c \le 1.64 \\ 5.58I_c^{\,3} - 0.403I_c^{\,4} - 21.63I_c^{\,2} + 33.75I_c - 17.88 & \text{if } 1.64 < I_c \le 2.50 \\ 6*10^{-7}(I_c)^{16.76} & \text{if } 2.50 < I_c < 2.70 \end{Bmatrix} \tag{3-33}$$

CRR can then be obtained using $Q_{tn,cs}$ as:

$$CRR = \begin{Bmatrix} 93(\frac{Q_{tn,cs}}{1000})^3 + 0.08 & \text{if } I_c < 2.70 \\ 0.053 * \mathrm{Q}_{tn} & \text{if } I_c \ge 2.70 \end{Bmatrix} \tag{3-34}$$

With the calculated values and case history data, liquefaction triggering curve for the Robertson and Wride (2009) deterministic model is presented in Figure 3-14.

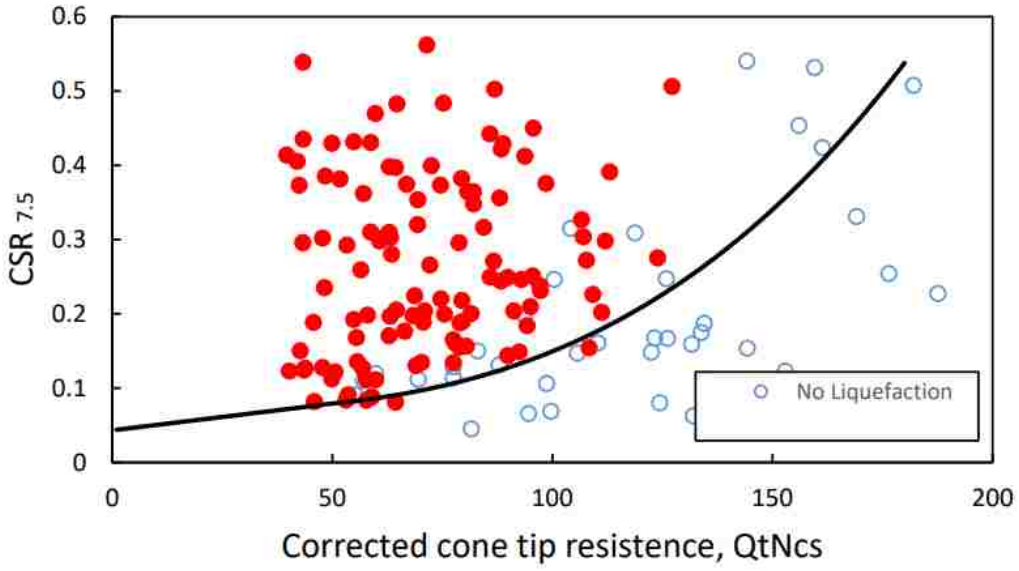

Figure 3-14: Robertson and Wride (2009) Liquefaction Triggering Curve with Case History Data Points.

3.4.2.3 Factor of Safety (FS_L) and Probability of Liquefaction (P_L)

FS_L can be computed using Equation (3-2). Alternatively, liquefaction triggering hazard can be expressed with P_L as:

$$P_L = 1 - \Phi\left[\frac{0.102 + \ln(FS_L)}{\sigma_m}\right] \tag{3-35}$$

where Φ is the standard normal cumulative distribution function, and σ_m is the model uncertainty equal to 0.276. The liquefaction triggering P_L curves are shown in Figure 3-15. The curve indicated by "RW" represents the Robertson and Wride (2009) deterministic triggering curve.

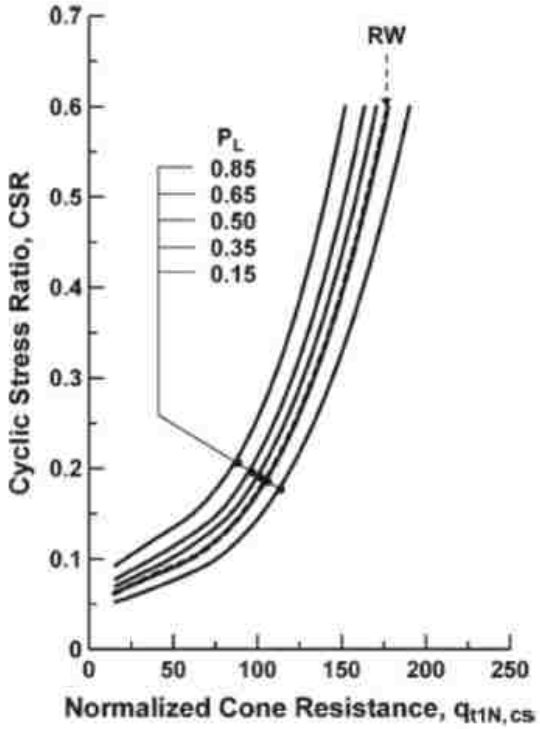

Figure 3-15: CRR Liquefaction Triggering Curves Based on PL (Ku et al., 2012).

3.5 Liquefaction Effects

Once the evaluation of liquefaction triggering is completed and triggering is predicted in the analysis, it is important to understand potential effects of liquefaction that may occur at the site. Liquefaction-induced effects can cause significant damage to infrastructure. Understanding and correctly predicting these effects will improve engineers' ability to minimize damage resulting from liquefaction.

3.5.1 Settlement

Soils tend to densify under earthquake shaking, and the densification of sublayers is manifested as settlement on the ground surface. Settlement occurs as the pore pressures dissipate

after an earthquake, which can happen from the end of to a day after the earthquake. When post-liquefaction settlement occurs, buildings may sink, tilt, or even tip over. Differential settlement, which occurs when structure settles unevenly, can cause more serious structural damage because of distortion applied to the structure. Figure 3-16 shows a picture of a tilted structure after the 1990 Luzon earthquake in Japan, where the left side of the ground has settled more than the right side.

Figure 3-16: Tilted Structure after the 1990 Luzon Earthquake in Japan (Orense, 2011).

Settlement of dry sands is controlled by the density of the sand, the amplitude of the cyclic shear strain in the sand, and the number of cycles of shear strain applied during the earthquake (Silver & Seed, 1971). Settlement of saturated sands is dependent on relative density and maximum shear strain (Kramer, 1996). Because post-liquefaction settlement is the focus of this study, greater details regarding settlement calculations will be discussed in chapter 4.

3.5.2 Lateral Spread

Lateral spread is the permanent horizontal movement of soil at a site due to liquefaction. Typically, a block of ground surface is broken off and will move on top of the liquefied soil

towards the toe of a slope or a free face. This movement can vary from a few centimeters to several meters. Similar to settlement, lateral spread can cause significant damage to infrastructure, especially bridges, railroad tracks and ports. Large cracks or fissures can also be formed in roadways, as shown in Figure 3-17.

Figure 3-17: Liquefaction and Lateral Spreading Induced Fissures in the Main East-West Highway between Siquerres and Puerto Limon (EERI, 2016).

3.5.3 Flow Failure

As mentioned previously, flow liquefaction is one of the most dangerous effects associated with liquefaction and can cause severe damage to the surrounding area. Flow failures occur when the shear stresses required to maintain static equilibrium are greater than the shear strength of the liquefied soil (Kramer, 1996). When flow failure is initiated, a massive volume of soil travels downslope like a fluid. The velocity of these flows can be significant.

3.5.4 Loss of Bearing Capacity

Liquefaction can also greatly reduce the shear strength of the liquefied soil, which will lead to the loss of bearing capacity. Buildings or structures supported by the soil may tip over or punch through the soil. Severe damage can occur to the footings or the embankments of overlying structures. Figure 3-18 shows apartment buildings in Niigata, Japan that experienced loss of bearing capacity during the 1964 earthquake.

Figure 3-18: Loss of Bearing Capacity due to Soil Liquefaction from Niigata, Japan 1964 Earthquake (Niigata Earthquake, 1964).

3.5.5 Sand Boils

Sand boils are often developed during liquefaction. During and after the earthquake shaking, excess pore water is commonly dissipated by travelling upwards to the ground surface. The velocity of these flows may be sufficient to carry sand particles through cracks and channels. Sand boils are formed when these sand particles are ejected on to the ground surface. They are useful indicators of the occurrence of liquefaction at a site (Kramer, 1996).

Figure 3-19: Sand Boils from 2011 Christchurch, New Zealand Earthquake (Musson, 2011).

3.6 Chapter Summary

Liquefaction occurs when excess pore pressures are generated in the soil under undrained conditions. Liquefaction susceptibility may be judged based on four criteria: historic criteria, geologic criteria, compositional criteria, and state criteria. Flow liquefaction and cyclic mobility are two different phenomena of soil liquefaction initiation. They depend on the initial stress state and the steady state strength of the soil. Boulanger and Idriss (2014) and Ku et al. (2012) are the two most commonly used methods to assess CPT-based liquefaction triggering in the field. When liquefaction occurs, settlement, lateral spread, flow failure, loss of bearing capacity, and sand boils are effects that can cause severe damage to a site.

4 POST-LIQUEFACTION SETTLEMENT

Earthquake-induced settlement is one of the common effects of soil liquefaction. When the ground surface settles unevenly, differential settlement occurs. Differential settlement often causes more severe damage to the area because of the cracks and distortions that are developed in the structure. It can also cause tilting of buildings, rupture of pipelines, and destruction of foundations. Though settlement is not directly life-threatening, large financial losses can be devastating to a city's economy. To minimize losses from post-liquefaction settlement and design resilient structures, engineers need to predict and quantify post-liquefaction settlement.

4.1 Understanding Settlement

Earthquake-induced settlement is a manifestation of the densification of the sublayers under shaking. For dry sand deposit, the shaking acts like a compaction mechanism, under which the soil particles are re-organized and densified. For saturated sand deposit, settlement occurs as earthquake-induced pore pressure dissipates (Kramer, 1996). In both cases, loosely deposited soil particles realign themselves into a denser and more stable state with smaller void spaces, as shown in Figure 4-1. This reduction in void space results in large volumetric strain, ε_v, which is the ratio between the change in volume of the soil (ΔV) and its original volume, as shown in Equation (4-1).

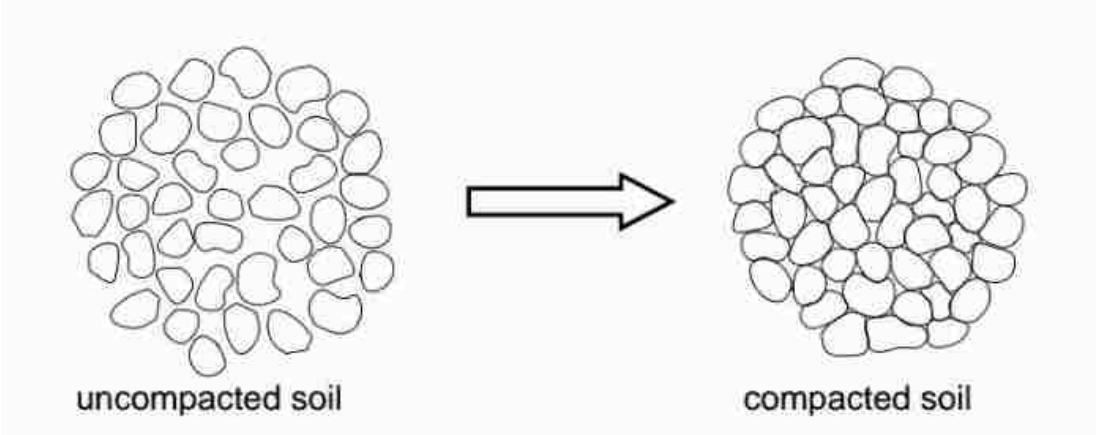

Figure 4-1: Densification of Soil (Bauer Maschinen GmbH, 2012).

$$\varepsilon_v = \frac{\Delta V}{V_0} \tag{4-1}$$

Thus, for the same original volume, a larger ε_v value indicates a bigger volume change. When there are different volumetric strains or varying liquefied soil thicknesses across a site, different amounts of settlement may be expected for each portion of the site, which leads to differential settlement.

It is important to know that other mechanisms can also impact the amount of settlement. For buildings with shallow foundations on liquefiable soil, high hydraulic gradients caused by earthquake loading can lead to the loss of material (piping), and cyclic inertial forces induced by soil-structure-interaction (SSI) can reduce the stiffness and strength of soils underneath the foundation. As a result, static bearing induced shearing of the soil, instead of volumetric strain, is an important factor in building settlement evaluation (Bray & Dashti, 2014). Research also shows that building height/width ratio, building weight, and 3D drainage have influence on building settlement (Dashti & Bray, 2010). Although these mechanisms are important, they are complex

and are not within the scoop of this study. All calculations and discussions only focus on free-field settlement, meaning no additional loading of structures or other situations is applied to the soil.

4.2 Free Field Post-Liquefaction Settlement Evaluation

Many empirical models have been developed over the years to predict post-liquefaction volumetric strain and settlement. Three of the most commonly used models are Cetin et al. (2009), Ishihara and Yoshimine (1992) and Juang et al. (2013), which is the probabilistic extension of the Ishihara and Yoshimine (1992) model. Because only Ishihara and Yoshimine (1992) and Juang et al. (2013) are CPT based settlement models, this thesis will focus on these two models.

4.2.1 Ishihara and Yoshimine (1992)

4.2.1.1 Development of the Ishihara and Yoshimine (1992) Strain Chart

Ishihara and Yoshimine (1992) performed several series of laboratory tests to study the volume change characteristic of sand under cyclic shear stress in undrained conditions.

At the University of Tokyo, sand samples were consolidated in the simple shear test device under a confining stress of 196 kN/m^2 and then subjected to horizontal, undrained shear stress with irregular time histories. Ishihara and Yoshimine found that the maximum shear strain experienced by sand during undrained cyclic loading is the most appropriate parameter that determines volume change during reconsolidation. Based on the work of Tatsuoka et al. (1984), Sasaki et al. (1982), and Kokusho et al. (1984), Figure 4-2 was developed to summarize the relationships between reconsolidation volume change and shear strain, for different soil densities.

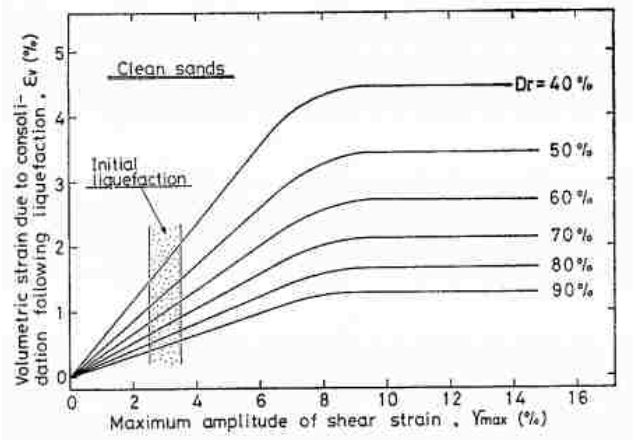

Figure 4-2: Summarized Relationships between Reconsolidation Volume Change and Shear Strain (Ishihara and Yoshimine, 1992).

Then, applying the work of Ishihara and Nagase (1988), a few series of simple shear tests were performed on Fuji river sand. Ishihara and Yoshimine used these test results to plot the maximum shear stress ratio against the maximum shear strain developed during the application of irregular loads. Because the factor of safety against liquefaction is a function of the maximum shear stress ratio, Ishihara and Yoshimine was able to develop a family of curves to describe the relationships between the FS_L and $\gamma_{\max}$, which is shown in Figure 4-3.

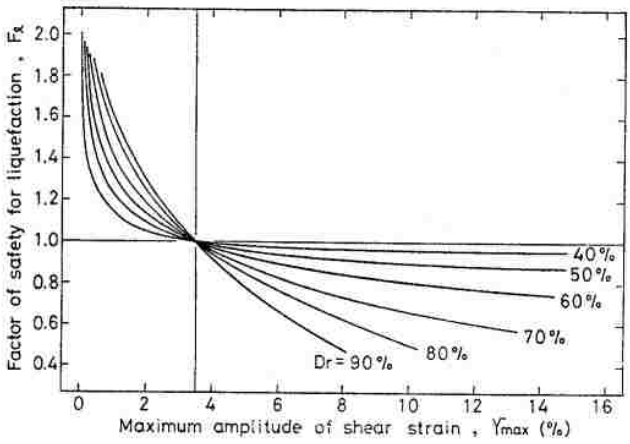

Figure 4-3: Summarized Relationship between the Factor of Safety and Maximum Shear Strain (Ishihara and Yoshimine, 1992).

By eliminating the parameter maximum shear strain, a family of relationships can be developed to relate factor of safety and volumetric strain, which is shown in Figure 4-4.

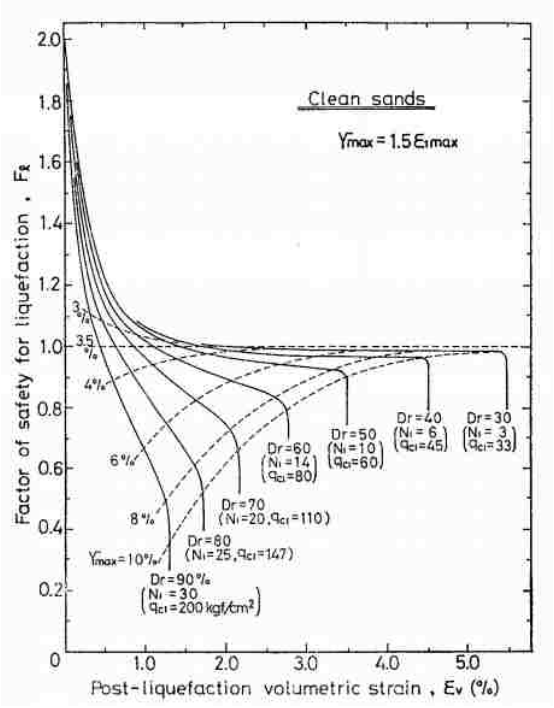

Figure 4-4: Chart for Determining Volumetric Strain as Functions of Factor of Safety (Ishihara and Yoshimine, 1992).

4.2.1.2 Ishihara and Yoshimine (1992) Procedure

With the relationships defined in Figure 4-4, Ishihara and Yoshimine were able to develop a deterministic procedure to estimate post-liquefaction settlement based on volumetric strains in liquefiable soils. They used this procedure to estimate settlements from the 1964 Niigata earthquake. The predicted values compared well to the observed settlements. It was shown that the proposed method is able to provide a rough estimate of settlements resulting from liquefaction during earthquakes. The Ishihara and Yoshimine (1992) procedure is given as follows.

1. Obtain FS_L for each sublayer using one of the triggering models (e.g., Boulanger and Idriss (2014), Ku et al. (2012)).

2. Calculate soil relative density, D_r, for each sublayer using equation from Tatsuoka et al. (1990).

$$D_r = -85 + 76 \log \frac{q_c}{\sqrt{\sigma_v'}} \tag{4-2}$$

where q_c is the cone tip resistance and σ_v' is the vertical effective stress.

3. Obtain volumetric strain, ε_v , for each sublayer, using the Ishihara and Yoshimine strain curves (Figure 4-4), FS_L, and D_r calculated previously.

4. Compute the predicted total ground surface settlement (S_p) by summating each sublayer's settlement, which is the product of volumetric strain multiplied by the sublayer's thickness, as shown below.

$$S_p = \sum_{i=1}^{N} \varepsilon_v \Delta Z_i \tag{4-3}$$

where ε_v is volumetric strain for the i^{th} layer, N is number of layers, and ΔZ_i is the i^{th} layer's thickness.

4.2.2 Juang et al. (2013)

Juang et al. (2013) suggested that there is a need to estimate the probability of exceeding a specified settlement because settlements on case histories are usually recorded as a range. To address this issue, Juang et al. (2013) developed a probabilistic method for calculating post-liquefaction settlement on the foundation of the Ishihara and Yoshimine (1992) procedure. The concepts of liquefaction probability, P_L , and maximum likelihood were used to obtain the proposed method.

Using the volumetric strain relationships that Ishihara and Yoshimine (1992) created, Juang et al. (2013) defined the relationships between ε_v, $q_{t1N,cs}$ and FS_L with the following equations through curving fitting.

$$\varepsilon_v(\%) = \left\{ \begin{array}{ll} 0 & \text{for} \quad \text{FS} \geq 2 \\ \min\left\{ \begin{array}{l} \dfrac{a_0 + a_1 \ln(q)}{\dfrac{1}{(2-FS)} - \left[a_2 + a_3 \ln(q)\right]} \\ b_0 + b_1 \ln(q) + b_2 \ln(q)^2 \end{array} \right\} & \text{for} \quad 2\text{-}\dfrac{1}{a_2 + a_3 \ln(q)} < FS < 2 \\ b_0 + b_1 \ln(q) + b_2 \ln(q)^2 & \text{for} \quad \text{FS} \leq 2\text{-}\dfrac{1}{a_2 + a_3 \ln(q)} \end{array} \right\} \tag{4-4}$$

where $a_0 = 0.3773$, $a_1 = -0.0337$, $a_2 = 1.5672$, $a_3 = -0.1833$, $b_0 = 28.45$, $b_1 = -9.3372$, $b_2 = 0.7975$ and $q = q_{t1Ncs}$.

Juang et al. (2013) also added two parameters IND_i and M to the settlement calculation equation, Equation (4-3), that was proposed by Ishihara and Yoshimine (1992). They proposed that the total post-liquefaction settlement should be calculated as:

$$S_p = M \sum_{i=1}^{N} \varepsilon_v \Delta Z_i IND_i \tag{4-5}$$

where ε_v is volumetric strain for the i^{th} layer, N is number of layers, IND_i represents the probability of liquefaction occurring, which is defined in Equation (4-6), M represents a modal bias correction factor, which will be discussed later in this section, and ΔZ_i is the i^{th} layer's thickness.

$$IND_i = P_L = 1 - \Phi\left\{ \frac{0.102 + \ln(FS_L)}{\sigma_{\ln(S)}} \right\} \tag{4-6}$$

where Φ represents the standard normal cumulative distribution function, and $\sigma_{ln(S)}$ represents the model uncertainty and is equal to 0.276 for their model.

The model bias factor, *M*, is used to correct the model error, and it is calibrated empirically using field observations. The maximum likelihood statistical method is used to perform the calibration. The database consists of m+n case histories of liquefaction-induced settlement, where m is the number of cases with a fixed settlement observation and n is the number of cases in which settlement is reported as a range. After applying the maximum likelihood principle, the model bias factor, or more precisely, μ_M and σ_M, are determined to be 1.0451 and 0.3175, respectively.

However, the Juang et al. (2013) model assumes that post-liquefaction settlement can be caused by both liquefied and non-liquefied soils, which may make sense in theory but not in practice. In practice, engineers rarely consider the contribution of non-liquefied soils to liquefaction settlement. Hatch (2017) has resolved the maximum likelihood equation developed by Juang et al. (2013) to neglect the possibility that non-liquefied layers contribute to post-liquefaction settlement, and the resulting values are 1.014 and 0.3313 for μ_M and σ_M. Any potential errors are accounted for in the larger standard deviation. These values will be used in this study.

4.3 Chapter Summary

Post-liquefaction settlement is a result of soil densification. Different methods have been developed over the years to predict post-liquefaction free field settlement. Ishihara and Yoshimine (1992) and Juang et al. (2013) are the most commonly used CPT based liquefaction settlement models. These two models are introduced in this chapter and will be applied to further calculations in this study.

5 PERFORMANCE-BASED EARTHQUAKE ENGINEERING

5.1 PBEE Framework

As discussed in Chapter 2, a PSHA allows engineers to perform seismic hazard analysis in a more complete manner due to its ability to account for the uncertainties of earthquake size, location and rate of occurrence. To implement PSHA into engineering design and improve seismic risk decision-making, the Pacific Earthquake Engineering Research Center (PEER) has developed the performance-based earthquake engineering (PBEE) framework. Instead of solely presenting earthquake risk in terms of factor of safety, the PBEE framework provides performance metrics that are more meaningful to various stakeholders.

Figure 5 1 is an example of the first-generation PBEE procedure, where relations are developed so that structural responses are represented by performance–oriented descriptions, such as Immediate Occupancy, Life Safety and Collapse Prevention. However, a few shortcomings were identified by engineers regarding this procedure, which included a lack of dynamic or nonlinear analysis methods, inconsistent relations defined between engineering demands and irrelevant data, and an inappropriate assessment for the overall system performance.

To address these challenges, Moehle and Deierlein (2004) developed a robust methodology for the PBEE, which breaks the process into logical elements that can be studied and analyzed in a consistent manner. This new framework begins with the definition of the first variable, Intensity Measure (IM), which should be defined in a probabilistic manner to capture seismic loading

information that can affect structural response. The next step is to determine Engineering Demand Parameters (EDP), which represent structural response in terms of deformations, accelerations, or other structural variables calculated using the input ground motions. Then Damage Measure (DM), which describes the physical resulting conditions of the structure, can be decided based on EDPs. Lastly, by quantifying DM into risk management decisions, which can include repair cost, lives lost, or down time, etc., Decision Variables (DV) may be calculated.

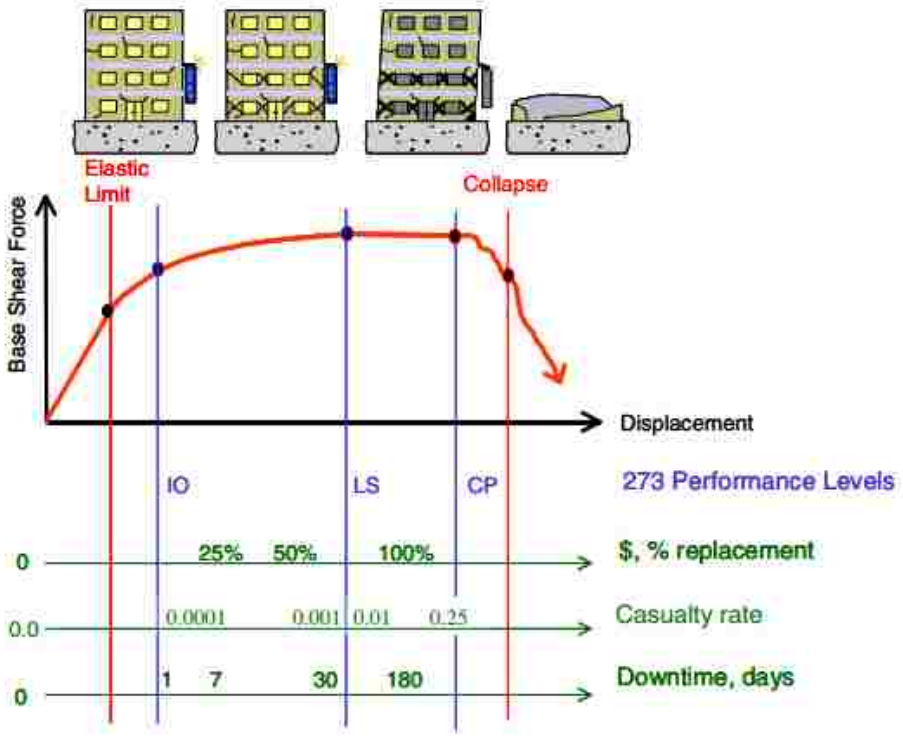

Figure 5-1: A Visualization of Performance-Based Earthquake Engineering (Moehle and Deierlein, 2004).

This framework can be represented using the flowchart shown in Figure 5-2, which can also be expressed in terms of a triple integral based on the total probability theorem, as stated in Equation (5-1).

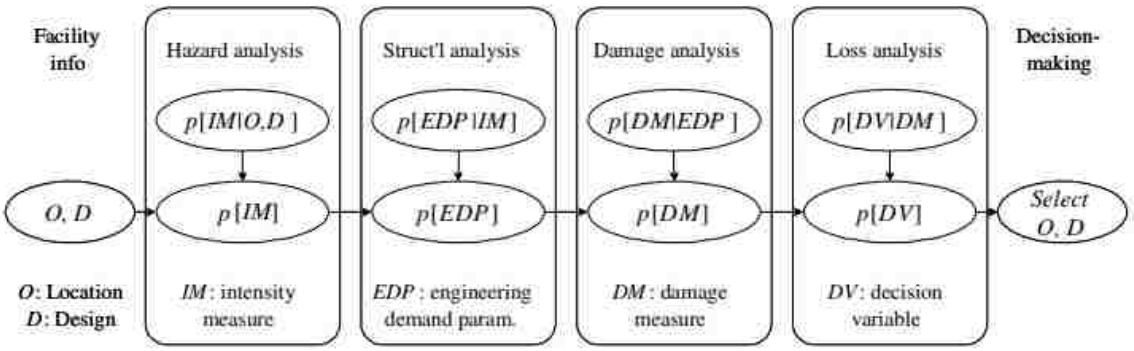

Figure 5-2: Underlying Probabilistic Framework (Porter, 2003).

$$\lambda_{DV} = \iiint P\langle DV \,|\, DM\rangle dP\langle DM \,|\, EDP\rangle dP\langle EDP \,|\, IM\rangle d\lambda_{IM} \tag{5-1}$$

which can be estimated numerically by:

$$\lambda_{DV} = \sum_{k=1}^{N_{DM}} \sum_{j=1}^{N_{EDP}} \sum_{i=1}^{N_{IM}} P\langle DV > dv \,|\, DM = dm_k\rangle \times P\langle DM = dm_k \,|\, EDP = edp_j\rangle \times P\langle EDP = edp_j \,|\, IM = im_i\rangle \Delta\lambda_{IM} \tag{5-2}$$

where λ_{DV} represents the total mean annual rate of exceedance of a *DV*,

$P\langle DV > dv \,|\, DM = dm_k\rangle$ represents the probability that a specified *DV* will exceed a certain level of *DV*, given particular *DM*, N_{DM}, N_{EDP} and N_{IM} are the number of increment of *DM*, *EDP* and *IM* respectively, $\Delta\lambda_{IM}$ is the incremental rate of exceedance of the *IM*.

5.1.1 Hazard Curves for *DV*

A hazard curve can be made for any of the parameters in the PBEE framework. Equation (5-1) provides the calculation necessary to create a *DV* hazard curve. Figure 5-3 shows an example hazard curve, where *DV* is expressed as economic loss. With such a hazard curve, stakeholders can clearly identify the level of loss for any rate of exceedance that they may be interested in.

Stakeholders can also have more confidence in their decisions because this hazard curve is developed using different possible earthquake scenarios rather than just one hypothetical scenario.

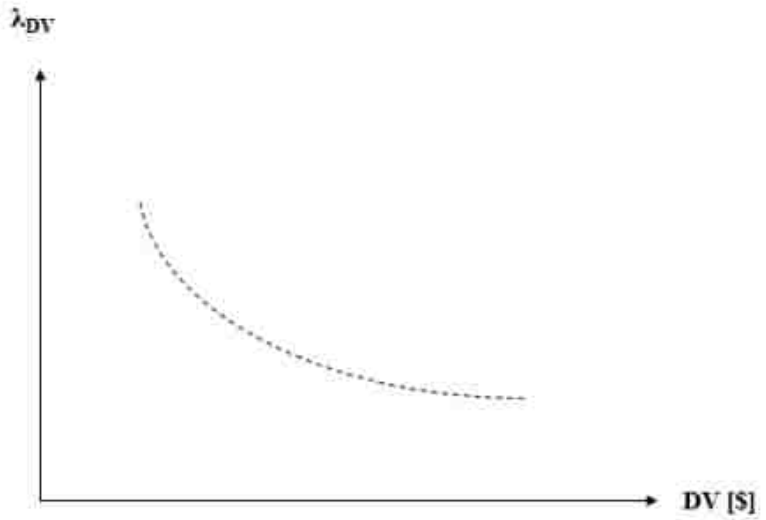

Figure 5-3: Illustration of a Hypothetical Hazard Curve with Economic Loss as the *DV* (Ulmer, 2015).

5.2 Liquefaction Triggering in PBEE Framework

The PBEE procedure is a useful tool for risk assessment. This framework may be applied to liquefaction triggering calculations to create FS_L hazard curves. Kramer and Mayfield (2007) suggested that M_w and $a_{\max}$ can be assigned as a joint *IM*, and FS_L as *EDP*. They also alter the probability of exceedance equation to probability of non-exceedance because engineers are generally more interested in FS_L not exceeding a certain value. The equation of non-exceedance can be expressed as:

$$\Lambda_{FS_L^*} = \sum_{j=1}^{N_N} \sum_{i=1}^{N_{a_{\max}}} P\left[FS_L < FS_L^* \mid a_{\max,i}, m_j \right] \Delta\lambda_{a_{\max,i}, m_j} \tag{5-3}$$

where $\Lambda_{FS^*_L}$ is the mean annual rate of not exceeding a certain factor of safety, N_M and $N_{a_{\max}}$ are the number of increments of M_w and $a_{\max}$, and $\Delta\lambda_{a_{\max,i},m_j}$ is the incremental mean annual rate of exceedance for intensity measure $a_{\max,i}$ and m_j.

Kramer and Mayfield (2007) also related the PBEE procedure with SPT resistance, N_{req}, which is the number of blow counts required to resist liquefaction. By applying the same method to CPT-based calculations, the mean annual rate of exceedance of the value q^*_{req} can be defined as (Arndt, 2017):

$$\lambda_{q^*_{req}} = \sum_{j=1}^{N_N} \sum_{i=1}^{N_{a_{\max}}} P\left[q_{req} < q^*_{req} \mid a_{\max,i}, m_j \right] \Delta\lambda_{a_{\max,i},m_j} \tag{5-4}$$

where

$$P\left[q_{req} < q^*_{req} \mid a_{\max,i}, m_j \right] = P_L(q^*_{req}) \tag{5-5}$$

where P_L is the probability against liquefaction, and it is calculated differently for the two triggering procedures.

For the Boulanger and Idriss (2014) triggering model, P_L is computed as shown in Equation (3-23). For the Ku et al. (2012) triggering model, P_L is computed as in Equation (3-35).

A hazard curve can be created by repeating Equation (5-4) for a range of q^*_{req} for each of the triggering methods. To relate FS_L and q_{req}, the following conversion may be used:

$$FS_L^{site} = \frac{CRR}{CSR} = \frac{CRR(q_{site})}{CSR(q_{req}^{site})} \tag{5-6}$$

where q_{site} is the measured corrected clean-sand equivalent CPT cone-tip resistance, and q_{req}^{site} is the computed corrected clean-sand equivalent cone-tip resistance required to resist liquefaction. With Equation (5-6), the q_{req} hazard curves may be converted to FS_L hazard curves. An example FS_L hazard curve is shown Figure 5-4.

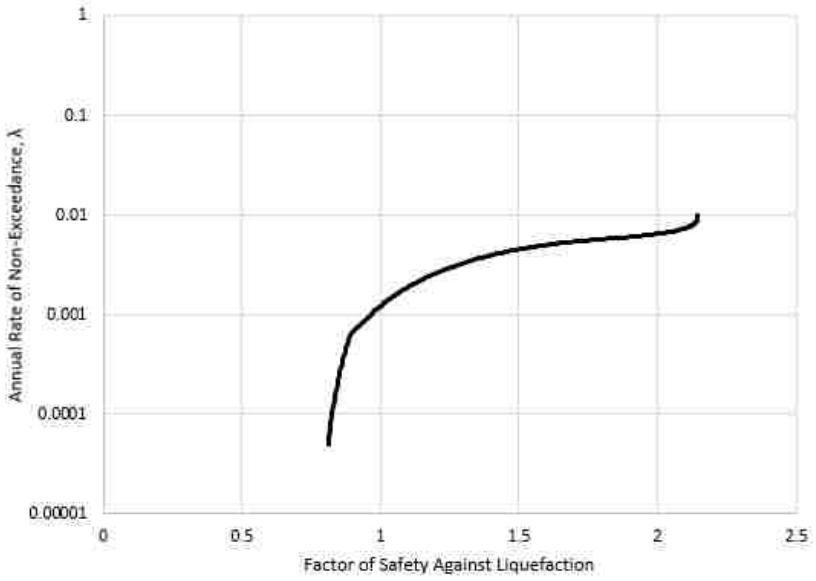

Figure 5-4: Example FS_L Hazard Curve for a Hypothetical Soil Layer Calculated in Salt Lake City, Utah.

5.3 Post-Liquefaction Settlement in PBEE Framework

Once the full performance-based triggering procedure is completed and the FS_L hazard curves are developed, a full performance-based post-liquefaction settlement analysis may be performed. The process of applying the PBEE framework to post-liquefaction settlement calculations is outlined in Hatch (2017). To begin with, FS_L and ε_v are assigned as *IM* and *EDP* respectively. The mean annual rate of exceedance of volumetric strain may be computed as:

$$\lambda_{\varepsilon_v^*} = \sum_{j=1}^{N_{FS_L}} P[\overline{\varepsilon_v} > \varepsilon_v^* \mid q_{c1Ncsi}, FS_{Lj}]\Delta\lambda_{FS_{Lj}} \tag{5-7}$$

where $\lambda_{\varepsilon_v^*}$ is the mean annual rate of exceeding a specified level of strain (ε_v^*), N_{FS_L} is the number of FS_L increments within the current soil layer's FS_L hazard space, q_{c1Ncs} is the current layer's corrected cone tip resistance, $\Delta\lambda_{FS_{Lj}}$ is the incremental mean annual rate of exceedance for intensity measure FS_L, and $P[\overline{\varepsilon_v} > \varepsilon_v^* \mid q_{c1Ncsi}, FS_{Lj}]$ is the probability of the calculated strain exceeding a specified level of strain (ε_v^*) given a specific incremental value from the FS_L hazard curve. The equation to calculate $P[\overline{\varepsilon_v} > \varepsilon_v^* \mid q_{c1Ncsi}, FS_{Lj}]$ is given as:

$$P[\overline{\varepsilon_v} > \varepsilon_v^* \mid q_{c1Ncsi}, FS_{Lj}] = \Phi\left[\frac{\ln(\overline{\varepsilon_v}) - \ln(\varepsilon_v^*)}{\sigma_{\ln(\varepsilon_v)}}\right] \tag{5-8}$$

where Φ represents the standard normal cumulative distribution function, $\sigma_{\ln(\varepsilon_v)}$ represents the model uncertainty and is equal to 0.276, and $\overline{\varepsilon_v}$ is the calculated strain using the Juang et al. (2013) strain Equation (4-4) multiplied by P_L. P_L is the probability of liquefaction computed using the Boulanger and Idriss (2014) and Ku et al. (2012) triggering models, which are presented in Equation (3-23) and Equation (3-35) respectively.

Using the calculated values of $\lambda_{\varepsilon_v^*}$ and ε_v^*, a hazard curve may be developed for one soil sublayer. An example volumetric strain hazard curve is shown in Figure 5-5. For any rate of exceedance that an engineer is interested in, a volumetric strain may be determined using this hazard curve. A hazard curve of settlement may also be created by calculating the volumetric strain hazard curve for each sublayer and applying Equation (4-5).

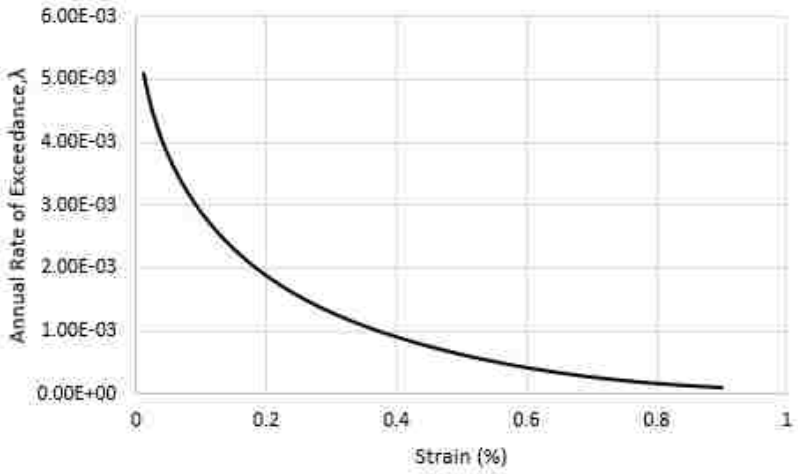

Figure 5-5: Example Volumetric Strain Hazard Curve for a Hypothetical Soil Sublayer Calculated in Salt Lake City, Utah.

5.4 Chapter Summary

The PBEE framework provides a more meaningful and informative tool for seismic hazard analysis. This framework can be applied to both liquefaction triggering and liquefaction settlement analyses. Hazard curves are generated during a performance-based procedure. They are useful for engineering design, but require a large amount of iterations and probabilistic calculations.

6 DEVELOPMENT OF THE SIMPLIFIED PERFORMANCE-BASED POST-LIQUEFACTION SETTLEMENT PROCEDURE

The PBEE framework has gained popularity over the past decades, but it is still not commonly used in routine engineering design due to its complexity. Though computational programs such as *WSliq* (Huang, 2008; Kramer,2008), *PBLiquefY* (Wright, 2013; Franke et al. 2014), *CPTLiquefY* (Franke et al. 2017) have been developed to perform PBEE calculations, they require some familiarity with PBEE principles.

To address this issue, Mayfield et al. (2010) suggested a simplified performance-based method, which combines the simplicity of the deterministic procedure and the completeness of the performance-based procedure. Based on the framework of Mayfield et al. (2010), other simplified performance-based procedures have been developed for SPT data to compute liquefaction triggering using the Boulanger and Idriss (2012) liquefaction triggering model (Ulmer, 2015), lateral spread displacements (Ekstrom, 2015), and post-liquefaction settlement (Error, 2017). With the increase use of CPT in the field, there is a need for a simplified performance-based procedure for the CPT. This study will focus on the development of a simplified performance-based procedure for post-liquefaction settlement. To better understand concepts of simplified performance-based methods, the procedure of Mayfield et al. (2010) is also described in this chapter. Then a detailed derivation of the simplified performance-based procedure for assessing post-liquefaction settlement using CPT data will be presented.

6.1 Simplified Performance-Based Methods

The simplified performance-based procedure is based on the idea of *liquefaction reference parameter maps*, which are contour maps showing liquefaction hazard values for a reference soil layer at a 6-meter depth, as shown in Figure 6-1. These liquefaction reference parameter maps are created by analyzing the reference soil profile using the full performance-based procedure across geographic coordinates at a given return period. Figure 6-2 is a sample contour map of N_{req}^{ref} for Washington State at return periods of 475-year and 2475-year. The liquefaction hazard value selected from the reference parameter maps is then corrected to a site specific value by applying correction factors, which will be discussed in greater details in subsequent sections.

6.1.1 Mayfield et al. (2010) Procedure

Mayfield et al. (2010) proposed a simplified performance-based procedure for the Cetin et al. (2004) model triggering model. While most engineers use *CSR* to characterize seismic loading, Mayfield et al. (2010) suggested that the SPT resistance required to resist liquefaction initiation, N_{req}, may be used. The relationship between N_{req} and *CSR* and *CRR* is shown in Figure 6-3.

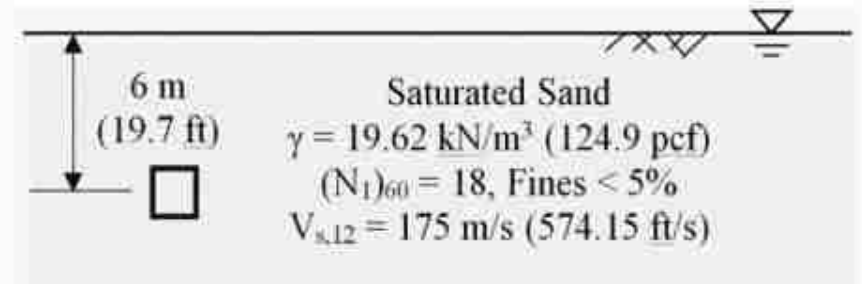

Figure 6-1: Reference Soil Layer Used to Develop Liquefaction Parameter Maps in the Mayfield et al. (2010) Simplified Procedure (Mayfield 2010).

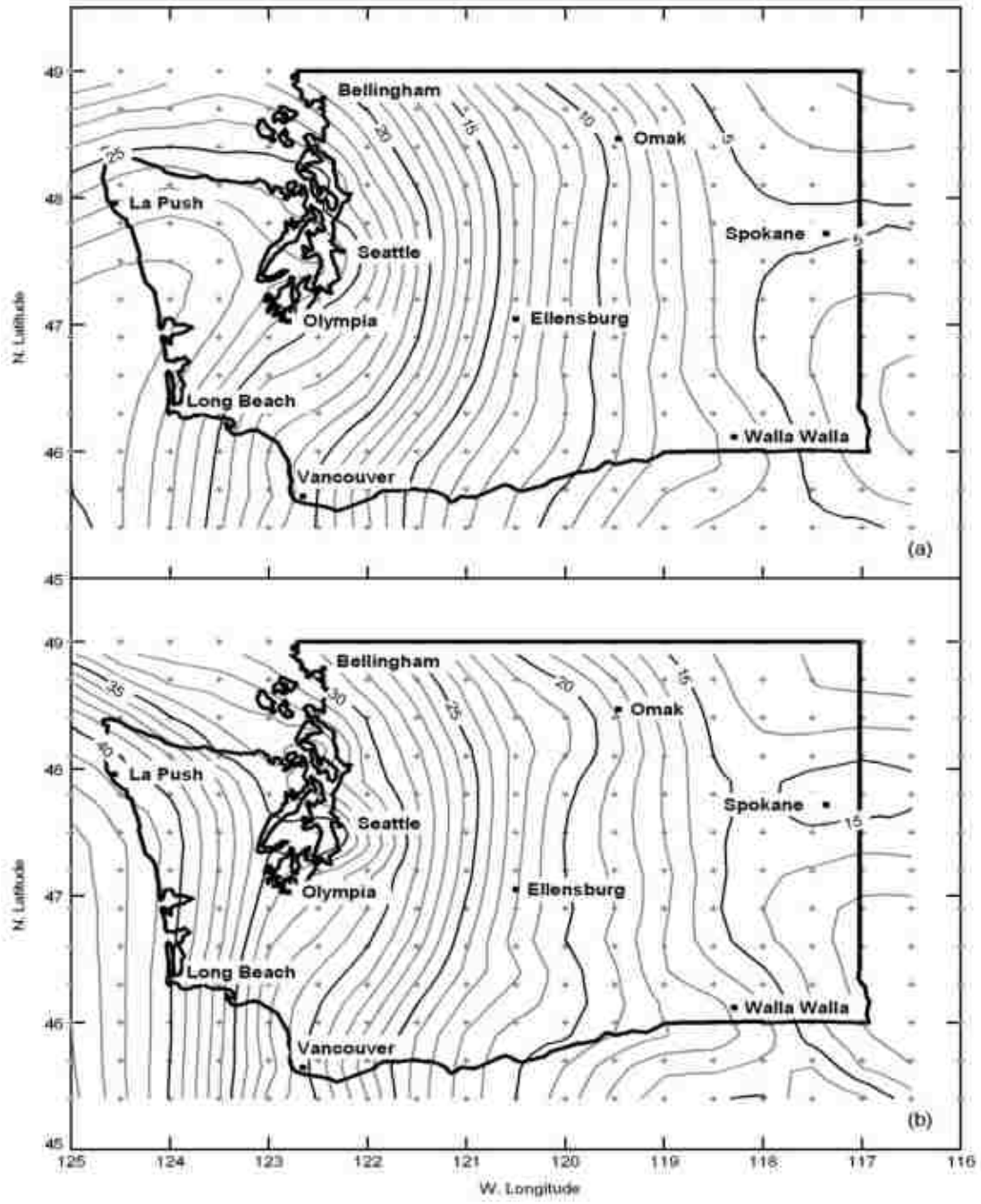

Figure 6-2: Contours of N_{req}^{ref} for Washington State: (a) 475-Year Return Period; (b) 2,475-Year Return Period (Mayfield et al., 2010)

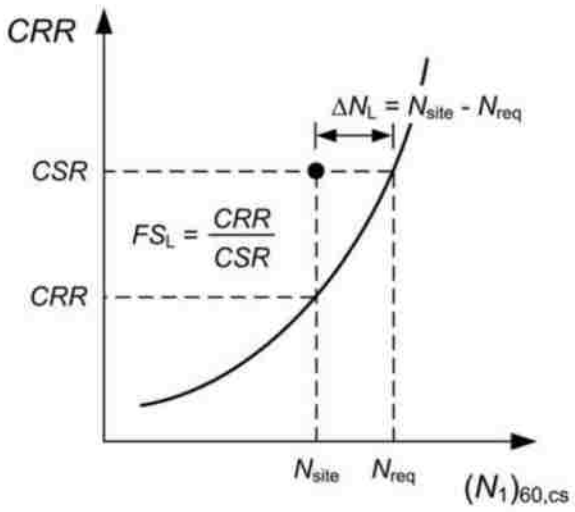

Figure 6-3: Relationship between CSR, CRR, and N_{req} (Mayfield et al., 2010)

Thus, liquefaction potential can be evaluated using Equation (6-1) .

$$\Delta N_L = N_{site} - N_{req} \tag{6-1}$$

where N_{site} is the actual SPT resistance in the soil layer, ΔN_L is the difference between N_{site} and N_{req}. A negative value of ΔN_L indicates that the soil layer does not have sufficient SPT resistance to resist liquefaction triggering.

Now the simplified procedure uses N_{req}^{ref} as the mapped liquefaction parameter. Mayfield et al. (2010) assumed that the site-specific value, N_{req}^{site}, can be related to the mapped reference value, N_{req}^{ref}, through a correction factor, ΔN_{req}, and the relationship is as shown:

$$N_{req}^{site} = N_{req}^{ref} + \Delta N_{req} \tag{6-2}$$

where ΔN_{req} is a site-specific correction term.

Mayfield el al. (2010) then used the following set of equations to solve for ΔN_{req}:

$$N_{req}^{ref} = 13.79 \ln\left[0.65 F_a^{ref} a_{\max,rock} \frac{\sigma_{v0}^{ref}}{(\sigma_{v0}^{'})^{ref}} r_d^{ref} \right] + 29.06 \ln(M_w) + 3.82 \ln \frac{(\sigma_{vo}^{'})^{ref}}{P_a} - 15.25 - 4.21 \Phi^{-1}(P_L) \tag{6-3}$$

$$N_{req}^{site} = 13.79 \ln\left[0.65 F_a^{site} a_{\max,rock} \frac{\sigma_{v0}^{site}}{(\sigma_{v0}^{'})^{site}} r_d^{site}\right] + 29.06 \ln(M_w) + 3.82 \ln \frac{(\sigma_{vo}^{'})^{site}}{P_a} - 15.25 - 4.21\Phi^{-1}(P_L) \quad (6\text{-}4)$$

$$\Delta N_{req} = N_{req}^{site} - N_{req}^{ref} = 13.79 \ln\left[\frac{\sigma_{v0}^{site} / (\sigma_{v0}^{'})^{site}}{\sigma_{v0}^{ref} / (\sigma_{v0}^{'})^{ref}}\right] + 3.82 \ln \frac{(\sigma_{v0}^{'})^{site}}{(\sigma_{v0}^{'})^{ref}} + 13.79 \ln \frac{F_a^{site}}{F_a^{ref}} + 13.79 \ln \frac{r_d^{site}}{r_d^{ref}} \quad (6\text{-}5)$$

Now engineers only need the value of N_{req}^{ref} provided through a liquefaction reference parameter map and Equations (6-2) and (6-5) to compute N_{req}^{site} at any depth at a site of interest, which can be used to determine liquefaction potential using Equation (6-1).

6.2 CPT-Based Simplified Performance-Based Procedure

The framework of Mayfield et al. (2010) can be applied to the development of simplified performance-based post-liquefaction settlement for the CPT. The simplified settlement procedure also relies on liquefaction reference parameter maps and correction factors. For consistency, a reference soil profile similar to the one used in Mayfield et al. (2010) and other SPT-based procedures is developed for this study, as shown in Figure 6-4, where $q_c = 6,800$ kPa and $f_s = 19.15$ kPa are used to define soil resistance of the reference soil layer at a 6-meter depth.

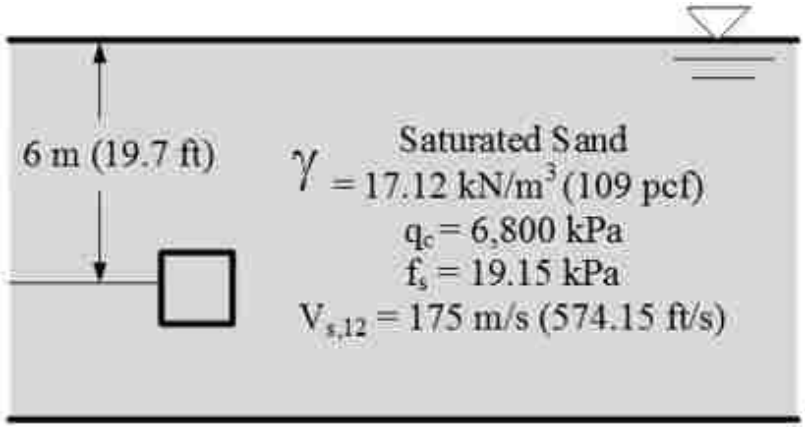

Figure 6-4: Reference Soil Profile Used to Develop Liquefaction Parameter Maps in the Simplified Performance-Based Procedure for CPT.

Full performance-based calculations are performed using the reference soil profile shown in Figure 6-4 for a series of gridded geographic coordinates. Contour maps are made using volumetric strain, ε_v, as the reference parameter. ε_v is computed with *CPTLiquefY* (Franke et al. 2017) using the methods presented in Chapter 5. Any value obtained from the liquefaction reference parameter map represents the reference volumetric strain, ε_v^{ref}, at the specific location. This ε_v^{ref} value needs to be corrected to accurately reflect site-specific conditions. The derivations of the correction factors for both the Boulanger and Idriss (2014) and Ku et al. (2012) triggering models are presented in the following sections.

6.2.1 Correction Factor for Volumetric Strain Using the Boulanger and Idriss (2014) Triggering Model

Because $\varepsilon_v^{ref} = 0.85$ is calculated using the reference soil profile, it must be corrected for site-specific soil conditions and depths before obtaining ε_v^{site}. A variety of relationships have been tested to relate ε_v^{ref} and ε_v^{site}. These relationships include:

$$\varepsilon_v^{site} = \varepsilon_v^{ref} - \Delta\varepsilon \tag{6-6}$$

$$\ln\left(\varepsilon_v^{site} + a\right)^b = \ln\left(\varepsilon_v^{ref} + a\right)^b + \Delta\varepsilon \tag{6-7}$$

$$\ln(\varepsilon_v^{site} + a)^b = \ln\left(\varepsilon_v^{ref} + a\right)^b \cdot \Delta\varepsilon \tag{6-8}$$

where *a* and *b* are constants ranging between 0.001 and 1000. A constant *a* was added to both ε_v^{site} and ε_v^{ref} to prevent a value of zero from occurring in the natural log operators.

After performing preliminary assessments, Equation (6-9) was best at predicting the volumetric strain calculated by the full performance-based method.

$$\ln\left(\varepsilon_v^{site}+1000\right)=\left(\ln\left(\varepsilon_v^{ref}+1000\right)\right)^{\frac{1}{3}}\cdot\Delta\varepsilon \tag{6-9}$$

where $\Delta\varepsilon$ is a site-specific correction factor. Rearranging Equation (6-9), we can solve for the correction factor $\Delta\varepsilon$ as:

$$\Delta\varepsilon=\frac{\ln(\varepsilon_v^{site}+1000)}{(\ln(\varepsilon_v^{ref}+1000))^{1/3}} \tag{6-10}$$

where ε_v^{site} in Equation (6-10) represents the full performance-based strain in the sublayer of interest and is unknown. To simplify the analysis, both ε_v^{ref} and ε_v^{site} can be approximated using the pseudo-probabilistic approach. This is an appropriate simplification because the same errors introduced by using the pseudo-probabilistic method should occur in both ε_v^{ref} and ε_v^{site}. These errors are minimized when performing the division in Equation (6-10). Thus, the equation for the correction factor may be approximated as:

$$\Delta\varepsilon\cong\frac{\ln\left(\varepsilon_{v,pseudo}^{site}+1000\right)}{\left(\ln\left(\varepsilon_{v,pseudo}^{ref}+1000\right)\right)^{\frac{1}{3}}} \tag{6-11}$$

where ε_v^{ref} and ε_v^{site} are volumetric strains calculated using a pseudo-probabilistic procedure with FS_L computed using the mean magnitude from the USGS deaggregation tool at the return period of interest.

Once the correction factor for a given soil sublayer is computed, site-specific strains are computed as:

$$\varepsilon_v^{site} = \exp\left(\ln\left(\varepsilon_v^{ref} + 1000\right)^{\frac{1}{3}} \cdot \Delta\varepsilon \right) - 1000 \tag{6-12}$$

where ε_v^{ref} is the volumetric strain obtained from the reference volumetric strain parameter map.

Equation (6-12) results in ε_v^{site} values that are non-linearly biased. Calibration equations were developed to correct this non-linear bias for different ranges of PGA. The final simplified site strain may be calculated as:

For $PGA < 0.2g$:

$$\varepsilon_{v,calibrated}^{site}(\%) = \begin{Bmatrix} 0 & \text{for } \varepsilon_v^{site} \le 0 \\ 0.7 \cdot \varepsilon_v^{site} & \text{for } 0 < \varepsilon_v^{site} \le 1.7 \\ (\varepsilon_v^{site} + 1.7)^{0.6} & \text{for } \varepsilon_v^{site} > 1.7 \end{Bmatrix} \tag{6-13}$$

For $PGA \ge 0.2g$:

$$\varepsilon_{v,calibrated}^{site}(\%) = \begin{Bmatrix} 0 & \text{for } \varepsilon_v^{site} \le 0 \\ 0.05 \cdot \varepsilon_v^{site} & \text{for } 0 < \varepsilon_v^{site} \le 1.7 \\ 0.975 \cdot \sqrt{2.5 \cdot \left[\frac{\left(\varepsilon_v^{site}\right)^3}{3.25} - 1.5 \right]} & \text{for } \varepsilon_v^{site} > 1.7 \end{Bmatrix} \tag{6-14}$$

where PGA is the 2475-year peak ground acceleration for the site that is being analyzed, ε_v^{site} is the site strain calculated in Equation (6-12). Once $\varepsilon_{v,calibrated}^{site}$ has been computed, the following equation may be applied to obtain the simplified performance-based settlement for the entire profile:

$$S_p = M \sum_{i=1}^{N} \varepsilon_{v,calibrated}^{site} \Delta Z_i \tag{6-15}$$

where M represents the re-solved modal bias correction factor and is equal to 1.014, $\varepsilon_{v,calibrated}^{site}$ is the simplified site strain calculated from Equation (6-14), and ΔZ_i is the i^{th} layer's thickness.

6.2.2 Correction Factor for Volumetric Strain using the Ku et al. (2012) Triggering Model

The framework presented in Section 6.2.1 can also be applied to the Ku et al. (2012) model. A preliminary assessment was also performed to relate ε_v^{ref} and ε_v^{site}. Equation (6-16) was found to minimize the difference between the full-performance based method and the simplified method.

$$\ln\left(\varepsilon_v^{site}+100\right)=\left(\ln\left(\varepsilon_v^{ref}+100\right)\right)^{\frac{1}{3}}\cdot\Delta\varepsilon \tag{6-16}$$

As explained in Section 6.2.1, the correction factor, Δε, can be approximated using pseudo-probabilistic estimates of ε_v^{ref} and ε_v^{site}. $\Delta\varepsilon$ for a given soil sublayer using the Ku et al. (2012) model can then be estimated as:

$$\Delta\varepsilon\cong\frac{\ln\left(\varepsilon_{v,pseudo}^{site}+100\right)}{\left(\ln\left(\varepsilon_{v,pseudo}^{ref}+100\right)\right)^{\frac{1}{3}}} \tag{6-17}$$

where ε_v^{ref} and ε_v^{site} are volumetric strains calculated using pseudo probabilistic method.

The site-specific strain for the soil sublayer can be computed as:

$$\varepsilon_{v,pseudo}^{site}=\exp\left(\ln\left(\varepsilon_{v,pseudo}^{ref}+100\right)^{\frac{1}{3}}\cdot\Delta\varepsilon\right)-100 \tag{6-18}$$

where ε_v^{ref} is the volumetric strain obtained from the reference volumetric strain parameter map.

Again, due to the non-linearity of the model, calibration equations were developed to obtain the final site specific strains as:

For $PGA < 0.2g$:

$$\varepsilon_{v,calibrated}^{site}(\%) = \begin{cases} 0 & \varepsilon_v^{site} \le 0 \\ 0.8 \cdot \varepsilon_v^{site} & 0 < \varepsilon_v^{site} \le 2 \\ \sqrt{\dfrac{\varepsilon_v^{site} - 0.86}{0.38}} & \varepsilon_v^{site} > 2 \end{cases} \quad (6\text{-}19)$$

For $PGA \ge 0.2g$:

$$\varepsilon_{v,calibrated}^{site}(\%) = \begin{cases} 0 & \varepsilon_v^{site} \le 0 \\ 0.322 \cdot \varepsilon_v^{site} & 0 < \varepsilon_v^{site} \le 1.8 \\ 0.805 \cdot \sqrt{8 \cdot \left[\dfrac{(\varepsilon_v^{site})^2}{3} - 1 \right]} & \varepsilon_v^{site} > 1.8 \end{cases} \quad (6\text{-}20)$$

$\varepsilon_{v,calibrated}^{site}$ can then be applied to Equation (6-15) to obtain the total settlement using the Ku et al. (2012) model for FS_L.

6.2.3 Summary of the Simplified Performance-Based Procedure

The simplified method for calculating site-specific settlement consists of the following steps:

1. Obtain a reference strain, ε_v^{ref}, from a liquefaction reference parameter map.
2. Calculate the correction factor, $\Delta\varepsilon$, with $\varepsilon_{v,pseudo}^{site}$ and $\varepsilon_{v,pseudo}^{site}$.
3. Calculate the simplified site-specific strain, ε_v^{site}.
4. Compute site-specific strains, $\varepsilon_{v,calibrated}^{site}$.
5. Compute total settlement for the whole soil profile.

6.3 Sample Calculation

To demonstrate how to use the simplified performance-based procedure to calculate post-liquefaction settlement for a set of site-specific conditions, a step-by-step sample calculation is provided in this section. For the purpose of demonstration, only calculations using the Boulanger and Idriss (2014) triggering model will be given, but the same procedure may also be applied to the Ku et al. (2012) triggering model.

The site that is being analyzed is located in Salt Lake City, Utah with latitude and longtitude of 40.76˚N and -111.898˚W respectively. The recorded CPT sounding is shown in Figure 6-5, including tip resistance, sleeve friction, pore pressure, and soil classification based on Soil Behavior Index Type, I_c. The ground water table is set to be at the ground surface, and the site is classified as Site Class D (i.e. $V_{s,30}$=180 m/sec to 360 m/sec). Calculations are performed using a return period of 1033 years.

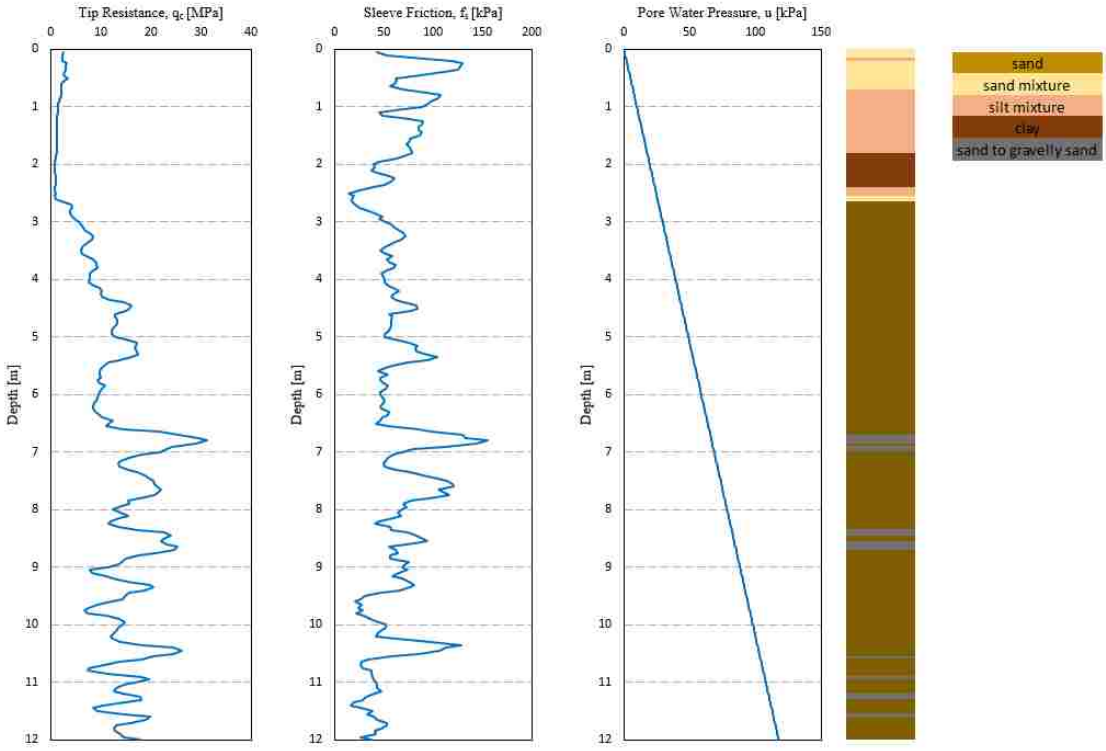

Figure 6-5: CPT Sounding for the Example Problem.

Table 6-1 shows the step-by-step results of the simplified performance-based procedure. The first column shows the depth of the sublayer that is being analyzed. For this demonstration, only depths of 6m to 7m are shown. Columns (2) and (3) are the estimated volumetric strain for the site-specific profile and the reference profile calculated using the pseudo-probabilistic procedure; Columns (4) is the site-specific volumetric strains computed using the full performance-based procedure. Both of the pseudo-probabilistic and the performance-based calculations are performed by *CPTLiquefY* (Franke et al. 2017). The following steps are used to calculate the simplified performance-based settlement for depths of 6m to 7m.

Table 6-1: Step by Step Results for the Example Problem (6m to 7m)

(1)	(2)	(3)	(4)	(5)	(6)	(7)	(8)	(9)	(10)	(11)	(12)
Depth (m)	Pseudo ε_v^{site}	Pseudo ε_v^{ref}	PB ε_v^{site}	PB ε_v^{ref}	Δε	Simp ε_v^{site}	Calibrated ε_v^{site}	ΔZ	Sub Settlement	Total Simp Se (cm)	Total PB Se (cm)
6.00	1.921	2.335	1.848	2.60	3.628	2.009	1.539	0.05	0.077	0.948	1.088
6.05	1.954	2.335	1.916	2.60	3.628	2.043	1.633	0.05	0.082		
6.10	1.981	2.335	1.969	2.60	3.628	2.069	1.707	0.05	0.085		
6.15	2.063	2.335	2.125	2.60	3.628	2.152	1.929	0.05	0.096		
6.20	2.130	2.335	2.243	2.60	3.628	2.218	2.102	0.05	0.105		
6.25	2.103	2.335	2.194	2.60	3.628	2.191	2.032	0.05	0.102		
6.30	2.050	2.335	2.091	2.60	3.628	2.138	1.892	0.05	0.095		
6.35	1.932	2.335	1.857	2.60	3.628	2.020	1.570	0.05	0.078		
6.40	1.859	2.335	1.691	2.60	3.628	1.947	1.354	0.05	0.068		
6.45	1.642	2.335	0.847	2.60	3.628	1.731	0.477	0.05	0.024		
6.50	1.713	2.335	1.237	2.60	3.628	1.801	0.842	0.05	0.042		
6.55	1.761	2.335	1.409	2.60	3.628	1.849	1.029	0.05	0.051		
6.60	1.498	2.335	0.033	2.60	3.627	1.586	0.079	0.05	0.004		
6.65	1.211	2.335	0.000	2.60	3.627	1.299	0.065	0.05	0.003		
6.70	1.200	2.335	0.000	2.60	3.627	1.288	0.064	0.05	0.003		
6.75	1.200	2.335	0.000	2.60	3.627	1.288	0.064	0.05	0.003		
6.80	1.200	2.335	0.000	2.60	3.627	1.288	0.064	0.05	0.003		
6.85	1.200	2.335	0.000	2.60	3.627	1.288	0.064	0.05	0.003		
6.90	1.200	2.335	0.000	2.60	3.627	1.288	0.064	0.05	0.003		
6.95	1.200	2.335	0.000	2.60	3.627	1.288	0.064	0.05	0.003		
7.00	1.209	2.335	0.000	2.60	3.627	1.298	0.065	0.05	0.003		

1. Obtain ε_v^{ref} from the volumetric strain reference parameter map. At this step, it is crucial to use the reference parameter map that has the correct return period and desired model. For the sample calculation, the Boulanger and Idriss (2014) map for 1033 year return period should be used, ε_v^{ref} (%) = 2.6 [Column (5)].

2. Calculate the correction factor, Δε [Column (6)], using Equation (6-11) and the values of $\varepsilon_{v,pseudo}^{ref}$ and $\varepsilon_{v,pseudo}^{site}$ [Columns (2) and (3)].
3. Calculate the simplified volumetric strain value [Column (7)] using Equation (6-12) and values of ε_{v}^{ref} and Δε [Columns (5) and (6)].
4. Calibrate the simplified volumetric strain value using Equation (6-14) and values of simplified ε_{v}^{site} [Column (7)]. The resulted $\varepsilon_{v,calibrated}^{site}$ values are shown in Column (8).
5. Compute the total settlement [Column (11)] for the depths of 6m to 7m. This is done by summing up the individual sublayer settlement, which is the multiplication of $\varepsilon_{v,calibrated}^{site}$ and ΔZ [Column (9)].

To compare the results, the individual sublayer strains and the total settlement calculated using the full performance-based procedure are also shown in Table 6-1. Using the simplified performance-based procedure, the estimated total settlement for depths of 6m to 7m is 0.948 cm, which compares well to the total settlement of 1.088 cm from the full performance-based procedure.

This same procedure can be repeated for all other depths to obtain the simplified performance-based post-liquefaction settlement. This settlement is computed to be 10.08cm; while the prediction from the full performance-based procedure is 11.20cm. The error introduced by applying the simplified procedure is about 1.12 cm.

6.4 Chapter Summary

The framework of simplified performance-based procedure was first proposed by Mayfield et al. (2010), and was used to develop other simplified procedures for the SPT. This study has developed a simplified performance-based procedure for assessing post-liquefaction settlement

using CPT data. This procedure consists of obtaining a reference strain from the reference parameter map, and correcting the reference strain to a site-specific strain by applying site-specific correction equations. These equations are presented in this chapter for both the Boulanger and Idriss (2014) and the Ku et al. (2012) triggering models. A sample calculation is also given to demonstrate the application of the proposed procedure. The simplified performance-based procedure closely approximates the settlement calculated from the full performance-based procedure.

7 REFERENCE PARAMETER MAPS

An essential part of the simplified performance-based procedure is to obtain the reference volumetric strain value, ε_v^{ref}, from reference parameter maps. These maps provide values of the hazard parameter (i.e., ε_v) for the reference soil profile at a set of grid points and at the period of interest. As part of this study, reference parameter maps for Connecticut, South Carolina, Oregon, and Utah are also created for return periods of 475, 1033, and 2475 years, see Appendix A.

7.1 Development of Reference Parameter Maps

The reference parameter maps are created following these steps:

1. Perform grid spacing study.
2. Create a list of grid points.
3. Run full performance-based analysis on grid points.
4. Interpolate strain values between grid points
5. Create contours based on interpolated strain values.

Steps 2, 4 and 5 are accomplished using ArcMAP, developed by the Environmental Systems Research Institute, ESRI. Step 3 is done using *CPTLiquefy*, a C++ program developed by a group of graduate students in Brigham Young University. Detailed descriptions of each step is given in the following sections.

7.2 Grid Spacing Study

To develop the reference parameter maps, it is first necessary to understand how spacing of the grid points used to make the maps could potentially bias the analysis results. The distance between analysis grid points is crucial to the accuracy of the parameter maps. If these grid points are too far apart, the resolution of the maps is not be able to capture changes over the areas. If these grid points are too close together, the maps become computationally expensive to develop. As such, a grid spacing study was to find the optimal spacing for developing reference parameter maps for volumetric strain in various seismic environments.

Based on previous SPT simplified procedures (Ulmer, 2015; Ekstrom, 2015; Error, 2017), it was hypothesized that areas of high mapped *PGA* hazard would require smaller grid spacing, and areas of low mapped *PGA* hazard would allow larger grid spacing. The USGS 2014 *PGA* hazard map (Figure 7-1) was chosen for this study, which divides the United States into areas of different *PGA* ranges.

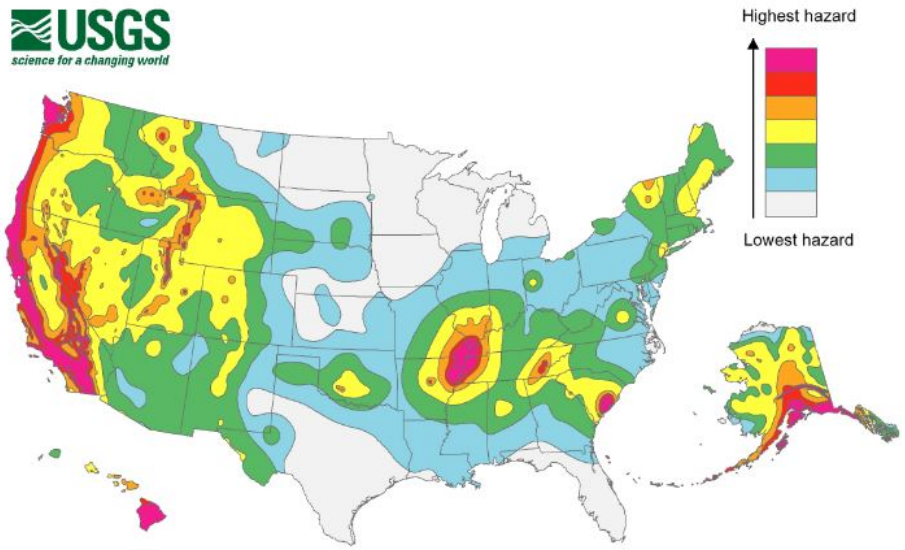

Figure 7-1: PGA Hazard Map (T_R = 2475 years) after USGS 2014.

36 cities representing different *PGA* ranges and were chosen from different regions across the United States. Figure 7-2 shows the chosen cities and the 2014 *PGA* corresponding to a return period of 2475 years.

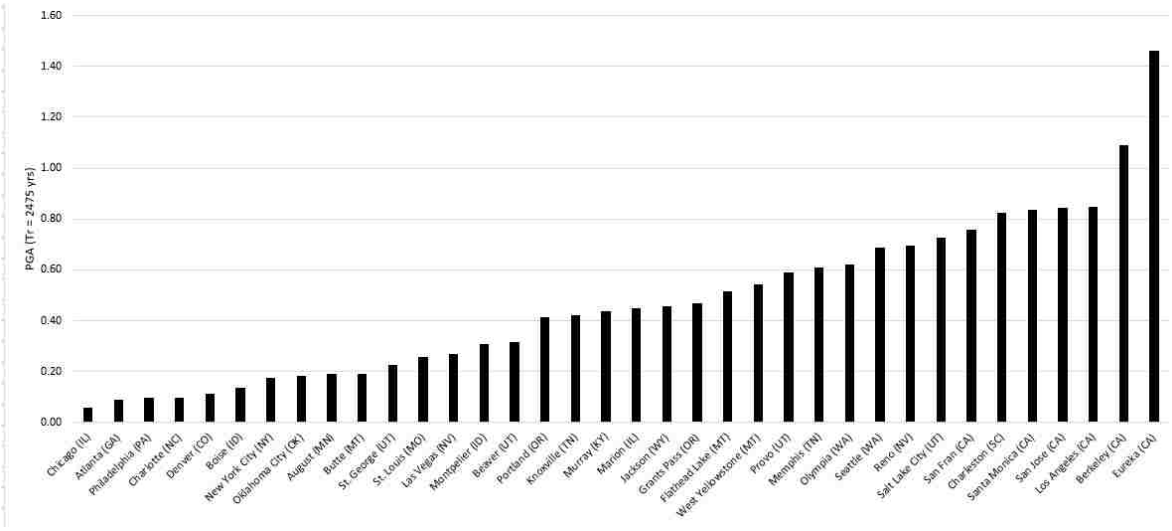

Figure 7-2: Range of *PGA* Values for Cities Included in Grip Spacing Study.

Following the framework provided by Ulmer (2015), the grid spacing study was performed using square grids with the site of interest as the anchor point in the center, as shown in Figure 7-3. To determine the maximum grid spacing, corner points were created with spacings of 1, 2, 4, 8, 16, 25, and 50 km.

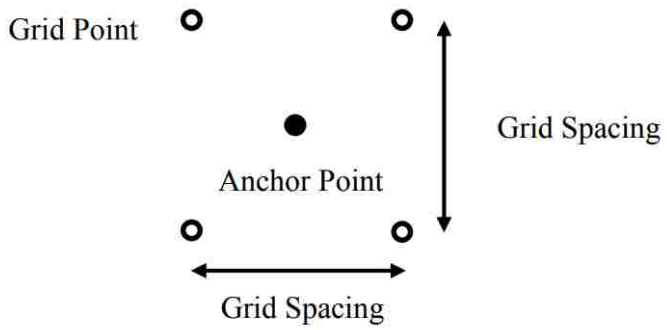

Figure 7-3: Layout of Grid Points Centered on a City's Anchor Point (Ulmer, 2015).

Full performance-based analyses were performed at the center point and the four corner points. The interpolated reference strain value, $\varepsilon_{v,\text{interpolated}}^{ref}$, which was the average of the four corner values, was then compared with the anchor value, $\varepsilon_{v,anchor}^{ref}$. An error was then calculated as the absolute difference between the interpolated value and the anchor value as shown:

$$Error = \left| \varepsilon_{v,\text{int}erpolated}^{ref} - \varepsilon_{v,anchor}^{ref} \right| \tag{7-1}$$

This error term was calculated at each grid spacing for all 36 cities. The optimum grid spacing for each city was then determined separately by plotting the absolute errors calculated using Equation (7-1) against the corresponding grid spacing. For this study, the optimum grid spacing for any city was defined as the target grid spacing that yields an absolute error less than 0.1%. The correlations between the absolute error and grid spacing were different for each city. A best-fit trend line (Figure 7-4) or curve (Figure 7-5) was used to determine the optimum grid spacing at absolute error of 0.1%. The optimum grid spacing for Figure 7-4 and Figure 7-5 are 10 km and 40 km, respectively. Because some of the cities such as New York City, NY did not reach the absolute error of 0.1% even at large grid spacing (Figure 7-6), a maximum grid spacing threshold of 50 km was set to maintain accuracy.

The optimum grid spacing for each city was then plotted against the expected *PGA* value of the city, which can be found on the *USGS* website. Correlations between PGA and optimum grid spacing for the Boulanger and Idriss (2014) and the Ku et al. (2012) triggering models are shown in Figure 7-7 and Figure 7-8, respectively.

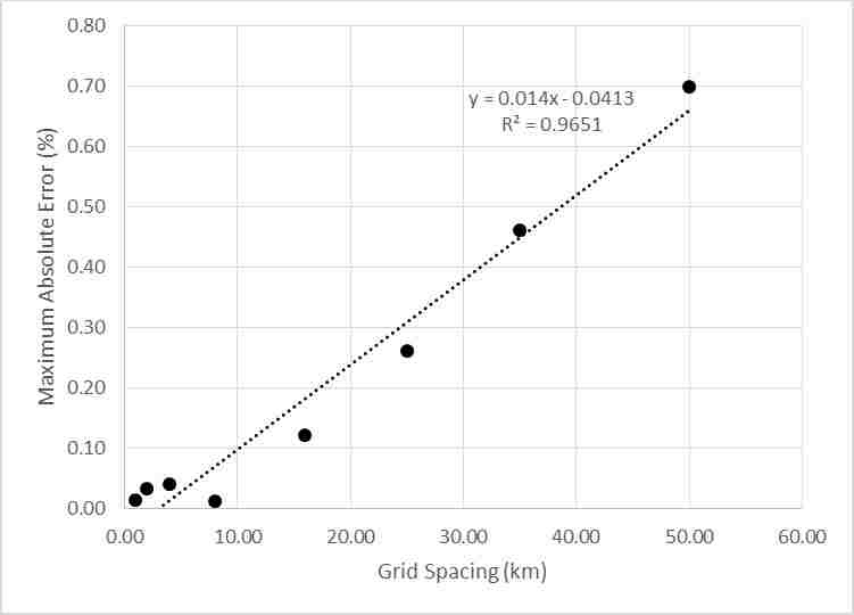

Figure 7-4: Variation of Maximum Absolute Percent Error with Increasing Distance between Grid Points (Charleston, SC).

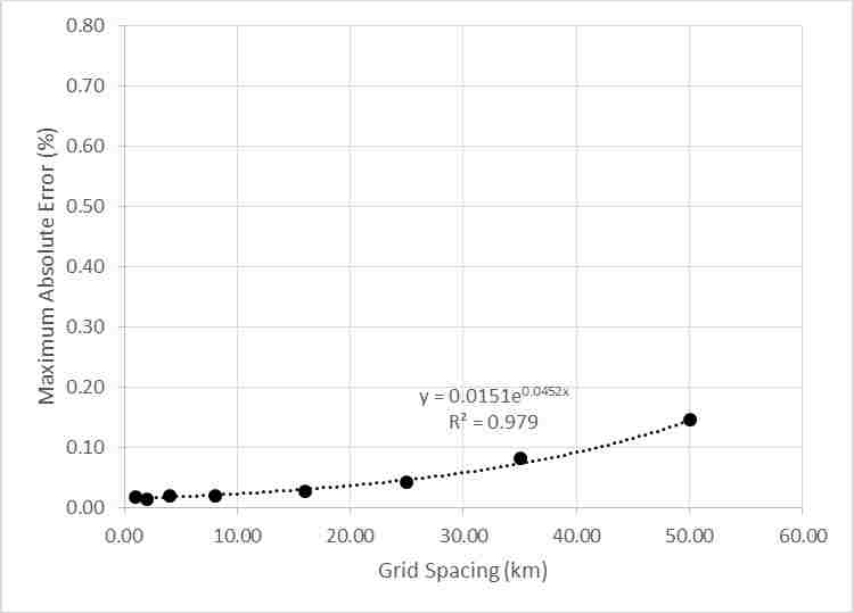

Figure 7-5: Variation of Maximum Absolute Percent Error with Increasing Distance between Grid Points (New York City, NY).

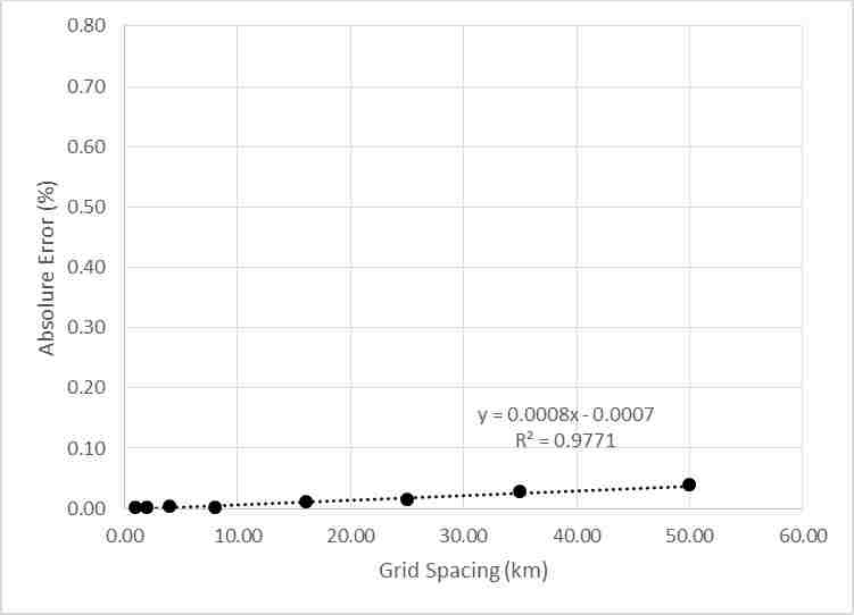

Figure 7-6: Variation of Maximum Absolute Percent Error with Increasing Distance between Grid Points (Boise, ID).

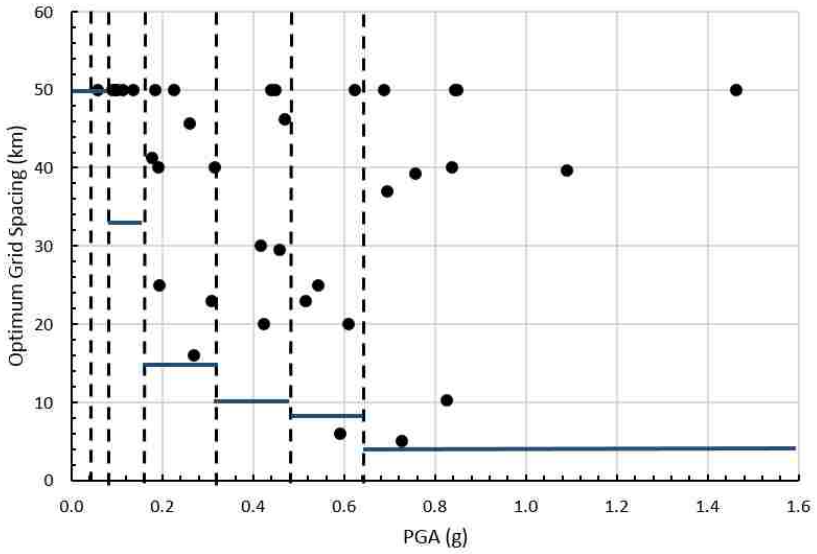

Figure 7-7: Correlation between *PGA* and Optimum Grid Spacing to Achieve 0.1% Maximum Absolute Percent Error, for Boulanger and Idriss (2014) Triggering Model.

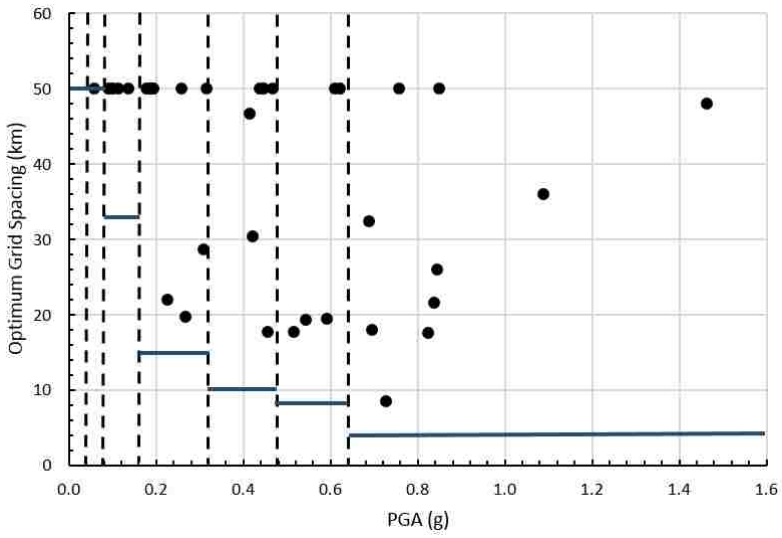

Figure 7-8: Correlation between PGA and Optimum Grid Spacing to Achieve 0.1% Maximum Absolute Percent Error for Ku et al. (2012) Triggering Model.

The vertical dashed lines indicate different *PGA* ranges (i.e., colors) from the USGS 2014 *PGA* hazard map. The horizontal blue lines were chosen to define the lower bound of the grid spacing for each *PGA* range. To simplify the computational process, for the same PGA range, the same lower bound was applied to both the Boulanger and Idriss (2-14) and the Ku et al. (2012) triggering models. These results were summarized in Table 7-1.

Table 7-1: Proposed Set of Rules to Determine Optimum Grid Spacing within a *PGA* Range.

PGA	Color	Spacing (km)	Spacing (mi)
0-0.04	Gray	50	31.1
0.04-0.08	Blue	50	31.1
0.08-0.16	Green	33	20.5
0.16-0.32	Yellow	15	9.3
0.32-0.48	Orange	10	6.2
0.48-0.64	Red	8	5.0
0.64+	Pink	4	2.5

7.3 Create a List of Grid Points with Coordinates

In ArcMap, different polygons were made to represent the different *PGA* ranges or color zones from the USGS 2014 hazard map. The *Fishnet* tool was used to create grid points within each color zone using different grid spacing, as specified in Table 7-1. These grid points were merged into one shapefile for each state and were exported as a text file. Figure 7-9 shows a map of Oregon with grid points and *PGA* color zones. Because the geographic coordinates of these grid points were needed to perform analysis in the next step, the X- and Y- coordinates needed to be calculated in the attribute table before exporting. The total number of coordinates analyzed in each state is presented in Table 7-2.

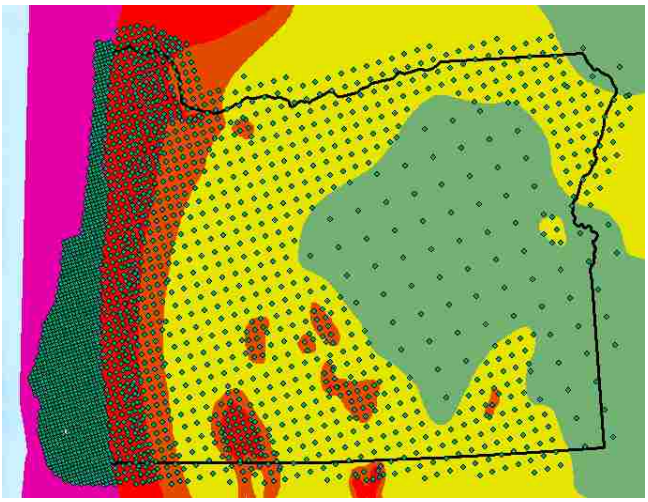

Figure 7-9: Location of Grid Points for Oregon with PGA Color Zones in Background.

Table 7-2: Number of Grid Points Analyzed for Map Development (by State).

State	Number of Grid Points
CT	42
OR	2,999
SC	1,047
UT	1,258
Total	**5,346**

7.4 Perform Full Performance-Based Analysis at the Grid Points

The list of coordinates were then entered into the *CPTLiquefy* (Franke et al., 2017) to perform full performance-based calculations. The vertical strain of the reference profile was computed for each location of grid point. These analyses were performed at return periods of 475, 1033 and 2475 years for both the Ku et al. (2012) and Boulanger and Idriss (2014) models. These results were then compiled into one excel file to for map creation.

7.5 Interpolating Values between Grid Points

The calculated grid points from Section 7.3 did not provide values for every possible location within the state, which means that interpolation is needed at locations that are located between grid points. The *Kriging* tool in ArcMap provides a convenient way to interpolate values between grid points and generate a raster that can be used to develop contour mpas. A sample raster for Oregon generated using the *Kriging* tool is shown in Figure 7-10.

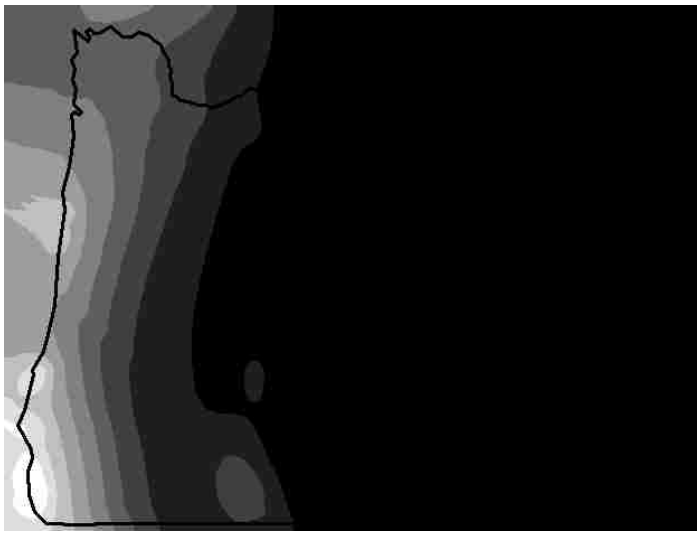

Figure 7-10: Sample Kriging Raster for Oregon with Light Areas as Larger Values of ε_v^{ref} at Return Period of 475 years.

7.6 Develop Contour Maps Using the Interpolated Values

With the raster created from Section 7.5, contour lines were made using the *Contour* tool in ArcMap. Larger contour intervals were needed to show clear contour lines in high seismicity areas, while smaller contour intervals were needed to show the changes in low seismicity areas. A map of Oregon (Figure 7-11) is shown to demonstrate the different contour intervals.

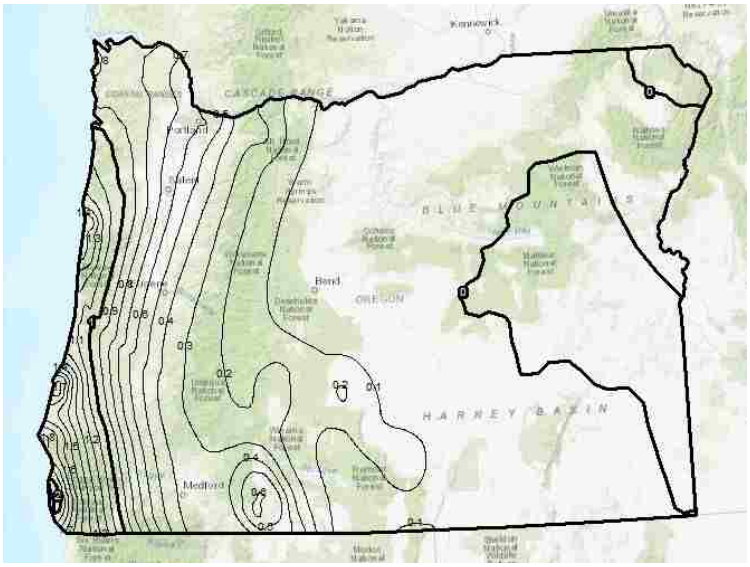

Figure 7-11: Sample Contour Map for Oregon at Return Period of 1033 Years.

7.7 Chapter Summary

A grid spacing study was performed to determine the maximum grid spacing for different *PGA* zones. A list of grid points was created for each of the four states (CT, OR, SC, UT) using the rules set from the grid spacing study. These points were then analyzed and imported to ArcMap to create contour maps. The creation of these parameter maps is a crucial part of the simplified performance-based procedure because it allows the complex full performance-based calculation to be transformed into a simple map reading process.

8 VALIDATIONS FOR THE SIMPLIFIED PERFORMANCE-BASED PROCEDURE

Though Chapter 6 showed that a simplified full performance-based procedure could be derived and Chapter 7 showed that reference parameter maps for volumetric strain could be created, the method needs to be validated before applying it in practice. To evaluate the accuracy of the introduced simplified performance-based procedure, a comparison between the results of simplified and full performance-based analyses were performed for 17 sites throughout the United States. These sites were evaluated for three different return periods: 475, 1033, and 2475 years, and with 20 different CPT soundings. Because liquefaction parameter maps were not available for all 17 sites that were chosen, liquefaction reference parameter maps were not used in the validation study. All reference values, ε_v^{ref}, were computed directly using *CPTLiquefy* (Franke et al., 2017).

8.1 Locations and CPT Soundings

The sites chosen for this study were selected based on the range of seismicity of each site, as well as their distribution across the United States. Table 8-1 and Table 8-2 are lists of the locations of these sites, latitudes and longitudes, and *PGA* at the return period of 2475 years. These sites were segregated based on *PGA*, because different calibration equations are used when the *PGA* values are above or below 0.2g. The *PGA* values were retrieved from the 2014 USGS interactive deaggregation tool.

Table 8-1: Cities Selected for Validation Study with *PGA* Lower Than 0.2g.

Site	Latitude	Longitude	PGA (g)
Louisville, KY	38.367	-83.828	0.099
Battleground, AL	34.316	-87.051	0.135
Leland, IL	41.577	-88.791	0.076
Quality, KY	37.115	-86.861	0.153
Bonelli Landing,AZ	35.995	-114.569	0.179
Grand View,ID	42.695	-116.171	0.112
Spokane, WA	47.768	-117.652	0.136
Butte, MT	46.003	-112.533	0.193

Table 8-2: Cities Selected for Validation Study with *PGA* Higher than 0.2g.

Site	Latitude	Longitude	PGA (g)
Charleston, SC	32.726	-79.931	0.730
Memphis, TN	35.149	-90.048	0.609
Eureka, CA	40.802	-124.162	1.462
Portland, OR	45.523	-122.675	0.415
Salt Lake City, UT	40.755	-111.898	0.726
San Francisco, CA	37.775	-122.418	0.757
San Jose, CA	37.339	-121.893	0.845
Santa Monica, CA	34.015	-118.492	0.838
Seattle, WA	47.530	-122.300	0.689

20 actual CPT soundings were chosen for this validation study to cover a wide range of soil stiffness and type. These CPT soundings, which were collected from the USGS database of CPT data, were also used to validate the accuracy of *CPTLiquefy* (Hatch, 2017). A plot of corrected cone tip resistance (Q_{tncs}) of the 20 CPT soundings is shown in Figure 8-1.

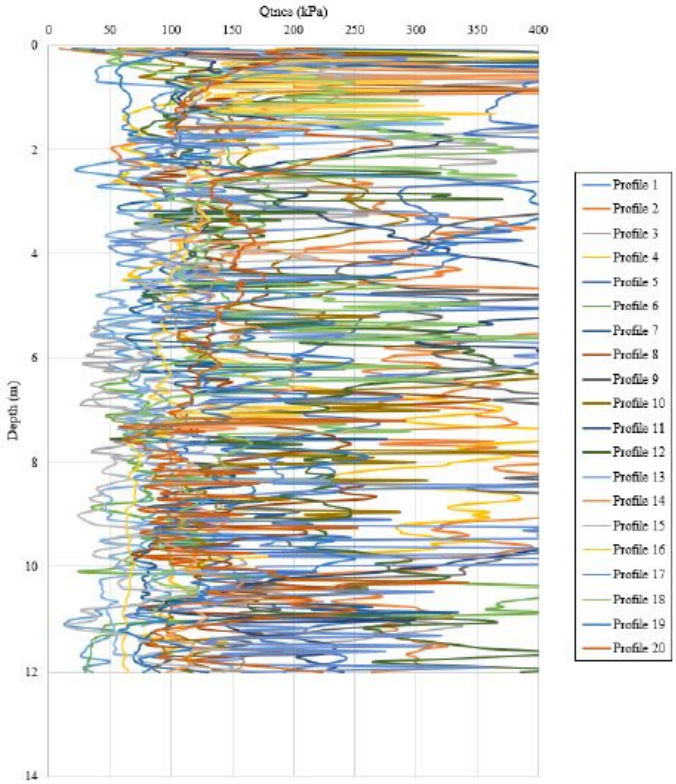

Figure 8-1: 20 CPT Profiles Plotted at Depth.

8.2 Validation of the Simplified Performance-Based Procedure

Post-liquefaction settlements were computed with the full performance-based procedure for the 20 different soil profiles in 17 different cities (8 with *PGA* lower than 0.2g, 9 with *PGA* higher than 0.2g) across the United States, using both the Boulanger and Idriss (2014) and Ku et al. (2012) triggering models. Then the same calculations were performed using simplified performance-based procedure as explained in Section 6.2. All of these analyses assumed that the water table was at ground surface.

The results calculated from the full performance-based procedure were plotted on the x-axis, and the results from the simplified procedure were plotted on the y-axis. If the simplified procedure accurately approximates the full performance-based procedure, the computed settlement

values should fall on a 1:1 (i.e., 45-degree angle) line. Points falling above the 1:1 line indicate over-estimation of settlement with the simplified procedure. Conversely, points falling below the 1:1 line indicate under-estimation of settlement with the simplified procedure. These plots are shown and discussed in Sections 8.2.1 and 8.2.2.

8.2.1 Validation of the Simplified Settlement Procedure Using Boulanger and Idriss (2014) Model

Figure 8-2 and Figure 8-3 show the validations of the simpflied proformance-based procedure using the Boulanger and Idriss (2014) triggering model. Figure 8-2 consists of cities with PGA lower than 0.2g; Figure 8-3 consists of cities with PGA higher than 0.2g.

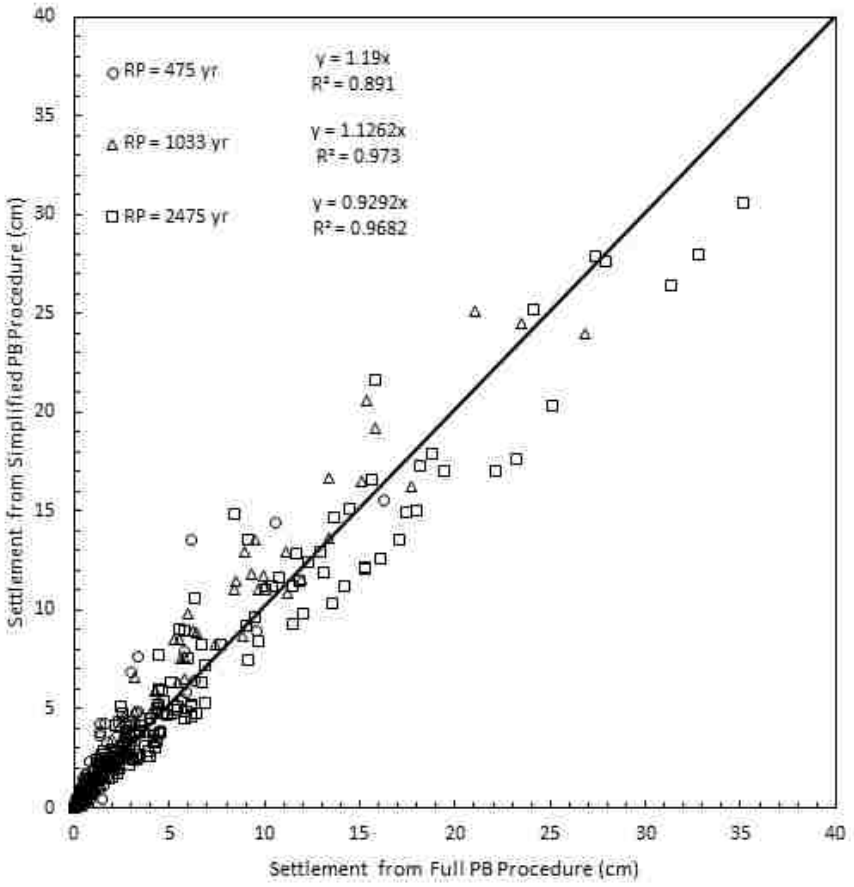

Figure 8-2. Boulanger and Idriss (2014) Full Performance-Based Settlement vs. Simplified Settlement Separated by Return Period (for *PGA* lower than 0.2g).

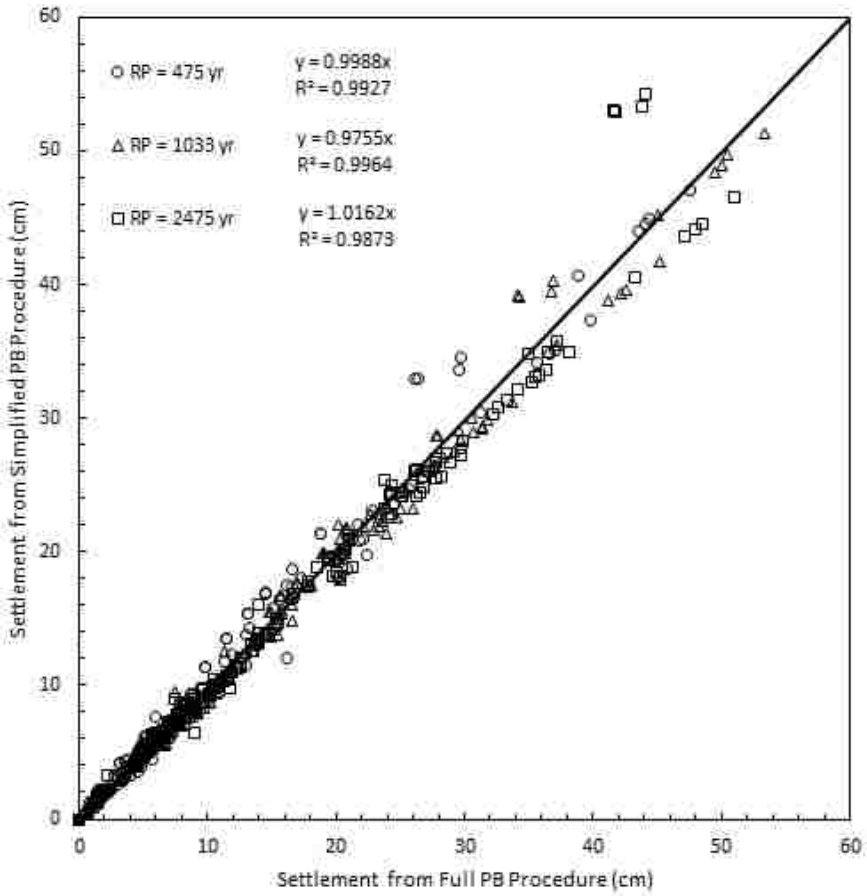

Figure 8-3: Boulanger and Idriss (2014) Full Performance-Based Settlement vs. Simplified Settlement Separated by Return Period (for *PGA* higher than 0.2g).

Overall, the simplified performance-based procedure is able to closely estimate the settlements calculated using the full performance-based procedure, but involves more scatter for cities with lower *PGA*. As shown in Figure 8-2, the trend lines have slopes between 0.9292 and 1.19 and R^2 values higher than 0.891. In Figure 8-3, the trend lines have slopes between 0.9755 and 1.0162 and R^2 higher than 0.9873. The high R^2 values indicates a strong relationship between the simplified and full performance-based results.

For cities with *PGA* lower than 0.2g, the simplified procedure was able to approximate the full performance-based procedure with less than 7cm of difference for all return periods and settlement ranges. For cities with *PGA* higher than 0.2g, the simplified procedure estimated the

total ground surface settlements within 4cm error when no more than 30cm of total settlement was predicted. Larger errors (i.e., 10cm) were observed in predicted total settlements larger than 30cm.

8.2.2 Validation of the Simplified Settlement Method Using Ku et. al (2012) Model

The validation plots for the Ku et. al (2012) triggering model are shown in Figure 8-4 and Figure 8-5, which present data from sites that have $PGA < 0.2g$ and $PGA > 0.2g$, repectively.

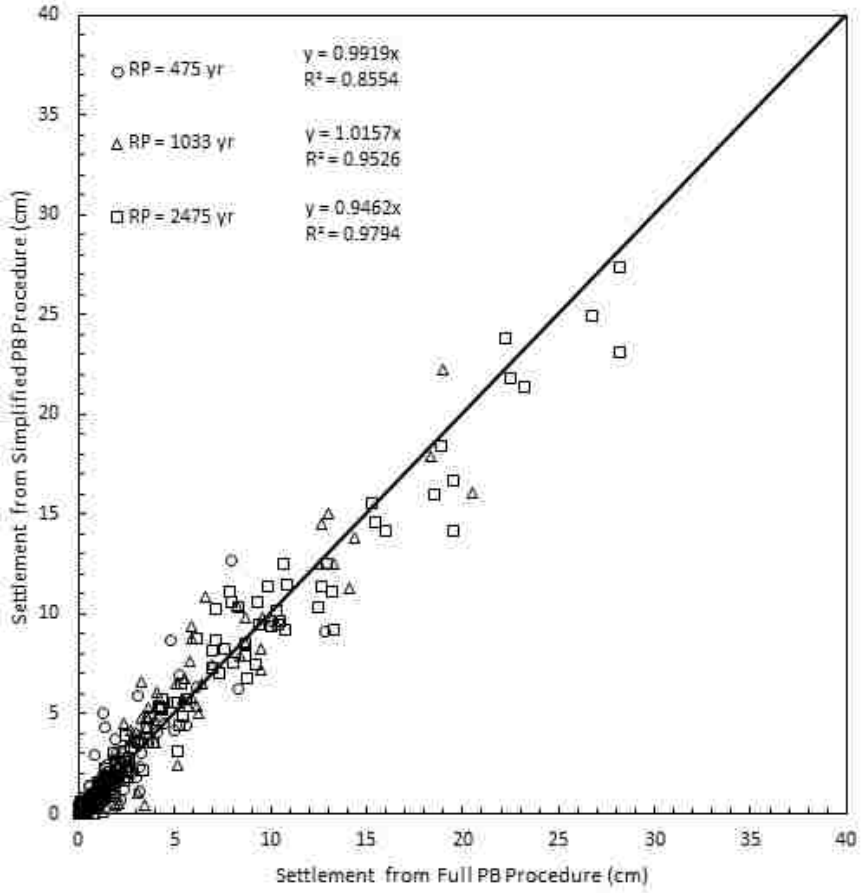

Figure 8-4. Ku et. al (2012) Performance-Based Total Settlement vs. Simplified Settlement Separated by Return Period (for *PGA* Lower than 0.2g).

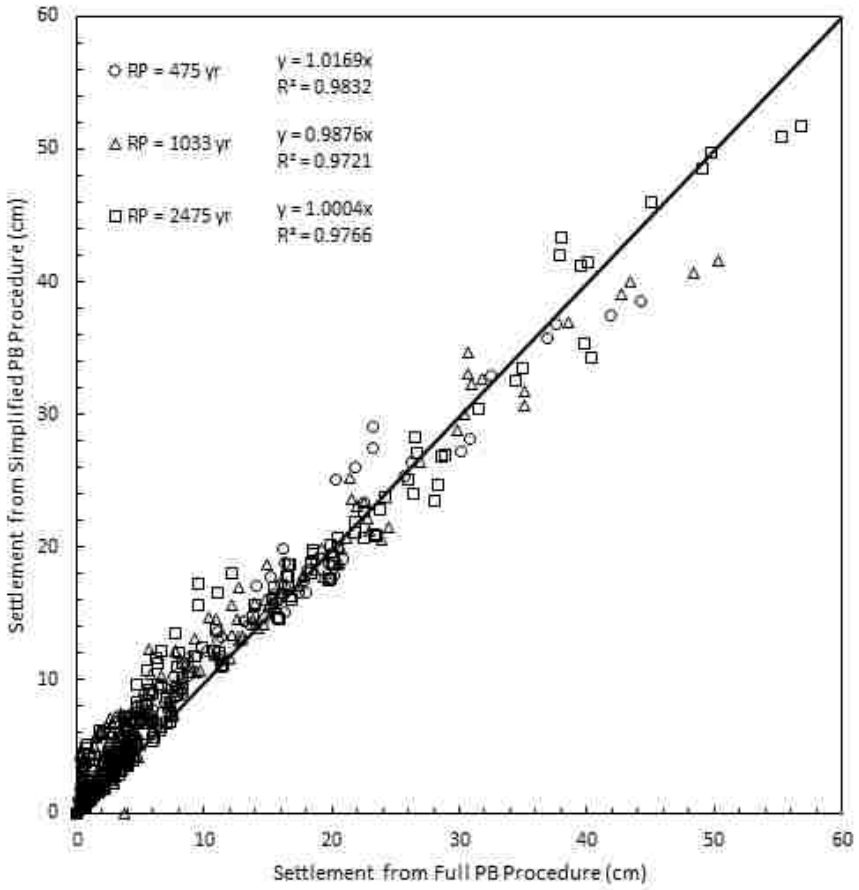

Figure 8-5: Ku et. al (2012) Performance-Based Total Settlement vs. Simplified Settlement Separated by Return Period (for *PGA* Higher than 0.2g).

8.3 Comparison of Using Pseudo-Probabilistic Results and Semi-Probabilistic Results to Obtain the Correction Factor

As part of the development of the simplified performance-based procedure, a comparison study was done to determine the best method for calculating the correction factor for volumetric strain, as shown in Equations (6-11) and (6-17). A semi-probabilistic method, where the volumetric strain is calculated using FS_L from the simplified performance-based triggering procedure, was used in the SPT simplified settlement procedure (Error, 2017). Thus, this study focused on comparing the resulting settlements using the correction factors that were computed

with semi-probabilistic and pseudo-probabilistic methods. The 20 profiles and 9 cities with *PGA* higher than 0.2g, which were described in Section 8.1, were used in this comparison study. The results are shown in Figure 8-6.

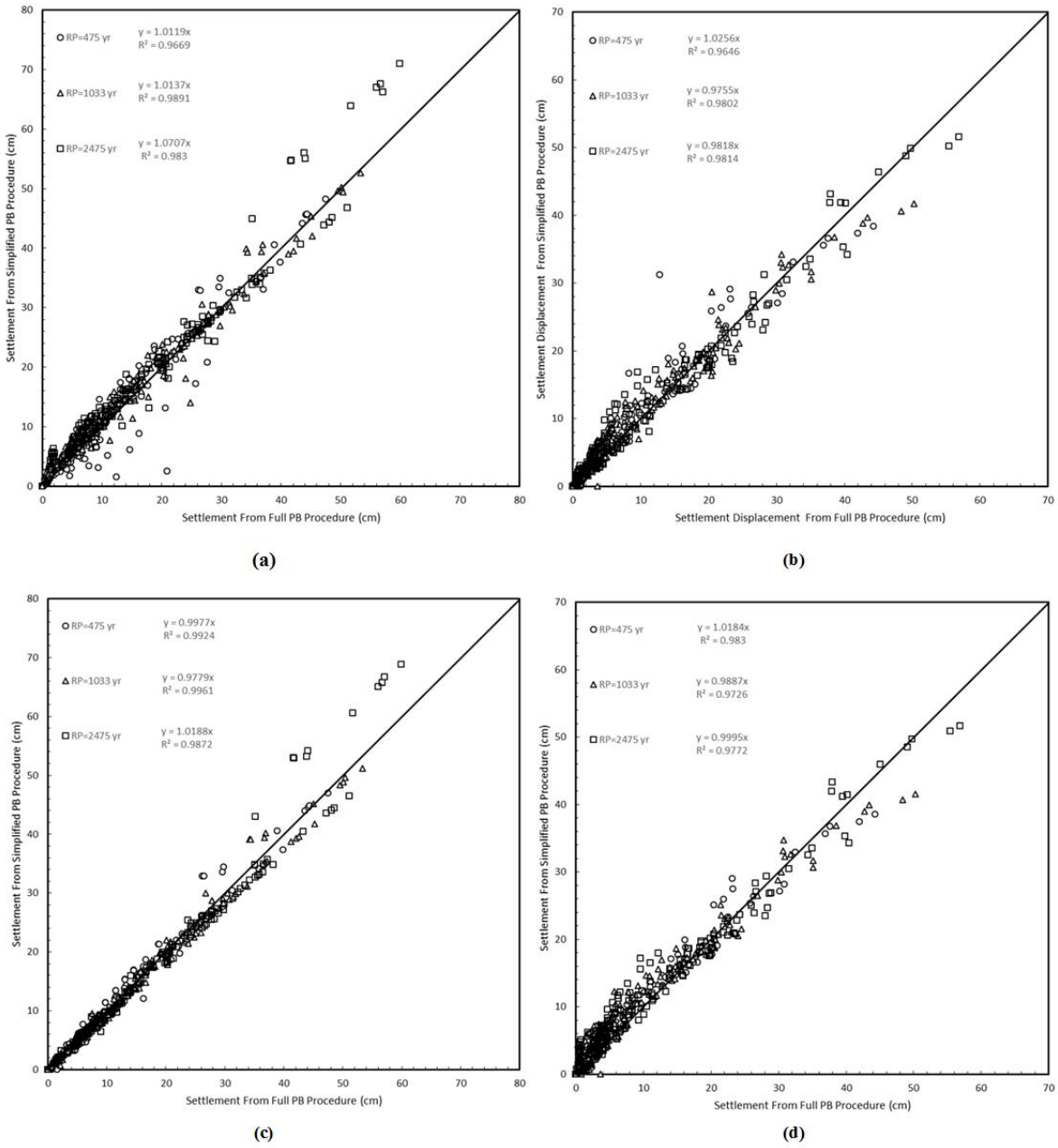

Figure 8-6. Comparative Scatter Plots for Simplified and Full Performance-Based Procedures Using (a) Semi-Probabilistic Results for B&I (2014), (b) Semi-Probabilistic Results for Ku (2012), (c) Pseudo-Probabilistic Results for B&I (2014) and (d) Pseudo-Probabilistic Results for Ku (2012) to Estimate the Correction Factor.

As shown in Figure 8-6, the bottom (pseudo-probabilistic) two plots have less scatter compared to the top (semi-probabilistic) two plots. These plots suggested that the pseudo-probabilistic approximation of $\Delta\varepsilon$ was able to better estimate the full performance-based settlement. Thus, the pseudo-probabilistic method was chosen over the semi-probabilistic method to obtain the correction factor for the volumetric strain.

8.4 Chapter Summary

The simplified performance-based procedures proposed in Chapter 6.2 were validated in this chapter by plotting the resulting settlements calculated from the full and the simplified performance-based procedures against each other. For both the Boulanger and Idriss (2014) and the Ku et al. (2012) triggering models, the simplified performance-based procedure was able to closely estimate the results from the full performance-based procedure. A comparison study was also shown to explain why the correction factors were calculated using pseudo-probabilistic method.

9 COMPARITIVE STUDY WITH THE TRADITIONAL METHOD

The ultimate goal of this study is to develop a simplified performance-based procedure that can be applied in routine design in a rapid manner, and also provide accurate approximates of the full performance-based procedure. The sample calculation performed in Section 6.3 has shown that the simplified performance-based procedure can be completed quickly with a simple spreadsheet. The purpose of this section is to compare the accuracy between the simplified performance-based procedure and the conventional pseudo-probabilistic procedure, which is used frequently in engineering practice. 12 cities (three cities in each mapped state) and 20 CPT profiles were used to compute post-liquefaction settlements using pseudo-probabilistic, simplified performance-based, and full performance-based procedures for return periods of 475, 1033 and 2475 years. All reference values, ε_v^{ref}, were retrieved from the reference parameter maps shown in Appendix A.

9.1 Locations and Profiles

The 12 sites chosen in this study were randomly selected from the four mapped states: CT, OR, SC, and UT, with three sites in each state. 8 out of these 12 sites have *PGA* lower than 0.2g, with the rest higher than 0.2g. Table 9-1 shows a list of the 12 sites with corresponding latitudes and longitudes and *PGA* at return period of 2475 years. The 20 CPT profiles presented in Figure 8-1 were also used for this comparison study.

Table 9-1: Sites Selected for Comparison Study.

State	Sites	Latitude	Longitude	PGA	Mean Magnitude
Oregon	Eugene	44.07531	-123.1323	0.3773	8.69
	Bend	44.07899	-121.3061	0.1748	7.11
	Mt. Vernon	44.40479	-119.1126	0.1386	6.22
Utah	Salt Lake City	40.755	-111.898	0.7261	6.8
	Frisco	38.39639	-113.0113	0.2188	6.23
	Moab	38.59779	-109.5475	0.1006	5.75
Connecticut	Hartford	41.77898	-72.6659	0.0995	5.64
	Stamford	41.07733	-73.56485	0.1607	5.49
	New Haven	41.31688	-72.9631	0.1114	5.58
South Carolina	Charleston	32.82052	-79.94348	0.9462	6.78
	Columbia	34.03673	-81.0377	0.189	6.14
	Florence	34.22184	-79.75401	0.189	6.81

9.2 Strain Reference Parameters

Different from the previous chapter, the liquefaction parameter maps (see Appendix A) were used to obtain the reference value, ε_v^{ref} for each site at their respective return period. This was done to assess the potential for interpolation of sites between the mapped grid points to bias the analysis results. The values of ε_v^{ref} used in this study are presented in Table 9-2 and Table 9-3.

Table 9-2: Mapped Values of ε_v^{ref} (%) for 12 Cities Using the Boulanger and Idriss (2014) Triggering Model.

State	Sites	Latitude	Longitude	Return Period (yrs)		
				475	1033	2475
Oregon	Eugene	44.0753	-123.1323	0.7	2.1	2.75
	Bend	44.079	-121.3061	0.04	0.49	1.8
	Mt. Vernon	44.4048	-119.1126	0	0.08	0.8
Utah	Salt Lake City	40.755	-111.898	1.72	2.4	3.2
	Frisco	38.3964	-113.0113	0.15	0.7	1.8
	Moab	38.5978	-109.5475	0	0	0.1
Connecticut	Hartford	41.779	-72.6659	0	0	0.031
	Stamford	41.0773	-73.56485	0	0.005	0.37
	New Haven	41.3169	-72.9631	0	0	0.09
South Carolina	Charleston	32.8205	-79.94348	1.63	2.3	2.95
	Columbia	34.0367	-81.0377	0	0.3	1.35
	Florence	34.2218	-79.75401	0	0.1	1.01

Table 9-3: Mapped Values of ε_v^{ref} (%) for 12 Cities Using the Ku et al. (2012) Triggering Model.

State	Sites	Latitude	Longitude	Return Period (yrs)		
				475	1033	2475
Oregon	Eugene	44.0753	-123.1323	0.49	1.56	2.28
	Bend	44.079	-121.3061	0.04	0.33	0.78
	Mt. Vernon	44.4048	-119.1126	0	0.04	0.35
Utah	Salt Lake City	40.755	-111.898	0.82	1.7	2.38
	Frisco	38.3964	-113.0113	0.08	0.19	0.52
	Moab	38.5978	-109.5475	0	0	0
Connecticut	Hartford	41.779	-72.6659	0	0	0.013
	Stamford	41.0773	-73.56485	0	0	0.048
	New Haven	41.3169	-72.9631	0	0	0.018
South Carolina	Charleston	32.8205	-79.94348	0.55	1.65	2.3
	Columbia	34.0367	-81.0377	0	0.1	0.47
	Florence	34.2218	-79.75401	0	0.05	0.48

9.3 Comparison with the Pseudo-Probabilistic Procedure

Post-liquefaction settlement calculations were performed for all 20 soil profiles and 12 selected sites at return periods of 475, 1033, and 2475 years using three procedures: pseudo-probabilistic, simplified performance-based, and full performance-based procedure. The simplifed performance-based post-liquefaction settlements were computed using the reference values shown in Table 9-2 and Table 9-3 and equations from Section 6.2. The pseudo-probabilistic and full performance-based post-liquefaction settlements were calculated in *CPTLiquefy* (Franke et al., 2017).

Settlements computed with the full performance-based procedure are plotted on the x-axis. Settlements calculated with the pseudo-probabilistic or the simplified performance-based procedure are plotted on the y-axis. The comparison between the simplified performance-based procedure and the pseudo-probabilistic procedure is based on two main criteria: the slopes of the trend lines and the R^2 values. The data with a trend line slope closer to 1.0 is better at

approximating of the full performance-based procedure on average, and the data with the larger R^2 value is more consistent (i.e., precise) in its predictions.

9.3.1 Comparison Results Using the Boulanger and Idriss (2014) Triggering Model

The comparison results of all three return periods for the Boulanger and Idriss (2014) triggering model are presented in Figure 9-1 and Figure 9-2. Figure 9-1 contains sites with PGA lower than 0.2g, and Figure 9-2 contains sites with PGA higher than 0.2g.

For all return periods, both the simplified performance-based procedure and the pseudo-probabilistic procedure, more scatter is observed for sites with *PGA* less than 0.2g (Figure 9-1). This observation agrees with the validation study presented in Section 8.2. At sites with *PGA* < 0.2g (Figure 9-1), slopes of the trend lines are 1.0545 and 1.2398 for the simplified procedure and the pseudo-probabilistic procedure, respectively, suggesting that, on average, the simplified performance-based procedure is over-predicting the full performance-based procedure by 5.5% and the pseudo-probabilistic method is over-predicting by 24.0%. Considering the R^2 values, both set of data produce a R^2 value around 0.925. Similarly, results at sites with PGA $\geq$ 0.2g (Figure 9-2) show that the simplified procedure underestimates the full performance-based procedure by 3.2% and the pseudo-probabilistic underestimates by 10.3%. The simplified performance-based procedure also has a slightly higher R^2 value (0.9729) than the pseudo-probabilistic procedure (0.9515), though such small difference is usually negligible.

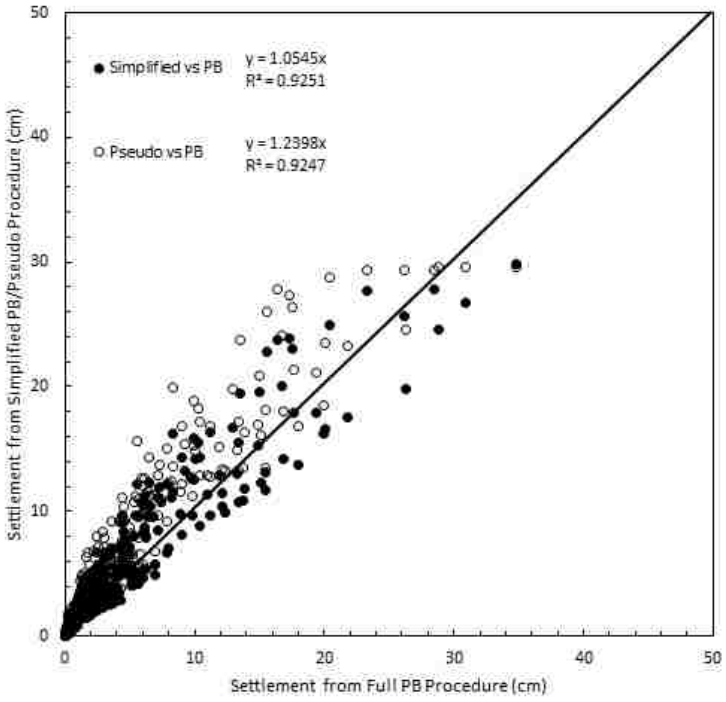

Figure 9-1: Comparison Results using the Boulanger and Idriss (2014) Triggering Model for Sites with *PGA* < 0.2g (for All Return Periods).

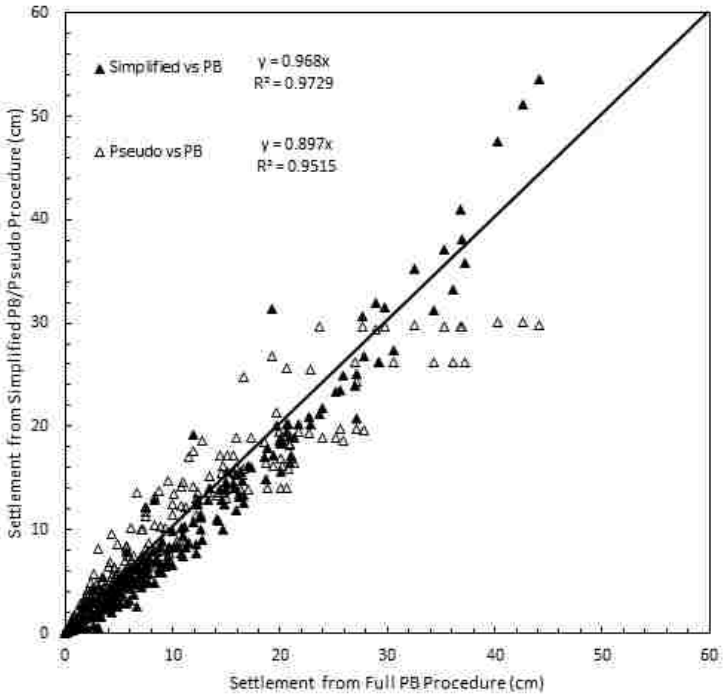

Figure 9-2: Comparison Results using the Boulanger and Idriss (2014) Triggering Model for Sites with *PGA* ≥ 0.2g (for All Return Periods).

Overall, both the simplified performance-based procedure and the pseudo-probabilistic procedure overestimate the full performance-based procedure for sites with *PGA* < 0.2g (i.e., low seismicity areas), and underestimate for PGA ≥ 0.2g (i.e., moderate to high seismicity areas). However, the simplified performance-based procedure more accurately approximates of the full performance-based procedure on average, and is slightly more consistent and precise than the pseudo-probabilistic procedure based on the comparisons performed in this study.

9.3.2 Comparison Results Using the Ku et al. (2012) Triggering Model

The comparison plots based on using the Ku et al. (2012) triggering model are shown in Figure 9-3 and Figure 9-4, with Figure 9-3 containing sites with *PGA* less than 0.2g and Figure 9-4 containing sites with *PGA* greater than or equal to 0.2g.

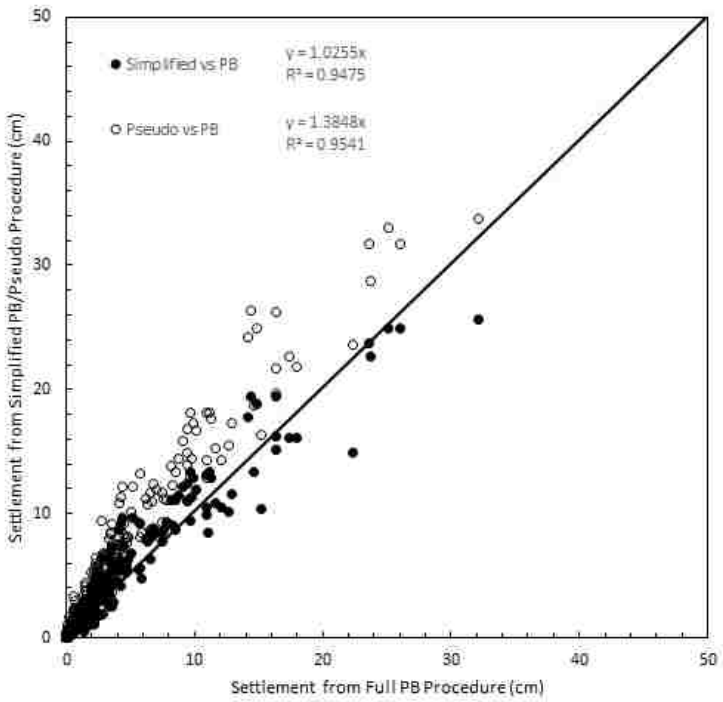

Figure 9-3: Comparison Results using the Ku et al. (2012) Triggering Model for Sites with *PGA* < 0.2g (for All Return Periods).

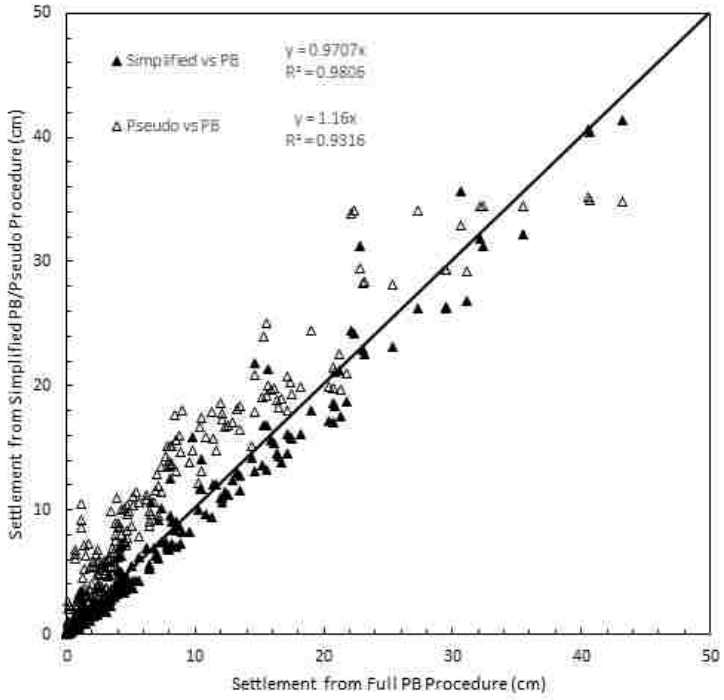

Figure 9-4: Comparison Results using the Ku et al. (2012) Triggering Model for Sites with *PGA* ≥ 0.2g (for All Return Periods).

As observed with the Boulanger and Idriss (2014) model, the simplified performance-based procedure with the Ku et al (2012) model produced better approximations of the full performance-based procedure and was slightly more consistent and precise than the pseudo-probabilistic procedure..

9.4 Discussion

Although the trend line slopes and R^2 values presented in Section 9.3 suggest that the simplified performance-based procedure can consistently provide better and more consistent approximations of the full performance-based procedure, there are not visually obvious differences between results from the simplified performance-based and the conventional pseudo-probabilistic procedures.

These apparent similarities can be explained. Studies have shown that the performance-based procedure generally deviates significantly from the pseudo-probabilistic procedure in liquefaction triggering (Kramer and Mayfield, 2007; Franke et al., 2013). However, these significant differences in comooputed FS_L are not fully transferred to the resulting volumetric strains, computed using Ishihara and Yoshimine (1992).

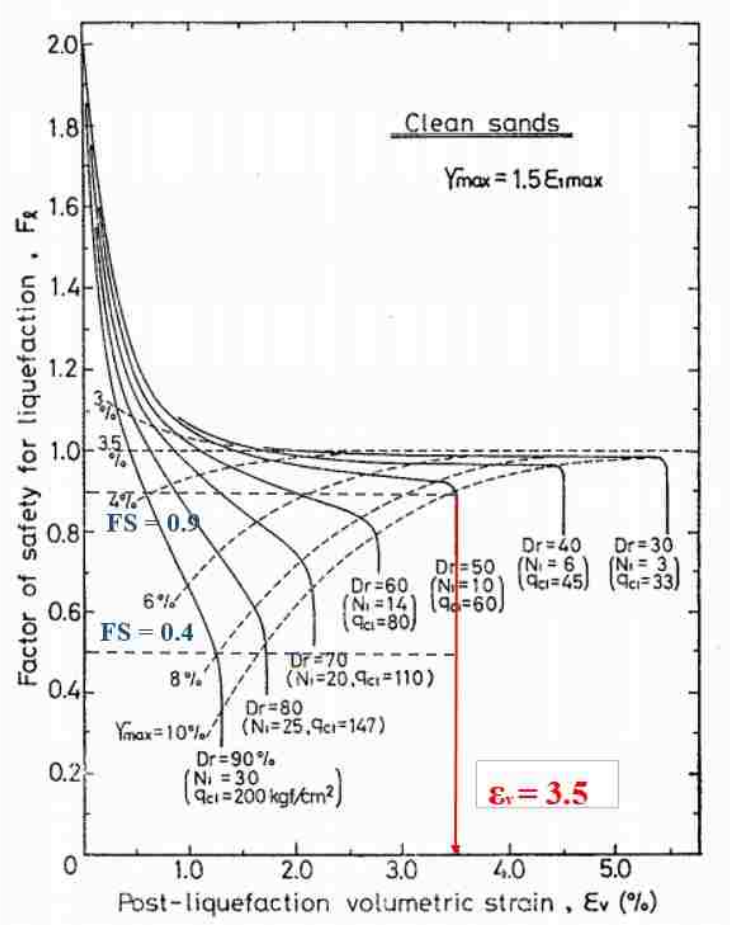

Figure 9-5: Ishihara and Yoshimine (1992) Method for Determining Volumetric Strain.

Consider, for example, two different values of FS_L (0.9 and 0.5) and the resulting volumetric strains from Ishihara and Yoshimine (1992) presented in Figure 9-5. Each of the FS_L values although significantly different, is predicted to result in approximately the same amount of

volumetric strain: 3.5%. As such, significant differences in computed FS_L between the simplified performance-based procedure and the pseudo-probabilistic procedure may not transfer to significant differences in volumetric strain when using the Ishihara and Yoshimine (1992) volumetric strain curves. Consequently, the resulting post-liquefaction settlements computed using the two different procedures can appear quite similar.

Regardless, engineers in practice may ask "why should we use the simplified performance-based procedure over the conventional pseudo-probabilistic procedure that we are already applying when no obvious improvements seem to have been made?" In response to this question, the simplified performance-based procedure clearly demonstrated trend line slope that is closer to 1.0 and larger R^2 values than the conventional pseudo-probabilistic procedure, indicating that it is better at approximating the full performance-based approach and is slightly more precise and consistent than the conventional pseudo-probabilistic approach. Engineers may certainly choose if they would like to benefit from the increased accuracy, consistency, and precision of the simplified performance-based approach or continue using the approach that they are already familiar with.

9.5 Chapter Summary

A study was performed to evaluate the accuracy and consistency of the simplified performance-based procedure by comparing it to the pseudo-probabilistic procedure. Resulting plots show that, on average and for all seismicity levels and return periods, the simplified performance-based procedure is able to better approximate the results of the full performance-based procedure with more consistency and precision.

10 CONCLUSION

Earthquake-induced liquefaction can cause severe damage to infrastructure and has been closely studied during the past 50 years. Post-liquefaction settlement due to volumetric strain, which is a manifestation of soil densification, is one of the common effects of soil liquefaction. Devastating economic losses caused by settlement have driven engineers and researchers to seek better ways to predict and quantify post-liquefaction settlement. Performance-based earthquake engineering (PBEE) has been developed to perform a more consistent, complete, and objective liquefaction hazard analysis, and it has been applied to the evaluation of post-liquefaction settlement. Unfortunately, the full performance-based procedure is complex and can be difficult for engineers to use on routine design projects.

Previous studies have shown that a simplified performance-based procedure can be developed to combine the simplicity of the traditional pseudo-probabilistic procedure and the accuracy of the full performance-based procedure. These simplified performance-based procedures have been developed for SPT calculations. The purpose of this thesis was to derive and validate a simplified performance-based procedure for post-liquefaction settlement using CPT. The following steps were taken to fulfill this purpose:

1) Derivation of the simplified performance-based procedure. The derivation included finding correction equations that would adjust a reference value, ε_v^{ref}, to reflect site-specific conditions, ε_v^{site}.

2) Performing a grid spacing study. The USGS 2014 *PGA* map was used to establish a relationship between *PGA* ranges and the optimum grid spacing. The distance between grid points were selected such that no more than 0.1% absolute error was allowed in a parameter map.
3) Development of the liquefaction parameter map. Post-liquefaction calculations were performed at the grid points using a full performance-based procedure. Contours maps were then created for the interpolated ε_v^{ref} values. Liquefaction parameter maps were made for four states: Connecticut, Oregon, South Carolina, and Utah.
4) Validation of the simplified performance-based procedure. Overall, the simplified performance-based procedure can reasonably estimate the results of the full performance-based procedure, with more apparent scatter in lower seismicity areas (*PGA* < 0.2g).

Based on the comparative study performed in this research, the simplified performance-based procedure for estimating free-field post-liquefaction settlements is a more accurate and consistent approximator of the full performance-based procedure than the conventional pseudo-probabilistic procedure used frequently by engineers today. The author recommends the application of the simplified performance-based procedure in engineering design rather than the pseudo-probabilistic procedure.

REFERENCES

Abrahamson, N., & Litehiser, J. (1989). Attenuation of Vertical Peak Acceleration. *Bulletin of the Seismological Society of America, 79*, 549-580.

Abrahamson, N., & Silva, W. (2008). Summary of the Abrahamson & Silva NGA Ground-Motion Relations. *Earthquake Spectra: February 2008, 24*(1), 67-97.

Abrahamson, N., Silva, W., & Kamai, R. (2014). Summary of the ASK14 Ground Motion Relation for Active Crustal Regions. *Earthquake Spectra, 30*(3), 1025-1055.

Ambraseys, N. (1988). Engineering seismology. *Earthquake Engineering and Structural Dynamics, 17*, 1-105.

Been, K., & Jefferies, M. (1985). A State Parameter for Sands. *Geotechnique, 35*(2), 99-112.

Bolt, B. A. (1969). Duration of Strong Motion. *Paper Presented at the 4th World Conference on Earthquake Engineering.* Santiago, Chile.

Boore D. M., Stewart, J., Seyhan, E., & Atkinson, G. (2014). NGA-West2 Equations for Predicting PGA, PGV, and 5% Damped PSA for Shallow Crustal Earthquakes. *Earthquake Spectra, 30*(3), 1057-1085.

Boore, D., & Atkinson, G. (2008). Ground-Motion Prediction Equations for the Average Horizontal Component of PGA, PGV, AND 5%-Damped PSA at Special Periods between 0.01 s and 10.0 s. *Earthquake Spectra: February 2008, 24*(1), 99-138.

Boulanger, R. W. (2003a). Relating Ka to Relative State Parameter Index. *Journal of Geotechnical and Geoenvironmental Engineering, 129*(8), 770-773.

Boulanger, R., & Idriss, I. (2014). *CPT and SPT Based Liquefaction Triggering Procedures.* University of California, Center for Geotechnical Modeling, Department of Civil and Environmental Engineering, Davis, CA. Report No. UCD/CGM-14/01.

Bozorgnia, Y. (2014). NGA-West2 Research Project. *Earhquake Spectra, 30*(3), 973-987.

Bray, J., & Dashti, S. (2014). Liquefaction-Induced Building Movements. *Bulletin of Earthquake Engineering*, 1129-1156.

Cambell, K., & Bozorgnia, Y. (2008). NGA Ground Motion Model for the Geometric Mean Horizontal Component of PGA, PGV, PGD, and 5% Damped Linear Elastic Reponse

Spectra for Periods Ranging from 0.01 s to 10 s. *Earthquake Spectra: February 2008, 24*(1), 139-171.

Campbell, K. (1985). Strong Ground Motions Attenuation Relations: A Ten-Year Perspective. *Earthquake Spectra, 1*(4), 759-804.

Campbell, K. W. (1981). Near source attenuation of peak horizontal acceleration. *Bulletin of the Seismological Society of America*, 2039-2070.

Campbell, K., & Bozorgnia, Y. (2014). NGA Ground Motion Model for the Geometric Mean Horizontal Compenent of PGA, PGV, PGD and 5% Damped Linear Elastic Response Spectra for Periods Ranging from 0.01 to 10 s. *Earhquake Spectra, 30*(3), 1089-1116.

Castro, G. &. (1977). Factors Affecting Liquefaction and Cyclic Mobility. *Journal of the Geotechnical Engineering Division, 106*(GT6), 501-506.

Chang, K. T. (1978). An Anlysis of Damage of Slope Sliding by Earthquake on the Paiho Main Dam and its Earthquake Strengthening. En D. o.-R. Reservoir, *Tseng-hua Design Section.* Peoples Republic of China.

Chiou, B.-J., & Youngs, R. (2008). A NGA Model for the Average Horizontal Component of Peak Groud Motion Response Spectra. *Earthquake Spectra: February 2008, 24*(1), 173-215.

Chiou, B.-J., & Youngs, R. (2014). Update of the Chious and Youngs NGA Model for the Average Horizontal Component of Peak Ground Motion and Response Spectra. *Earthquake Spetra, 3*, 1117-1153.

Coulter, M. &. (1966). Effects of the Earthquake of March 27, 1965 at Valdez, Alaska. *Professional Paper 542-C*.

Dashti, S., Bray, J., Pestana, J., Riemer, M., & Wilson, D. (2010). Mechanisms of Seismically Induced Settlement of Buildings with Shallow Foundations on Liquefiable Soil. *Journal of Geotechnical and Geoenvironmental Engineering, 135*(1).

Ekstrom, L. T. (2015). *A Simplified Procedure for the Performance-Based Prediction of Lateral Spread Displacement.* Provo, Utah: Brigham Young University.

Error, B. M. (2017). *Development of a Simplified Performance-Based Procedure for the Assessment of Liquefaction-Induced Settlement Using Liquefaciton Loading Maps.* Provo, Utah: Brigham Young University.

Evans, M. D. (1987). *Undrained Cyclic Triaxial Testing of Gravel: the Effect of Membrane Compliance.* University of California, Berkeley, Earthquake Engineering Research Center. California: Report UCB/EERC-87/08.

GmbH, B. M. (2012). Ground Improvement by Depth Vibrator. 80.

Golesorkhi, R. (1989). *Factors Influencing the Computational Determination of Earthquake-Induced Shear Stress in Sandy Soils.* University of California at Berkely.

Goulet, C. A. (2014). *PEER NGA-East Database.* Berkeley, California: Pacific Earhquake Engineering Research Center.

Hanks, T. C., & Kanamori, H. (1979). A moment magnitude scale. *Journal of Geophysical Research, 84*, 2348-2350.

Hanzawa, H., Itoh, Y., & Suzuki, K. (1979). Shear Characteristics of a Quick Sand in the Arabian Gulf. *Soils and Foundations, 19*(4), 1-15.

Hatch, M. S. (2017). Development of a Performance-Based Procedure to Predict Liquefaction-Induced Free-Field Settlements for the Cone Penetration Test. *M.S. Thesis.* Provo, Utah: Brigham Young University.

Idriss, I. M. (2008). An NGA Empirical Model for Estimating the Horizontal Spectral Values Generated By Shallow Crustal Earthquakes. *Earthquake Spectra: February 2008, 24*(1), 217-242.

Idriss, I. M. (2014). An NGA-West2 Empirical Model for Estimating the Horizontal Spectral Values Generated by Shallow Crustcal Earthquakes. *Earthquake Spectra, 30*(3), 1155-1177.

Ishihara, K., & Nagase, H. (1988). Multi-directional Irregular Loading Tests on Sand. *Soil Dynamics and Earthquake Engineering, 7*(4), 201-212.

Ishihara, K., & Yoshimine, M. (1992). Evaluation of Settlements in Sand Deposits Follwing Liquefaction During Earhquakes. *Soils and Foundations, 32*(1), 173-188.

Jefferies, M. G., & Davies, M. (1993). Use of CPT to Estimate Equivalent SPT N60. *Geotechnical Testing Journal, 16*(4).

Jennings, P. C. (1985). Ground Motion Parameters that Influence Structural Damage. *Earthquake Engineering Institute*.

Joyner, W. B. (1988). Measurement, Characterization, and Prediction of Strong Ground Motion. *Earthquake Engineering and Soil Dynamics II - Recent Advances in Ground-Motion Evaluation*, 43-102.

Joyner, W. B., & Boore, D. M. (1988). Measurement, characterization, and prediction of strong ground motion. *ASCE* (págs. 43-102). New York: Geotechnical Special Publication 20.

Juang, C. H., Ching, J., Wang, L., Khoshnevisan, S., & Ku, C. -S. (2013). Simplified Procedure for Estimation of Liquefaction-Induced Settlement and Site-Specific Probabilistic Settlement Exceedance Curve Using Cone Penetration Test. *Canadian Geotechnical Journal, 50*(10), 1055-1066.

Kanamori, H. (1977). The Energy Release in Great Earthquakes. *Journal of Geophysical Research, 82*, 2981-2987.

Kishida, T. e. (2017). Development of the NGA-Subduction Database. *16th World Conference on Earthquake, 16WCEE 2017*.

Kokusho, T., & Nagasaki. (1984). Settlement Characteristics of Dense Sands Following Liquefaction. *Proc. 19th Annual Convention of Japan Society of Soil Mechanics and Foundation Engineering*, (págs. 563-566).

Kramer, S. L. (1996). *Geotechnical Earthquake Engineering.* Upper Saddle River, New Jersey: Prentice-Hall, Inc.

Ku, C., Juang, C., Chang, C., & Ching, J. (2012). Probabilistic Version of the Robertson and Wride Method for Liquefaction Evaluation: Development and Application. *Canadian Geotechnical Journal, 49*(1), 27-44.

Liao, S., & Whitman, R. (1986). *A Catalog of Liquefaction and Non-Liquefaction Occurrences during Earthquakes.* Massachusetts Institute of Technology, Department of Civil Engineering. Cambridge, Mass: ASCE.

Moehle, J, & Deierlein, G. (2004). A Framework Methodology for Performance-based Earthquake Engineering. *13th World Conference on Earthquake Engineering*, (pág. 679). Vancouver, B.C., Canada.

Mogami, T., & Kubo, K. (1953). The behavior of soil during vibration. *Proceedings, 3rd International Conference on Soil Mechanics and Foundation Engineering*, *1*, págs. 152-155. Zurich.

Musson, T. (February de 2011). *Timothy Musson.* Obtenido de flickr: https://www.flickr.com/photos/37990418@N08/5476123346

Niigata Earthquake, 1964. (s.f.). *Proceedings of the 3rd World Conference in Earthquake Engineering. 3*, págs. 78-105. Japan Natioanl Committee on Earthquake Engineering.

Orense, R. P. (2011). Soil Liquefaction during the 2010 Darfield and 1990 Luzon Earthquakes: a Comparative Study. *Proceedings of the Ninth Pacific Conference on Earthquake Engineering.* Auckland, New Zealand: Building an Earthquake-Resilient Society.

Poulos, S. J. (1981). The Steady State of Deformation. *Journal of the Geotechnical Engineering Division, 107*(GT5), 553-562.

Reiter, L. (1990). *Earthquake Hazard Analysis - Issues and Insights.* New York: Columbia University Press.

Robertson, P. K. (1990). Soil Classification Using the Cone Penetration Test. *Canadian Geotechnical Journal*, 27.

Sasaki, T., Tatsuoka, F., & Yamada, S. (1982). Method of Predicting Settlements of Sandy Ground Following Liquefaction. *Proc. 17th Annual Convention of Japan Society of Soil Mechanics and Foundation Engineering*, (págs. 1661-1664).

Seed, H. B., & Idriss I. M. (1971). Simplified Procedure for Evaluating Soil Liquefaction Potential. *Journal of Soil Mechanics and Foundations Div.*

Seed, H., & Lee, K. (1966). Liquefaction of Saturated Sands during Cyclic Loading. *Journal of the Soil Mechanics and Foundation Division, 92*(SM6), 105-134.

Silver, N., & Seed, H. (1971). Volume Changes in Sands During Cyclic Loading. *Journal of the Soil Mechanics and Foundations Divison, 97*(SM9), 1171.

Tatsuoka, F., Sasaki, T., & Yamada, S. (1984). Settlement in Saturated Sand Induced by Cyclic Undrained Simple Shear. *Eighth World Conference on Earthquake Engineering*, *III*, págs. 95-102. San Francisco.

Tatsuoka, F., Zhou, S., Sato, T., & Shibuya, S. (s.f.). *Evaluation Method of Liquefaction Potential and its Application.* Ministry of Education of Japan, Report on Seismic Hazards on the Ground in Urban Areas, Tokyo.

Ulmer, K. J. (2015). *Development of a Simplified Performance-Based Procedure for Assessment of Liquefaction Triggering Using Liquefaction Loading Maps.* Provo, Utah: Brigham Young University.

USGS. (s.f.). *Magnitude/Intensity Comparison*. Obtenido de USGS: http://earthquake.usgs.gov/learn/topics/mag_vs_int.php

Vaid, Y., & Chern, J. (1983). Effect of Static Shear on Resistance of Liquefaction. *Soils and Foundations, 23*(1), 47-60.

Wong, R. T. (1975). Liquefaction of Gravelly Soil Under Cyclic Loading Conditions. *Journal of the Geotechnical Engineering Division, 101* (GT6), 571-583.

Wong, W. (1984). Earthquake Damages to Earth Dams and Levees in Relation to Soil Liquefaction and Weakness in Soft Clays. *Proceedings, International Conference on Case Histories in Geotechnical Engineering*, *1*, págs. 511-521.

Yegian, M. K. (1994). Liquefaction and Embankment Failure Case Histories, 1988 Armenai Earthquake. *Journal of Geothnical Engineering, 120*(3), 581-596.

Youd, T. (1984). Recurrence of liquefaction at the same site. *Proceedings, 8th World Conference on Earthquake Engineering*, *3*, págs. 231-238.

Youd, T. L. (s.f.). The Borah Peak, Idaho Earthquakeof October 28, 1983 - Liquefaction. *Earthquake Spectra, 2*(1), 71-89.

Youd, T. L., & Idriss, I. M. (2001). Liquefaction Resistance of Soils: Summary Report from the 1996 NCEER and 1998 NCEER/NSF Workshops on Evaluation of Liquefaction Resistance of Soils. *Journal of Geotechnical and Geoenvironmental Engineering, 127*(10), 817-833.

Youd, T., & Hoose, S. (1977). Liquefaciton Susceptibility and Geologic Setting. *Proceedings of 6th World Conference on Earthquake Engineering*, (págs. 37-42). New Delhi, India.

Youngs, R., Day, S., & Stevens, J. (1988). Near field ground motions on rock for large subduction earthquakes. *Proceedings, Earthquake Engineering and Soil Dynamics II: Recent Advances in Ground Motion Evaluation*, 445-462.

APPENDIX A. SAMPLE LIQUEFACTION PARAMETER MAPS

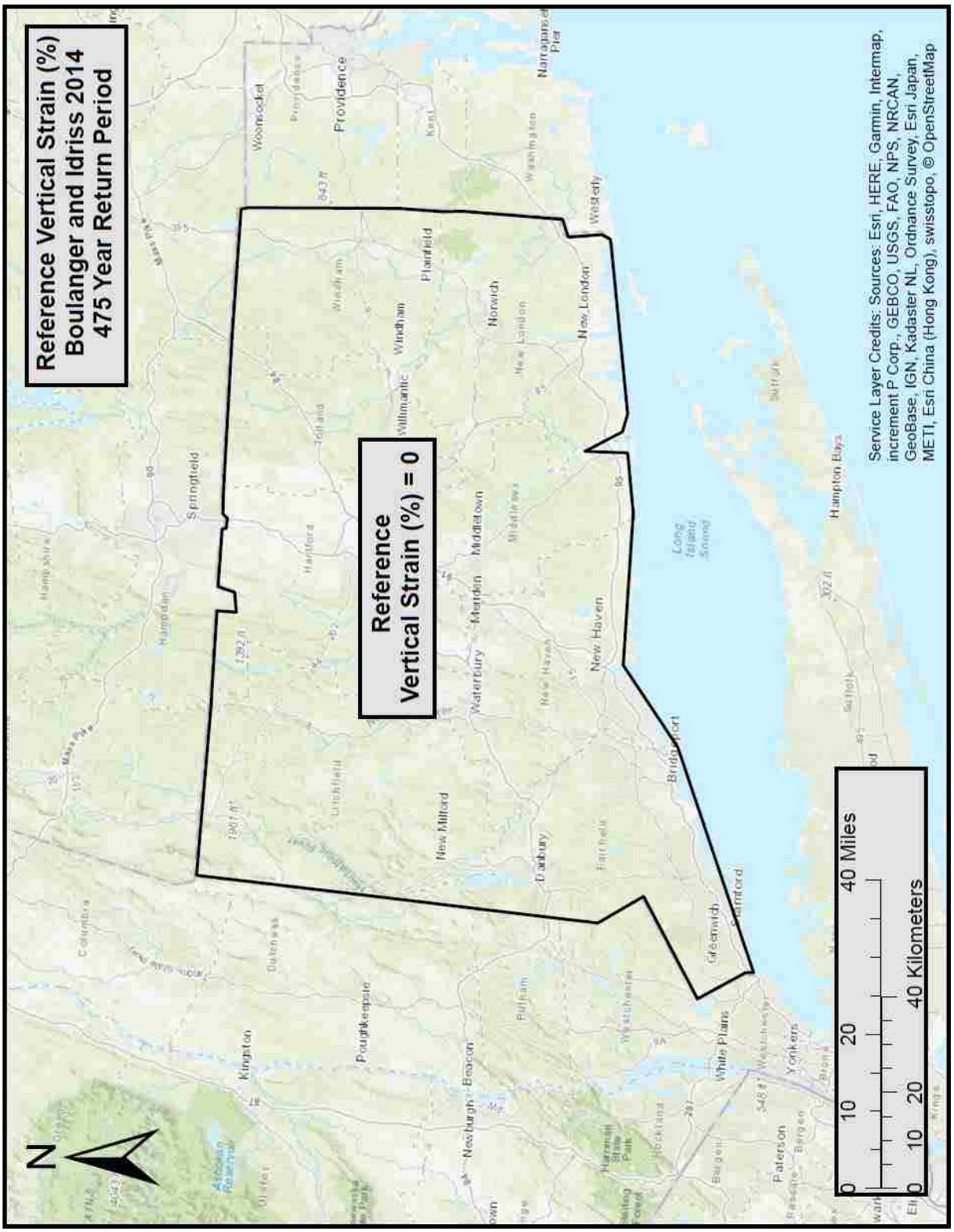

Figure A-1: Boulanger and Idriss (2014) Volumetric Strain Parameter Map for Conneticut (Tr = 475).

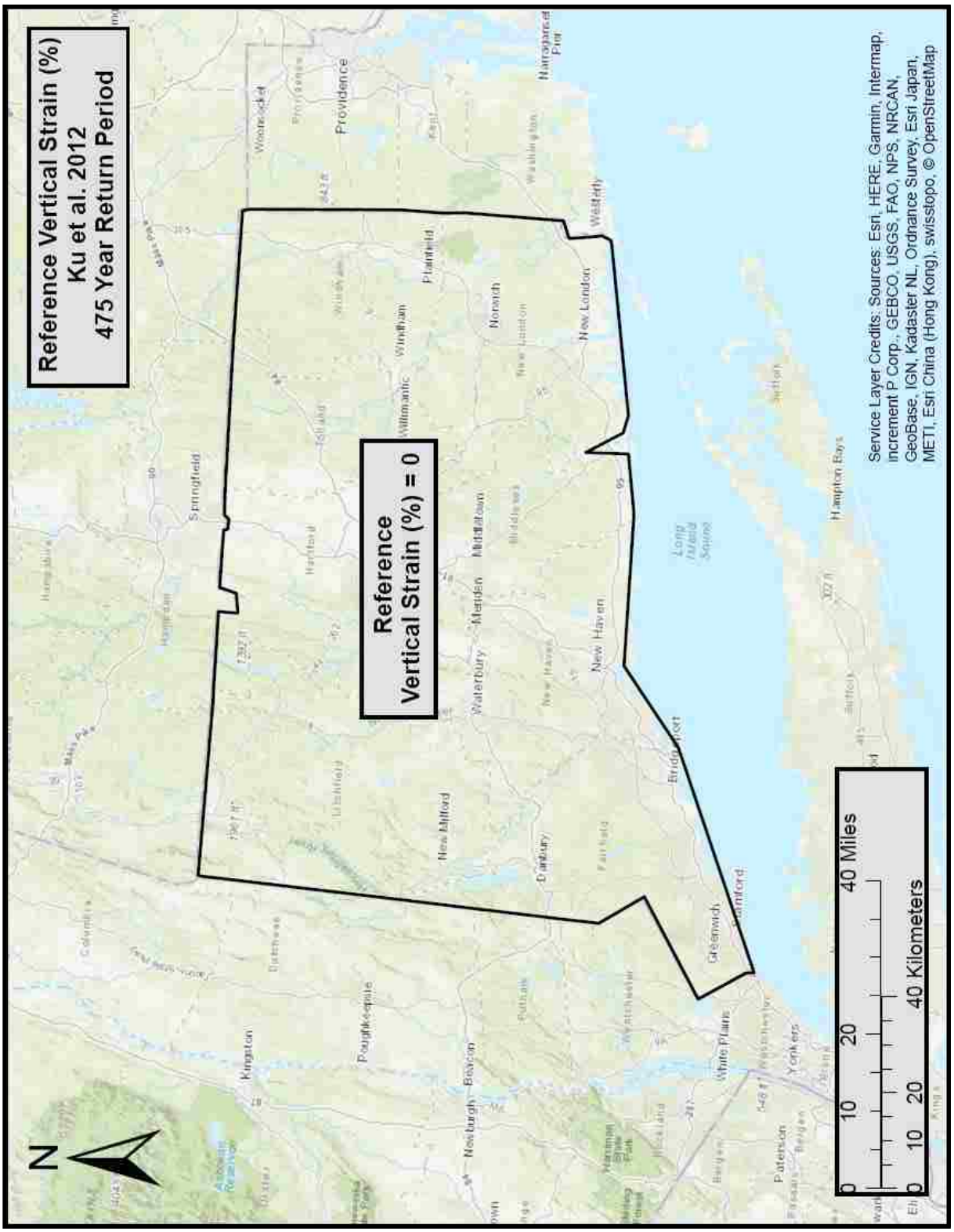

Figure A-2: Ku et al. (2012) Volumetric Strain Parameter Map for Conneticut (Tr = 475).

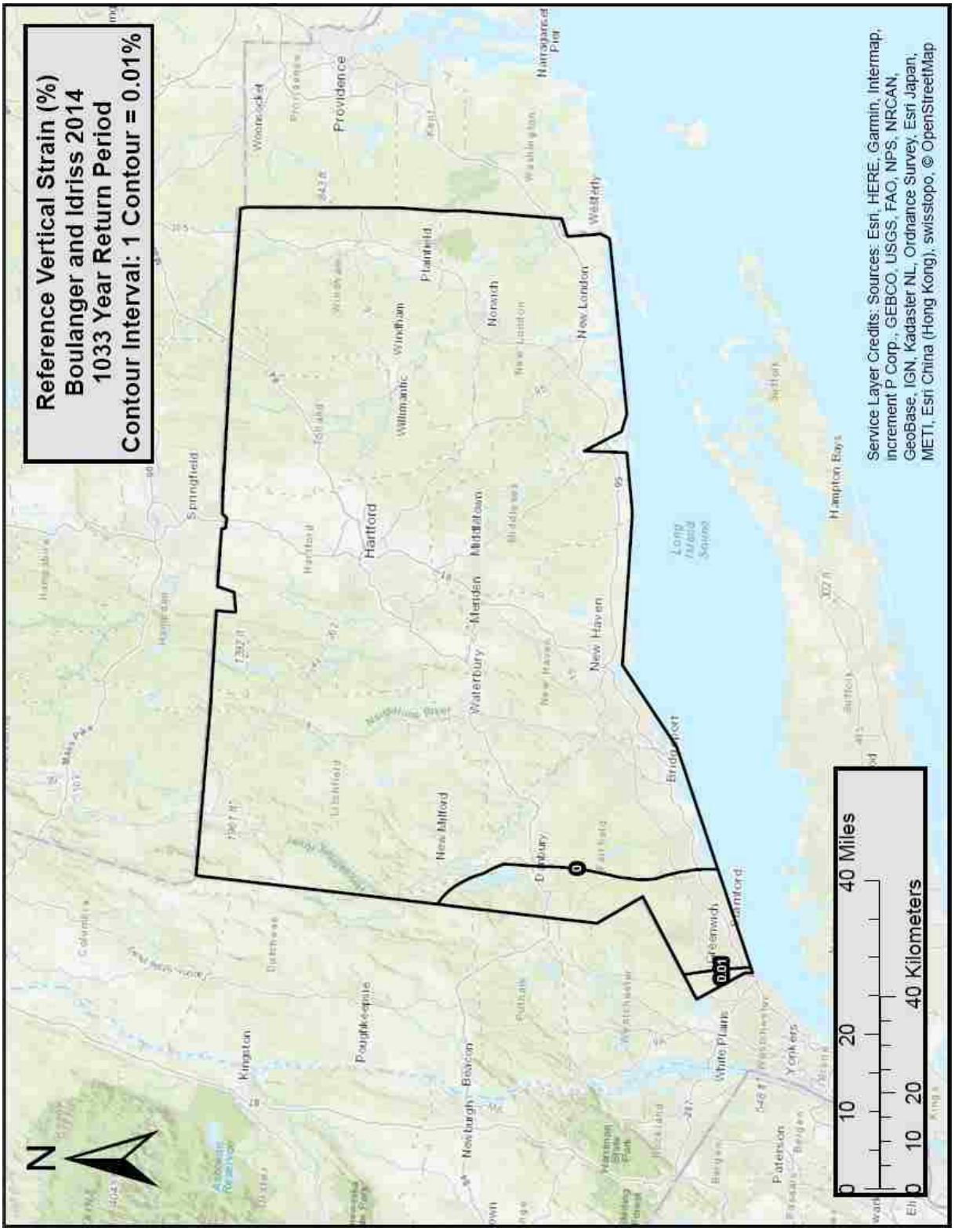

Figure A-3: Boulanger and Idriss (2014) Volumetric Strain Parameter Map for Conneticut (Tr = 1033).

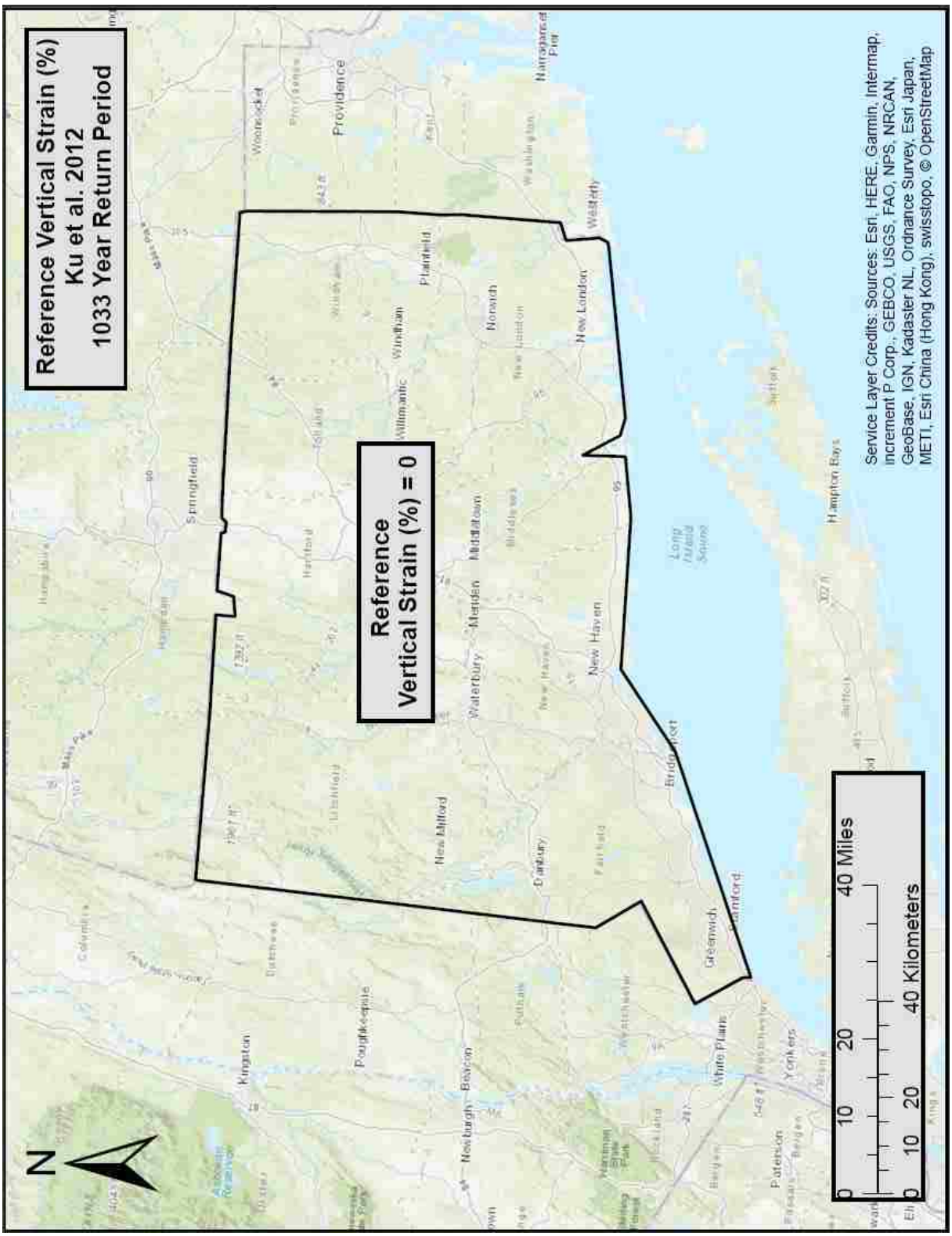

Figure A-4: Ku et al. (2012) Volumetric Strain Parameter Map for Conneticut (Tr = 1033).

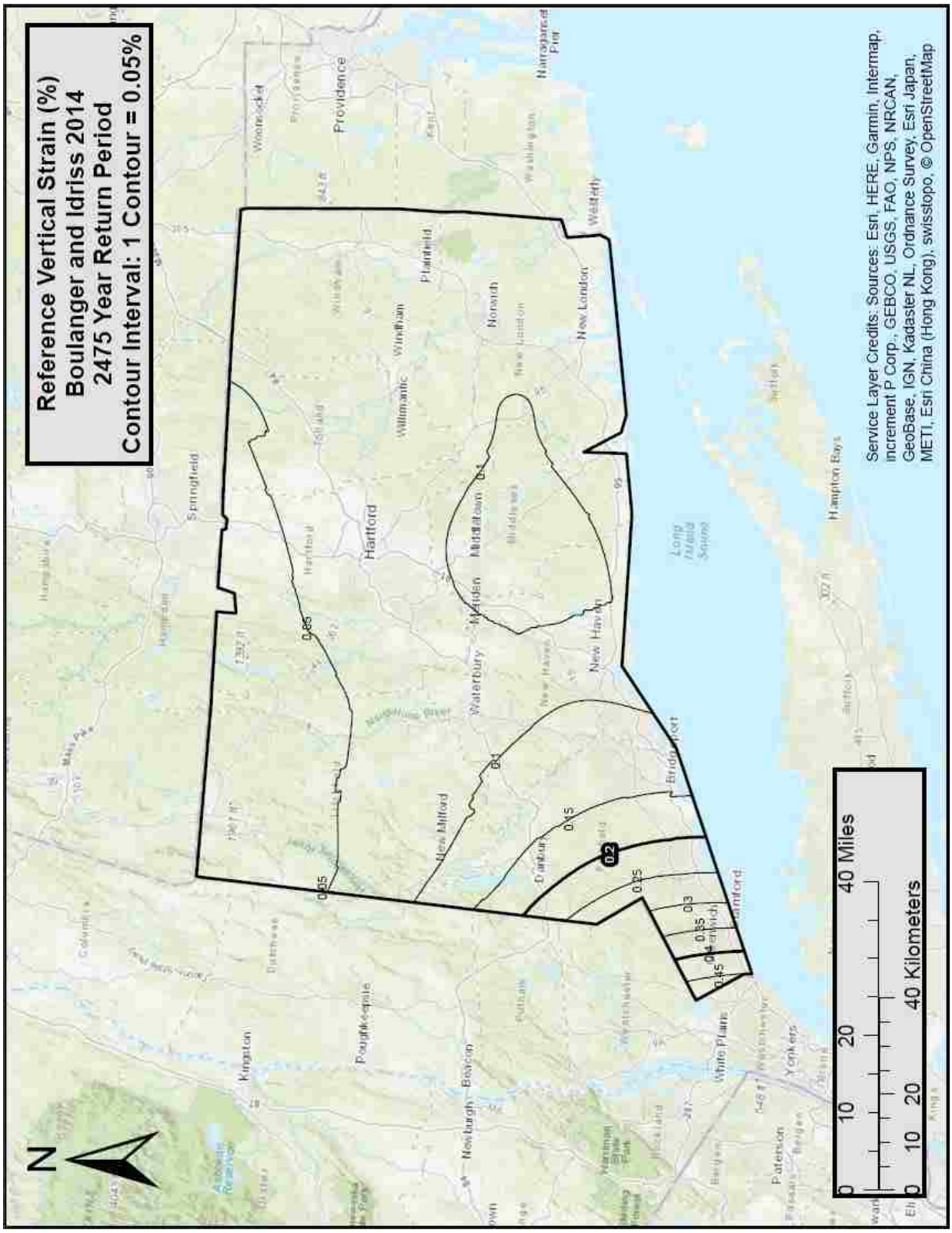

Figure A-5: Boulanger and Idriss (2014) Volumetric Strain Parameter Map for Conneticut (Tr = 2475).

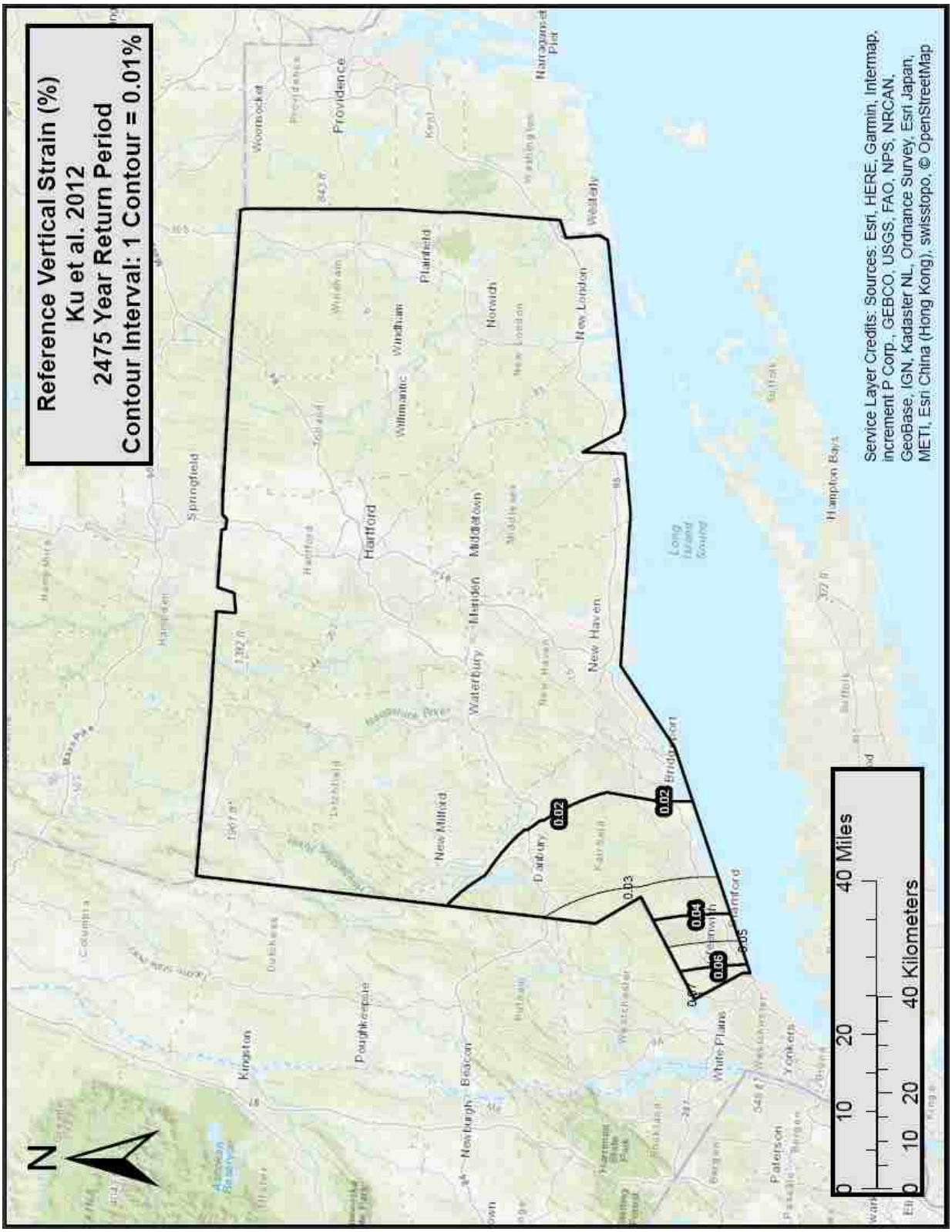

Figure A-6: Ku et al. (2012) Volumetric Strain Parameter Map for Conneticut (Tr = 2475).

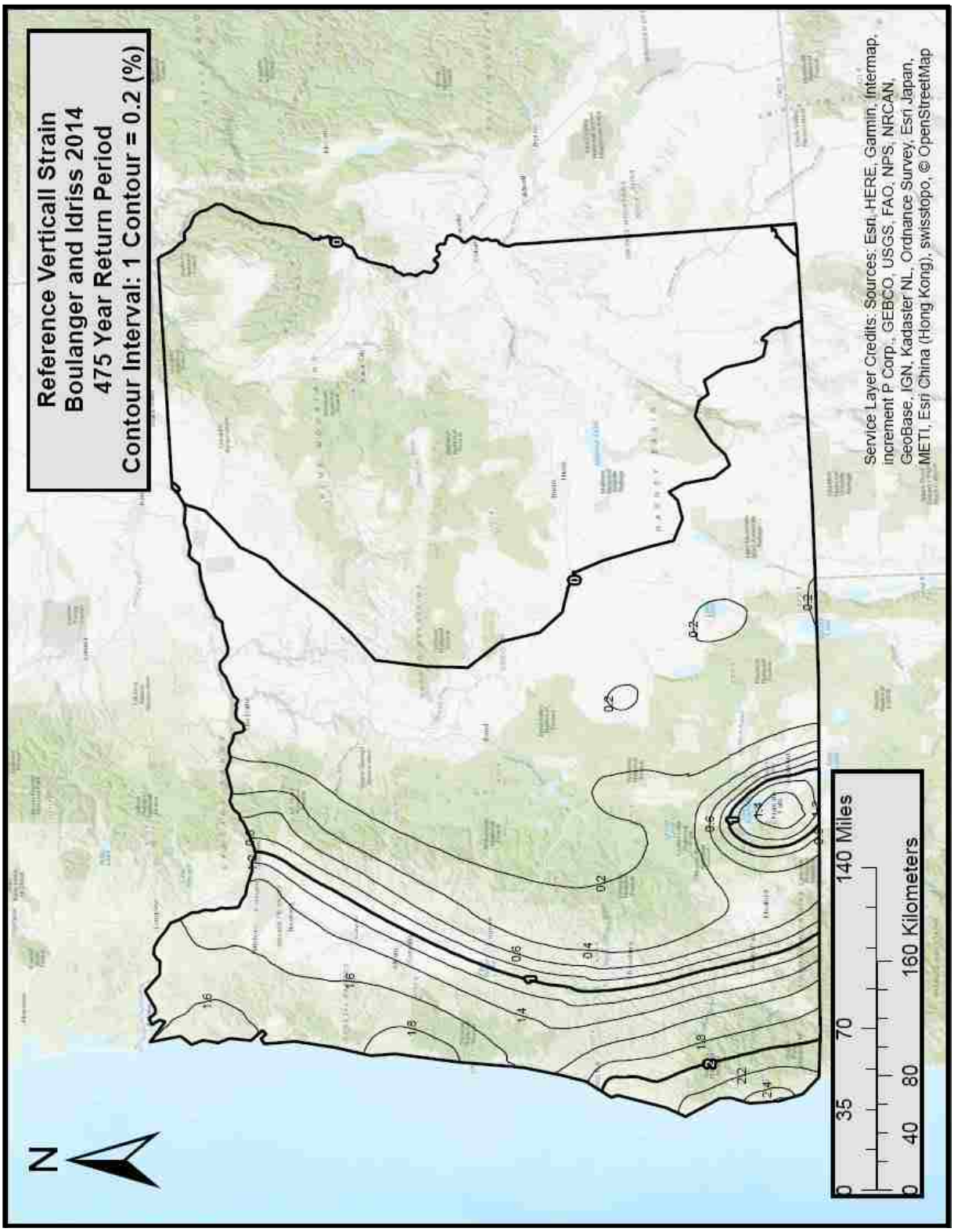

Figure A-7: Boulanger and Idriss (2014) Volumetric Strain Parameter Map for Oregon (Tr = 475).

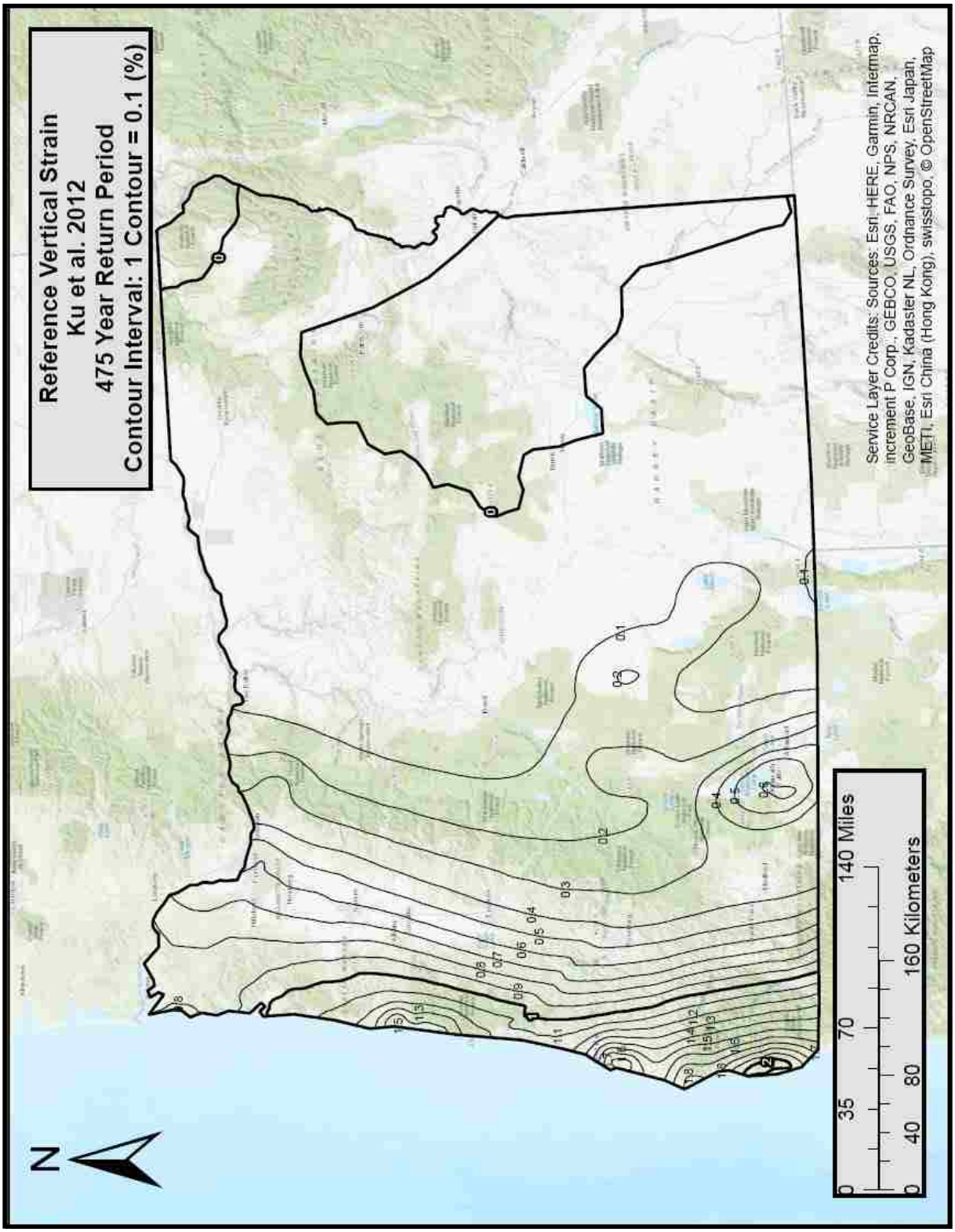

Figure A-8: Ku et al. (2012) Volumetric Strain Parameter Map for Oregon (Tr = 475).

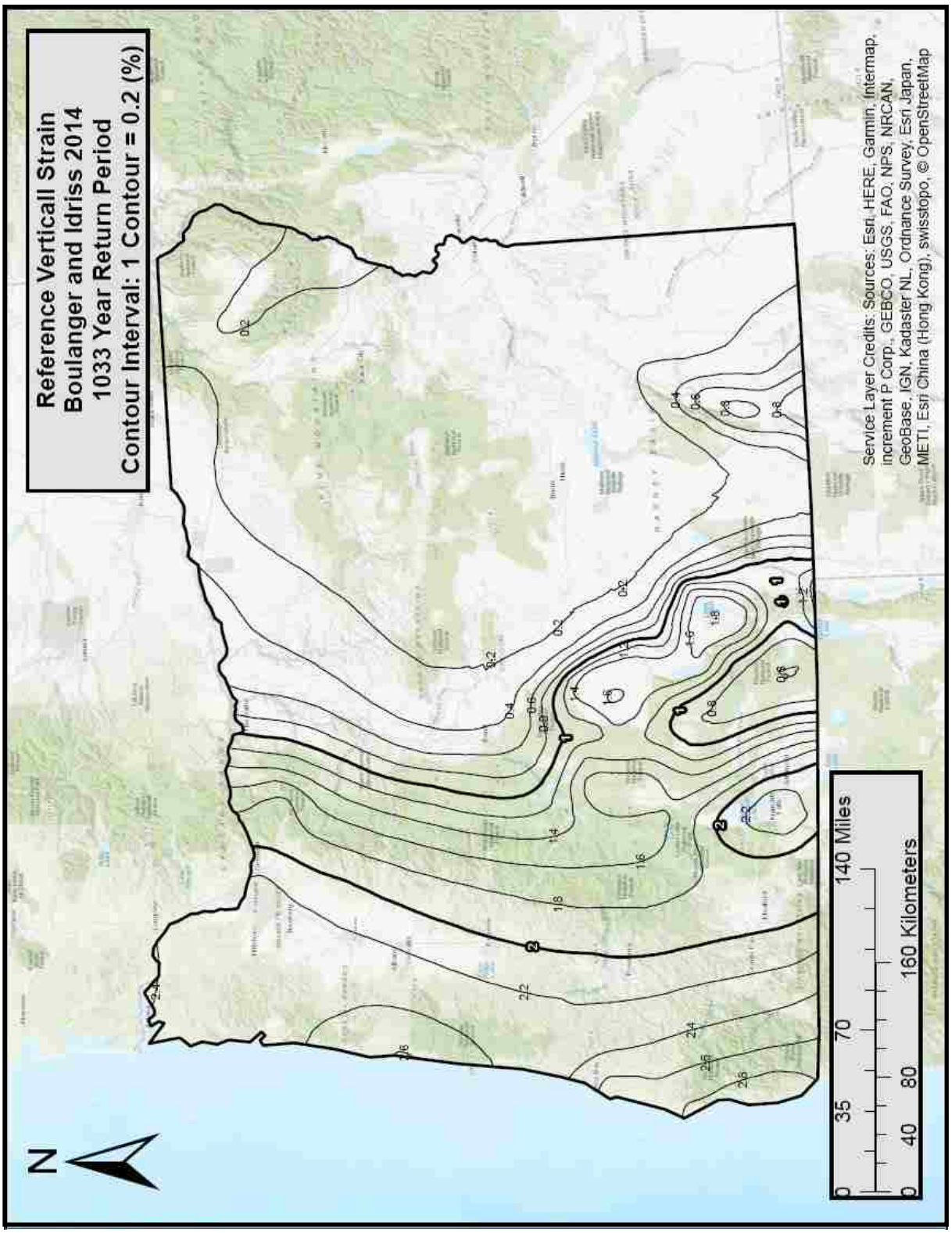

Figure A-9: Boulanger and Idriss (2014) Volumetric Strain Parameter Map for Oregon (Tr = 1033).

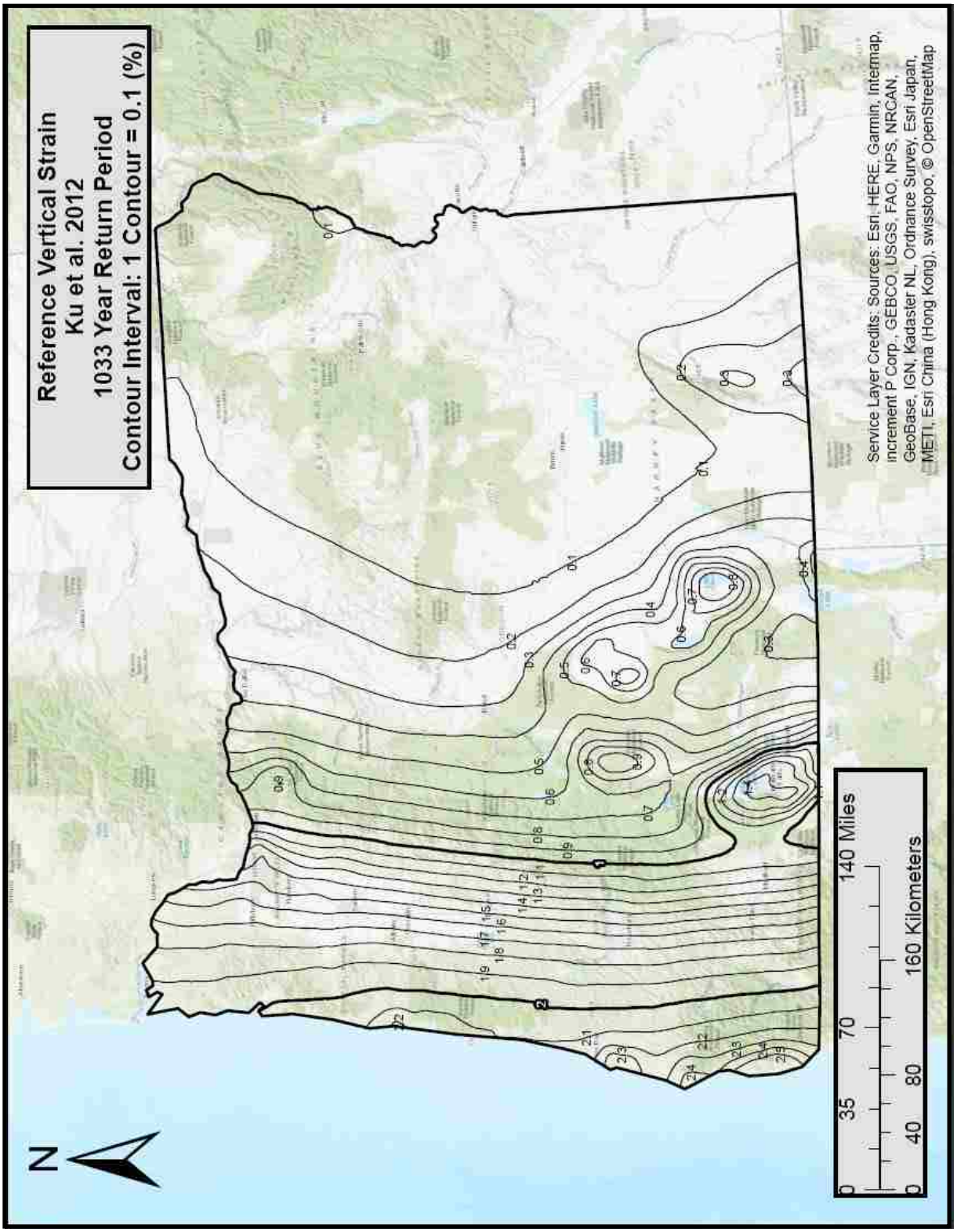

Figure A-10: Ku et al. (2012) Volumetric Strain Parameter Map for Oregon (Tr = 1033).

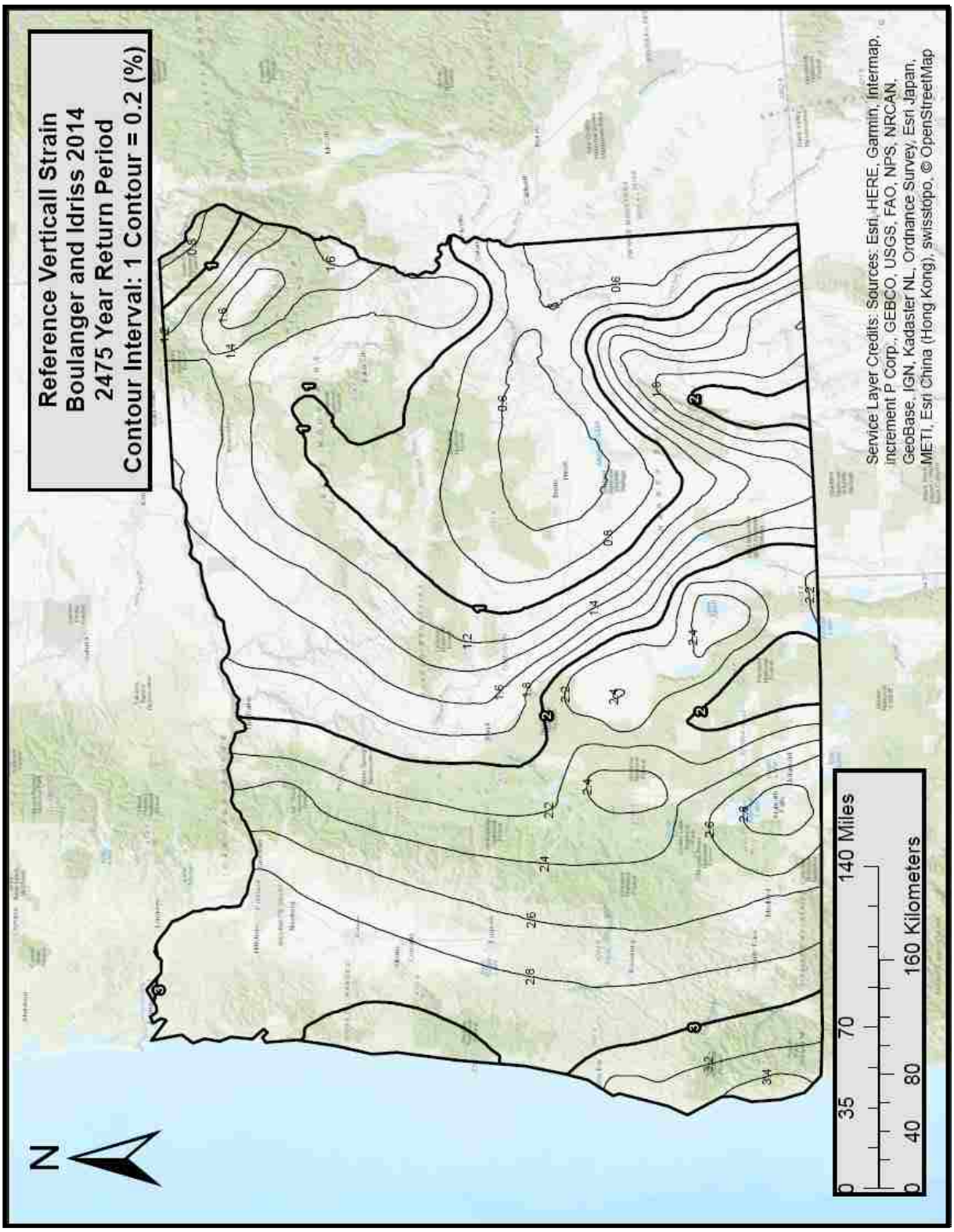

Figure A-11: Boulanger and Idriss (2014) Volumetric Strain Parameter Map for Oregon (Tr = 2475).

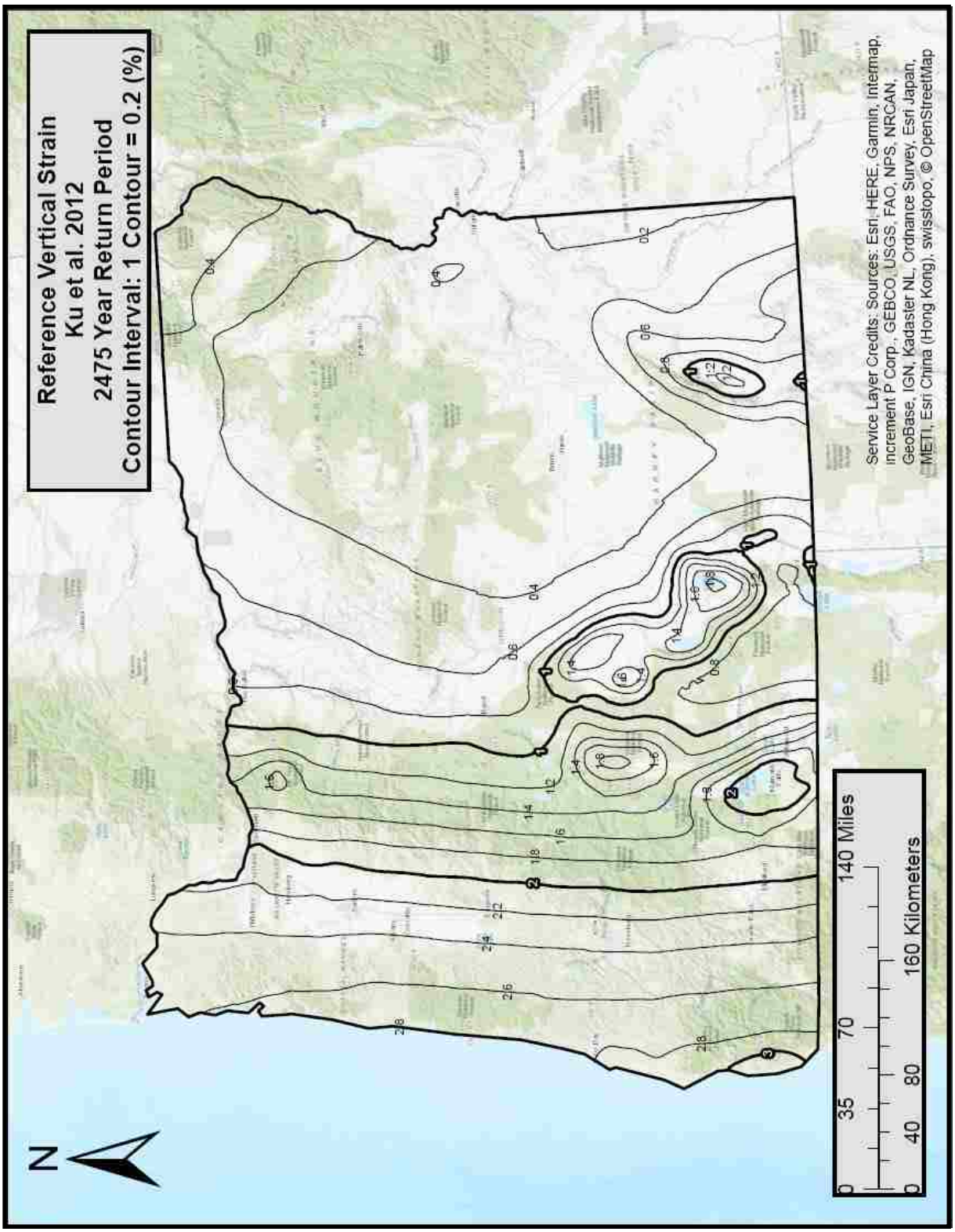

Figure A-12: Ku et al. (2012) Volumetric Strain Parameter Map for Oregon (Tr = 2475).

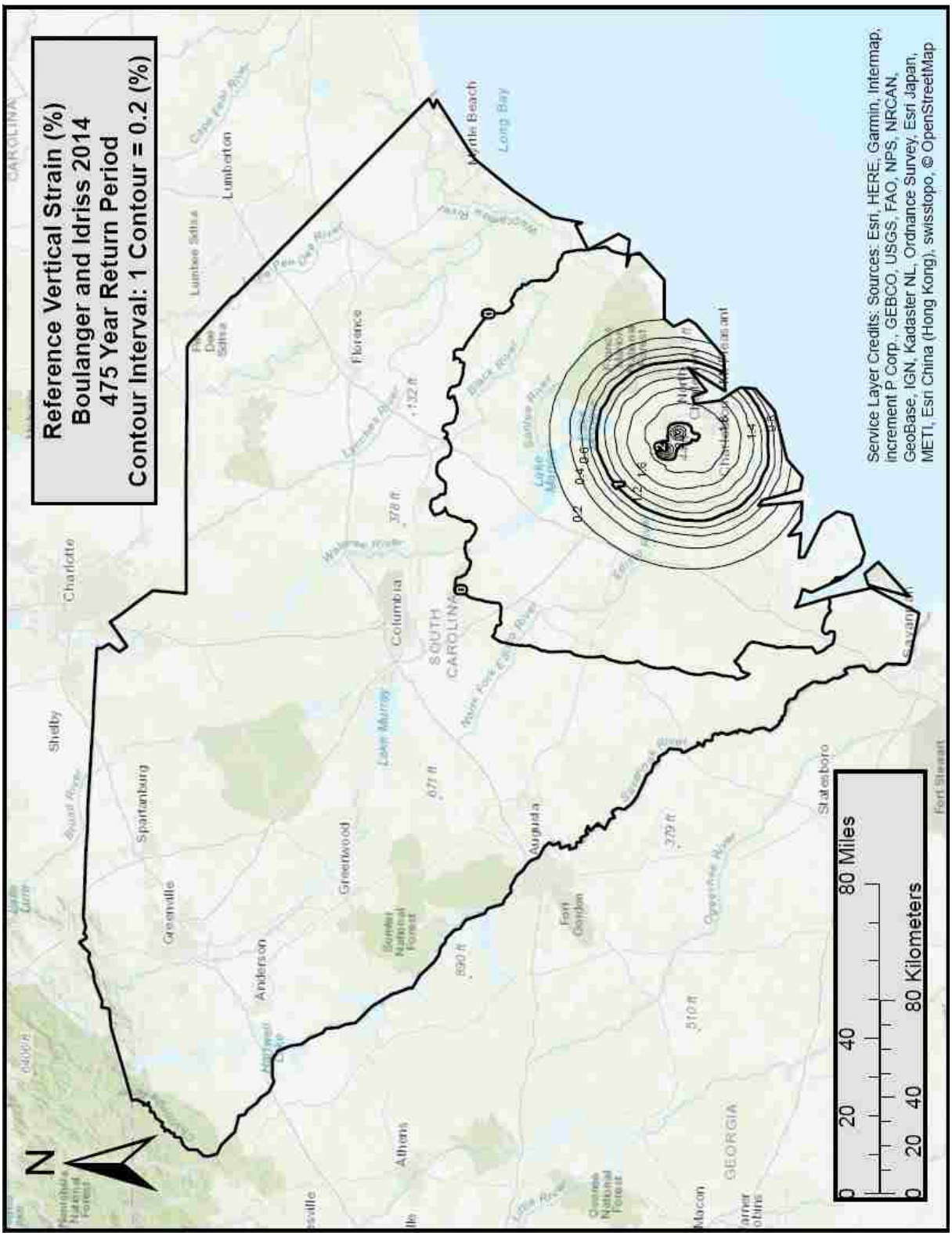

Figure A-13: Boulanger and Idriss (2014) Volumetric Strain Parameter Map for South Carolina (Tr = 475).

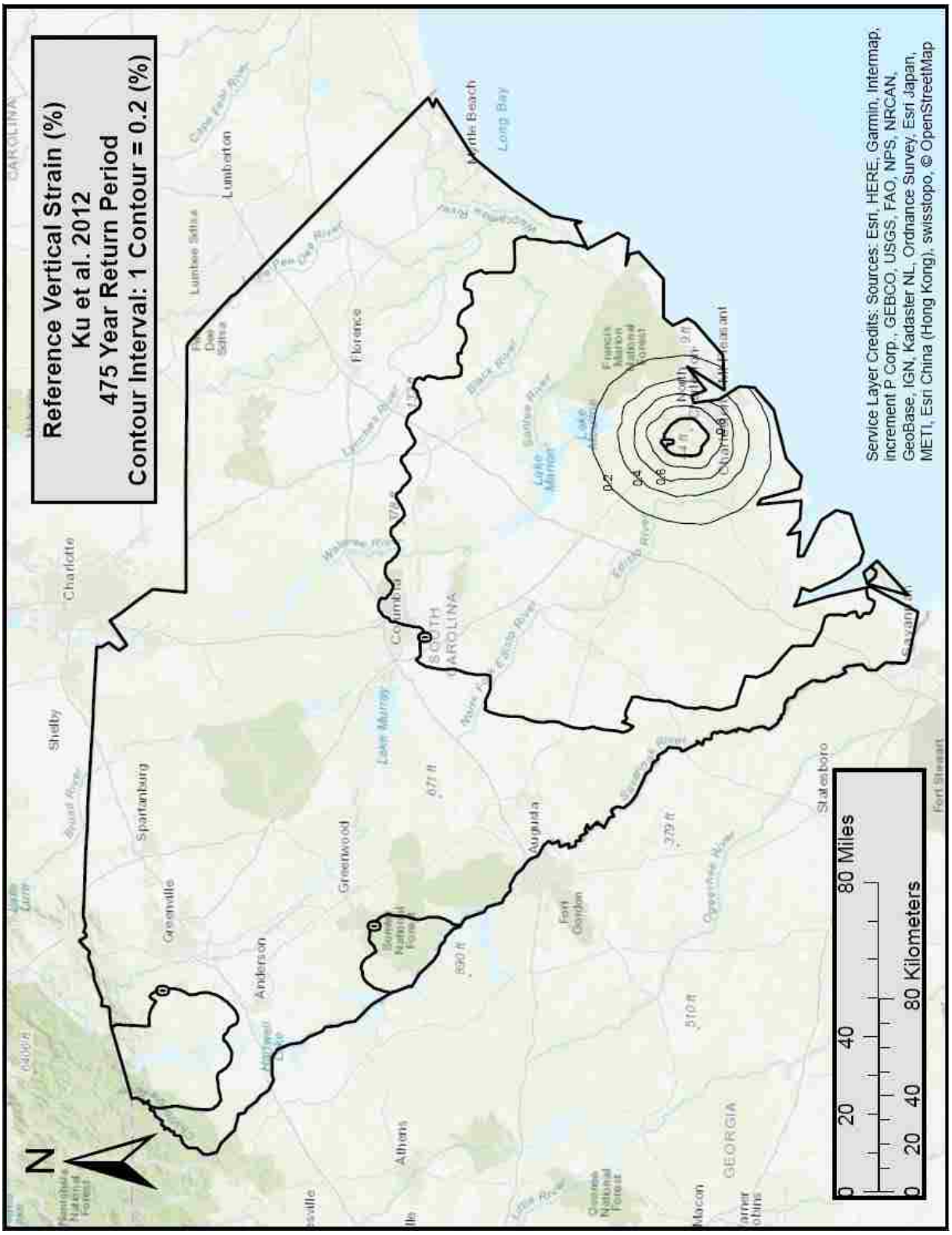

Figure A-14: Ku et al. (2012) Volumetric Strain Parameter Map for South Carolina (Tr = 475).

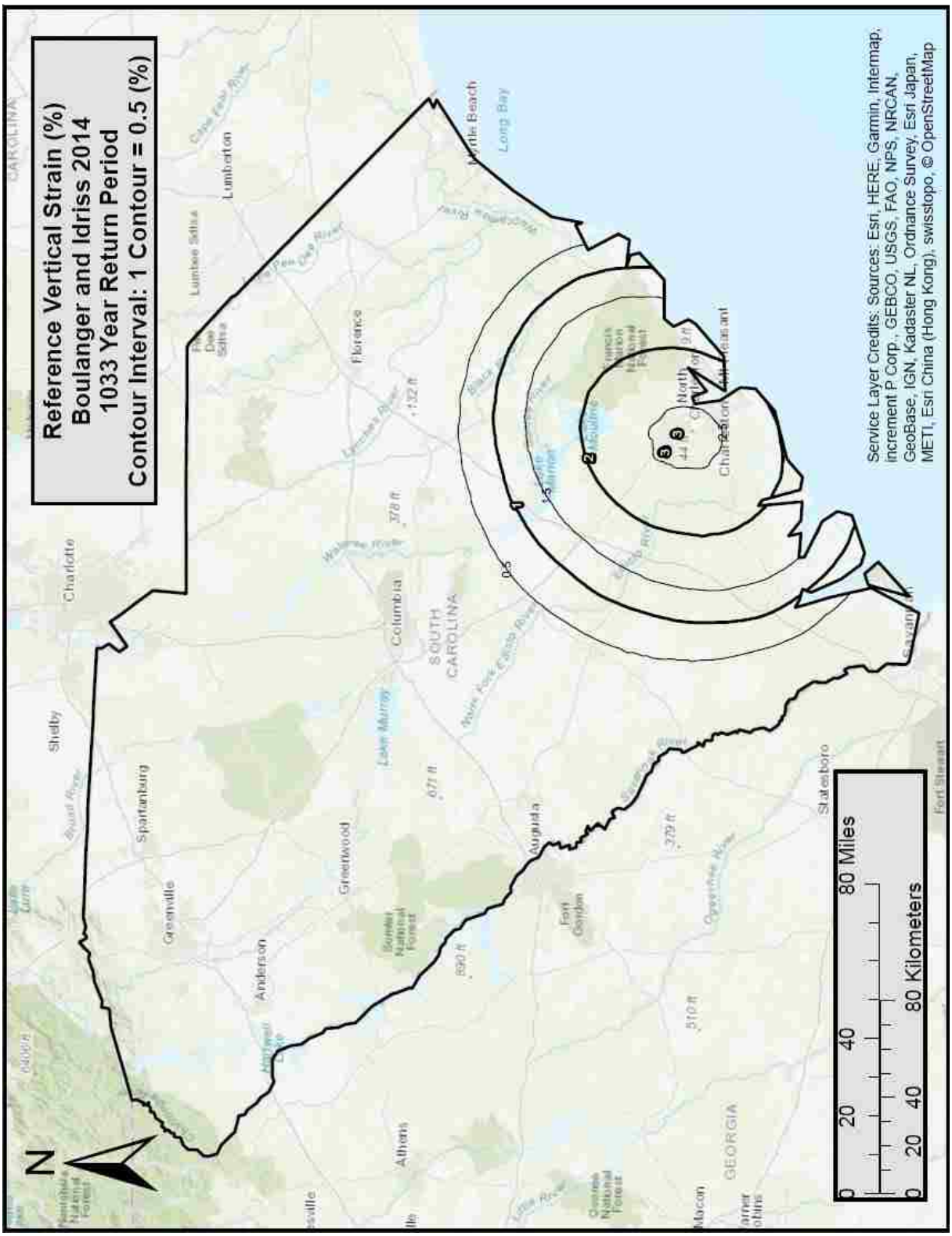

Figure A-15: Boulanger and Idriss (2014) Volumetric Strain Parameter Map for South Carolina (Tr = 1033).

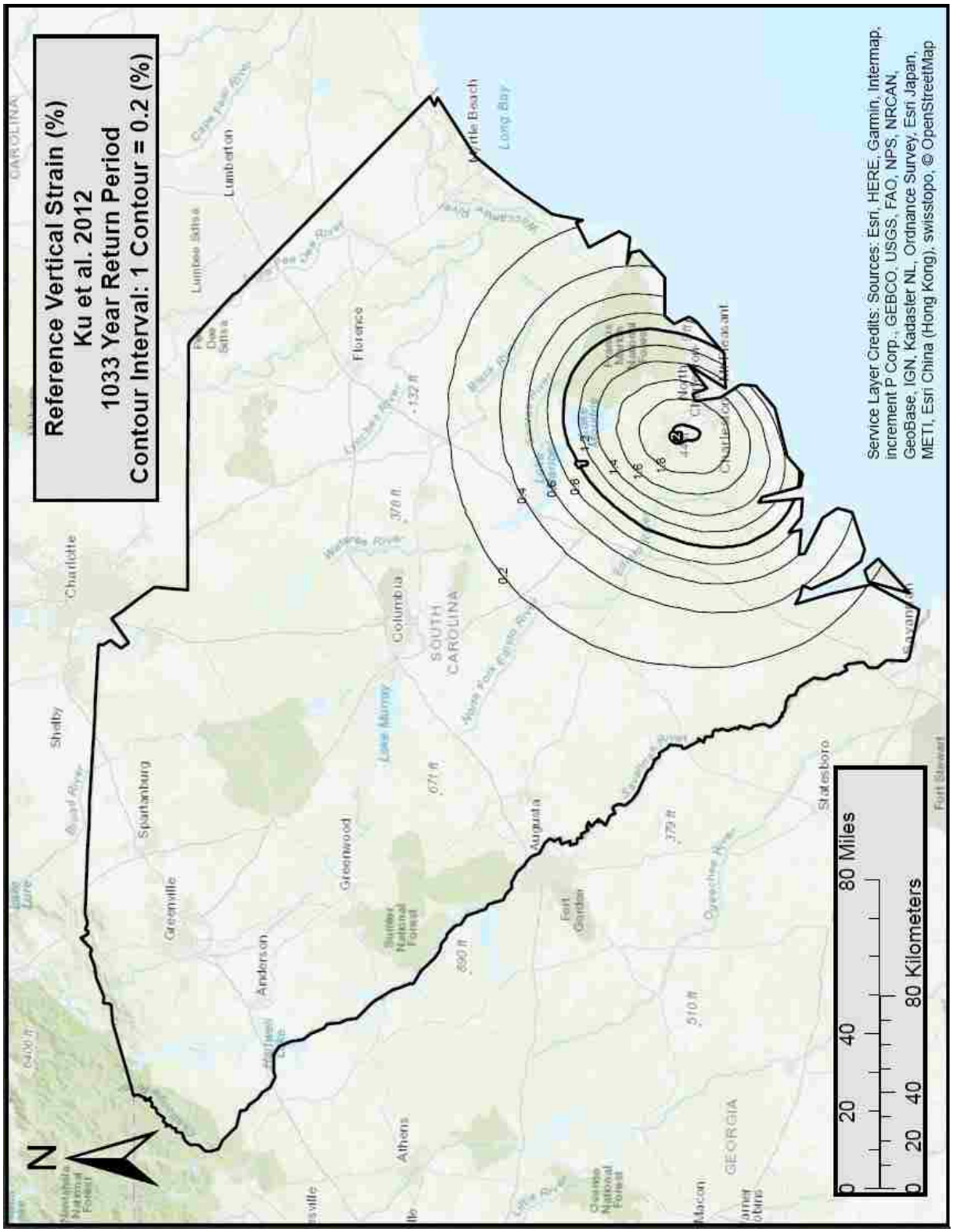

Figure A-16: Ku et al. (2012) Volumetric Strain Parameter Map for South Carolina (Tr = 1033).

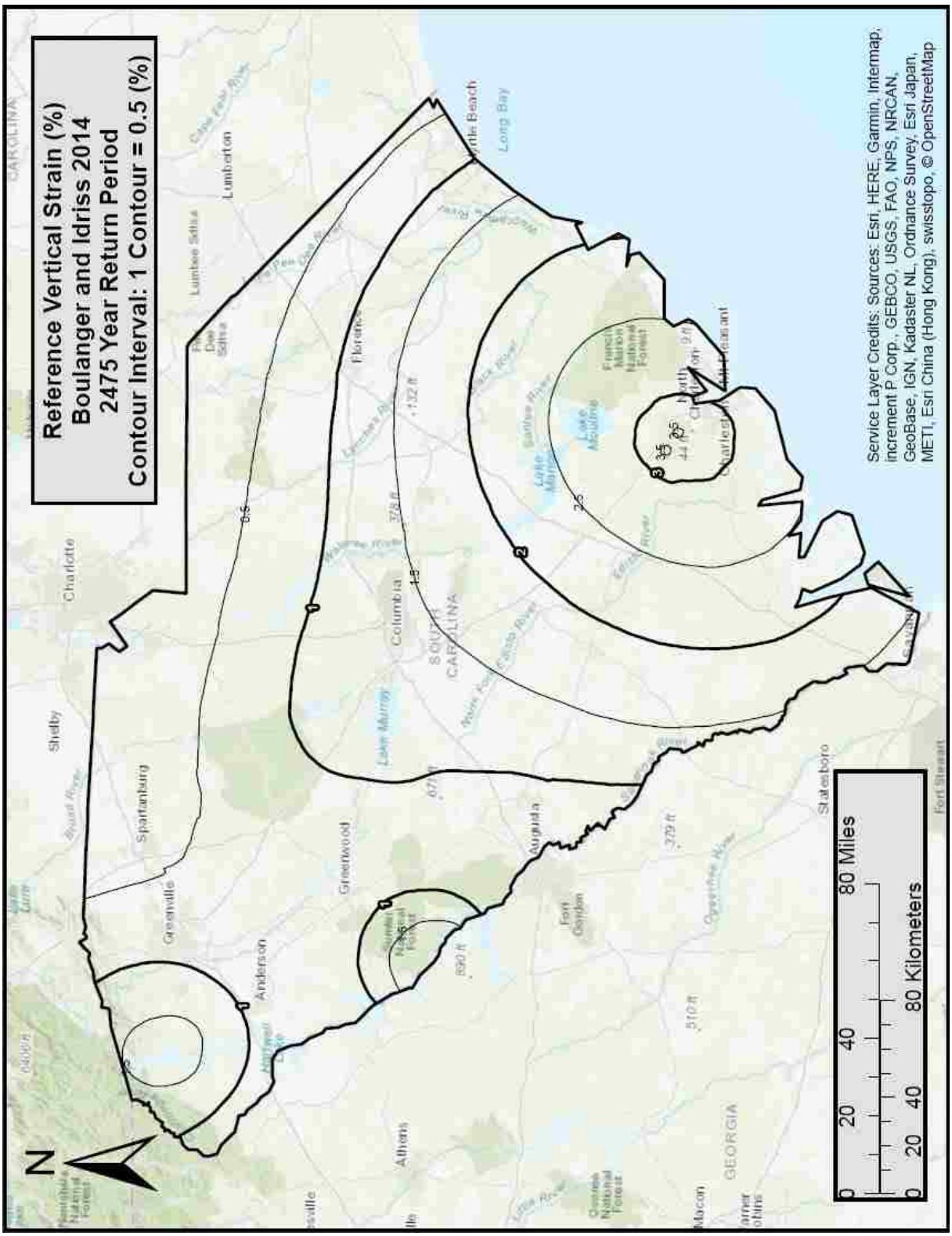

Figure A-17: Boulanger and Idriss (2014) Volumetric Strain Parameter Map for South Carolina (Tr = 2475).

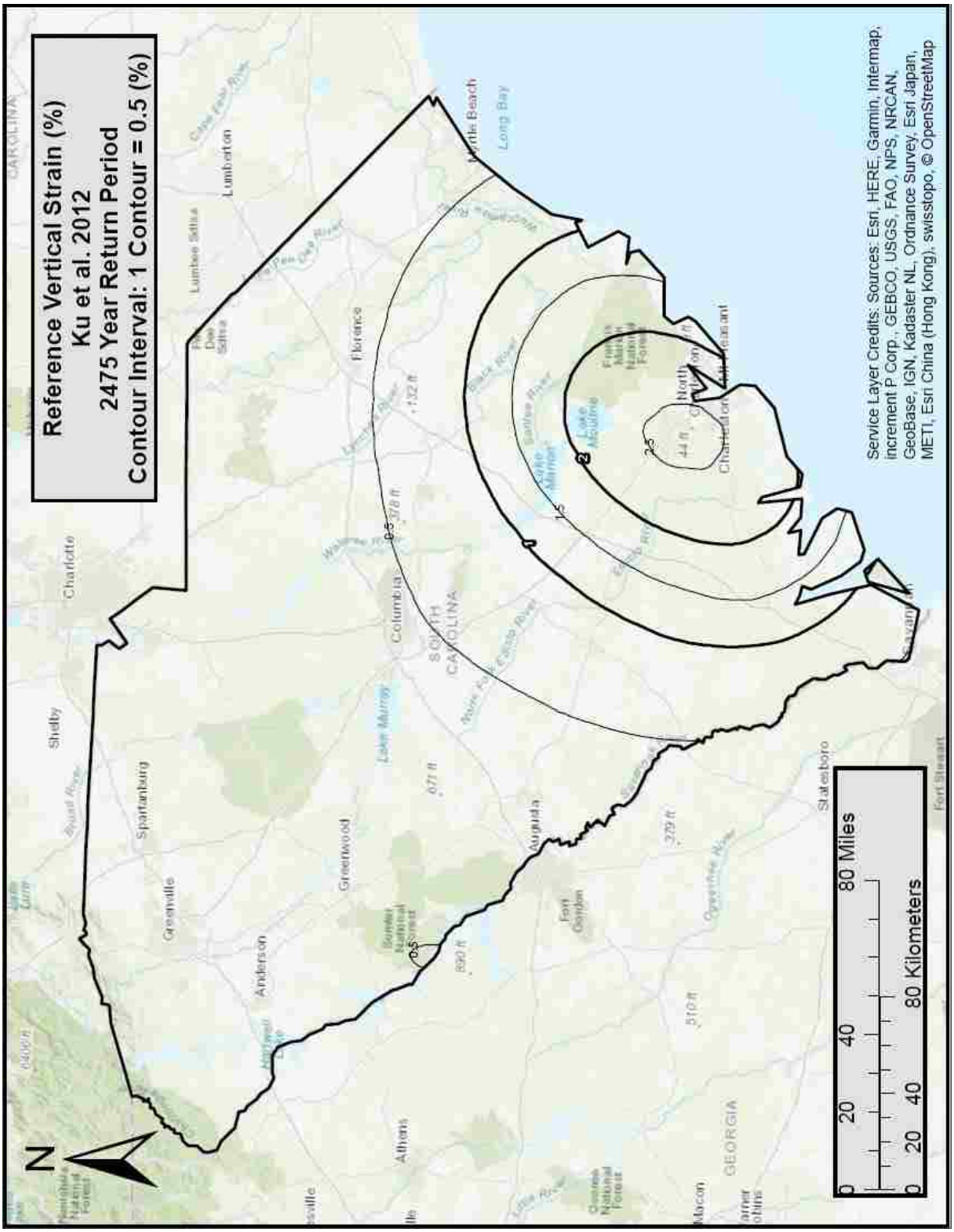

Figure A-18: Ku et al. (2012) Volumetric Strain Parameter Map for South Carolina (Tr = 2475).

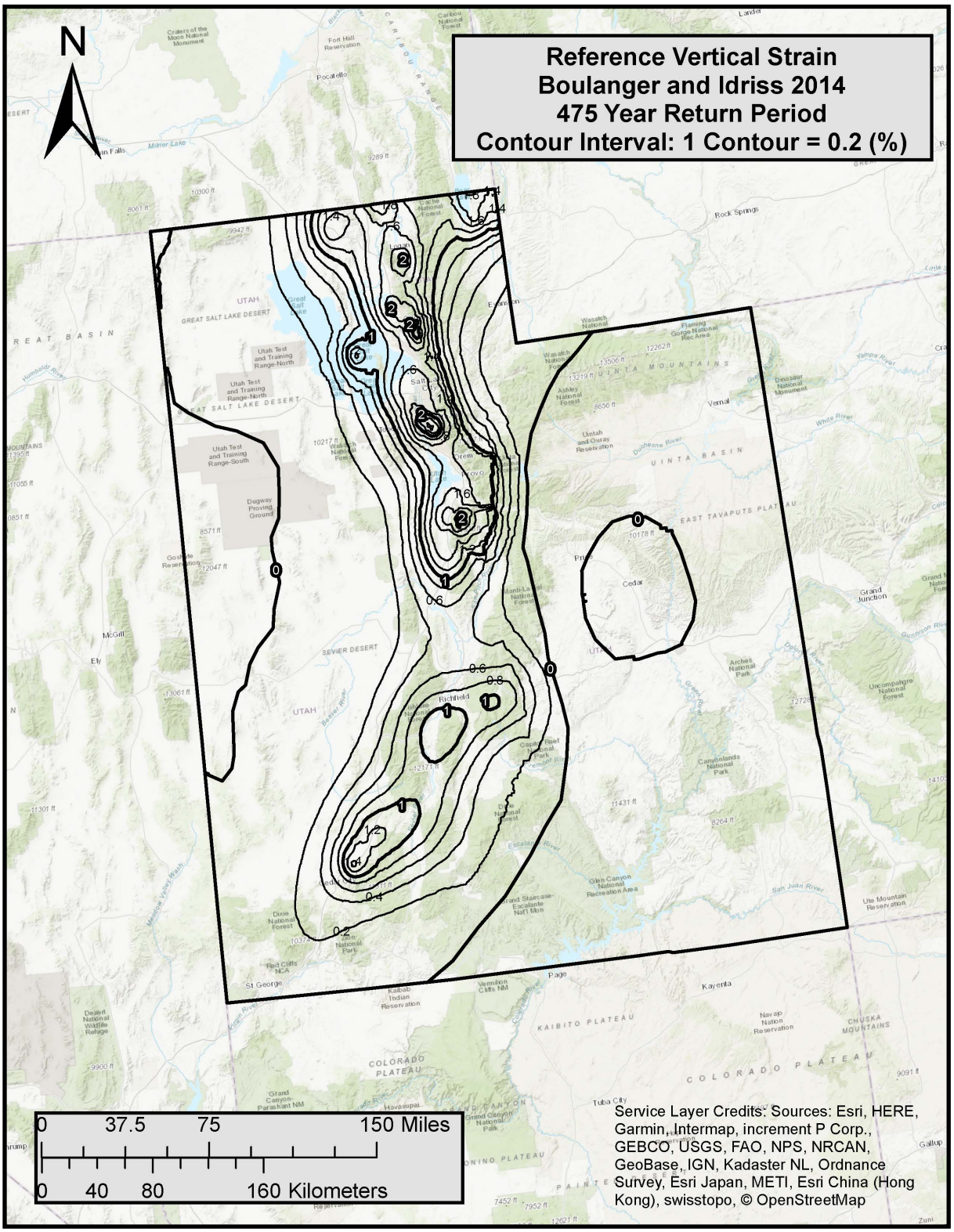

Figure A-19: Boulanger and Idriss (2014) Volumetric Strain Parameter Map for Utah (Tr = 475).

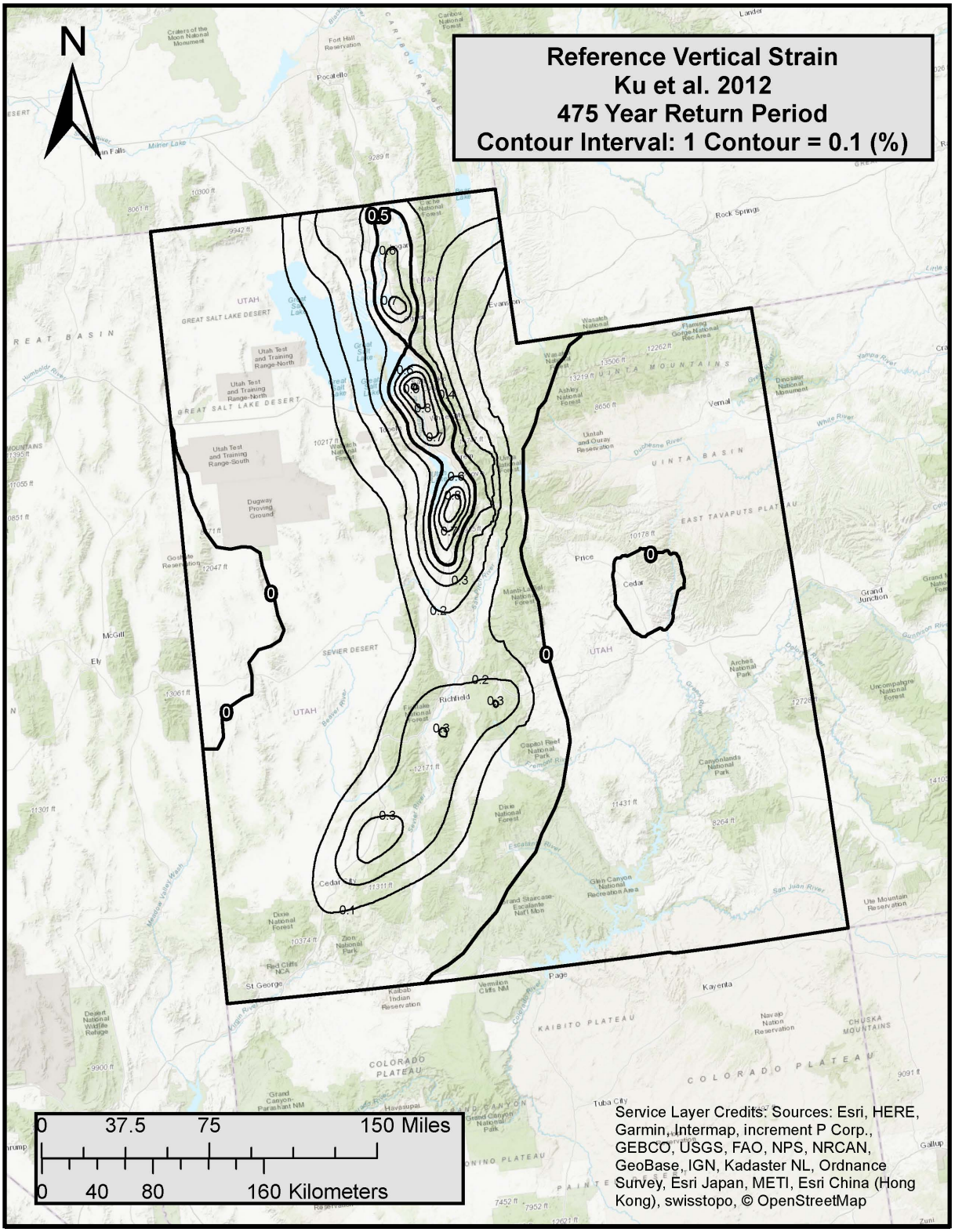

Figure A-20: Ku et al. (2012) Volumetric Strain Parameter Map for Utah (Tr = 475).

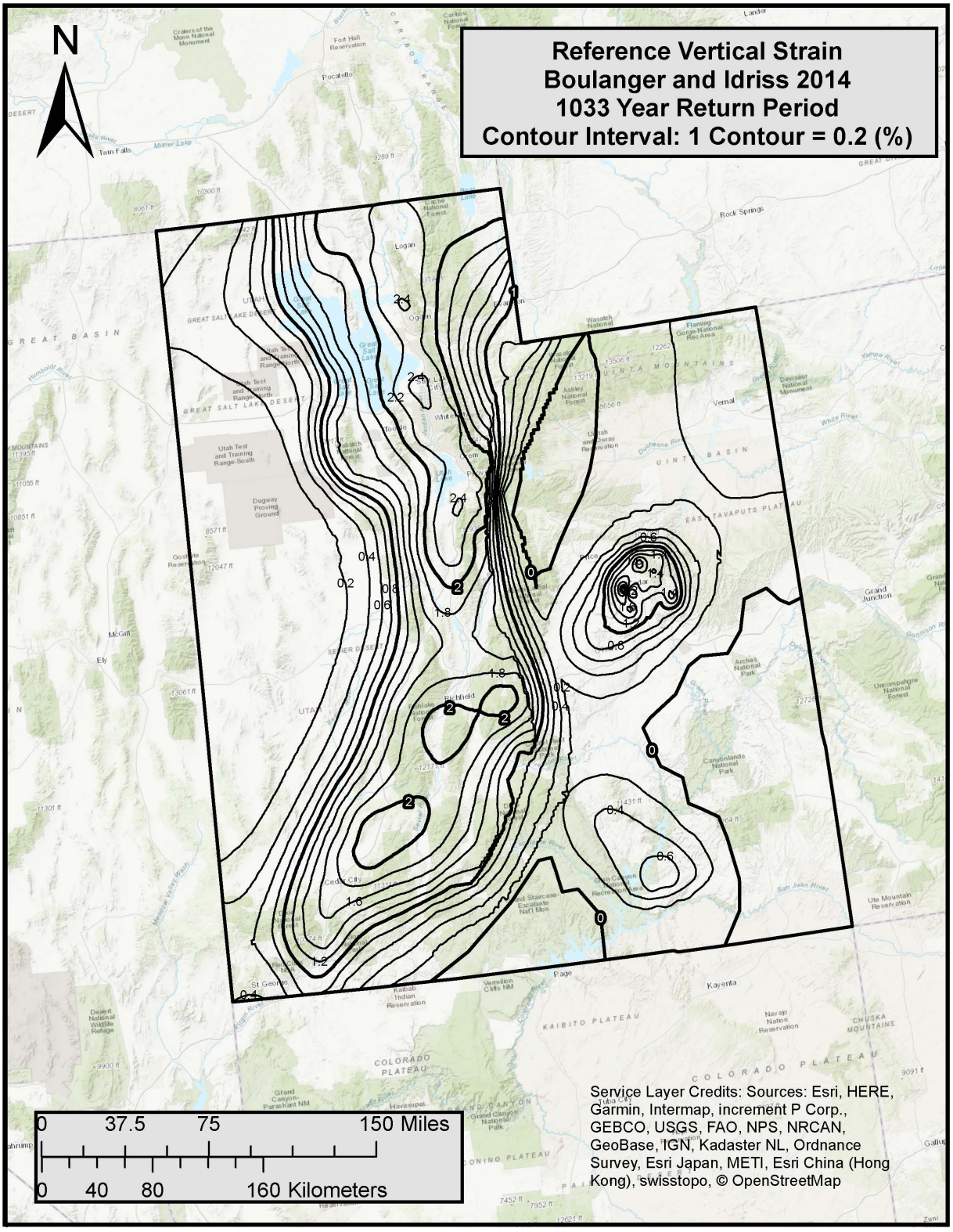

Figure A-21: Boulanger and Idriss (2014) Volumetric Strain Parameter Map for Utah (Tr = 1033).

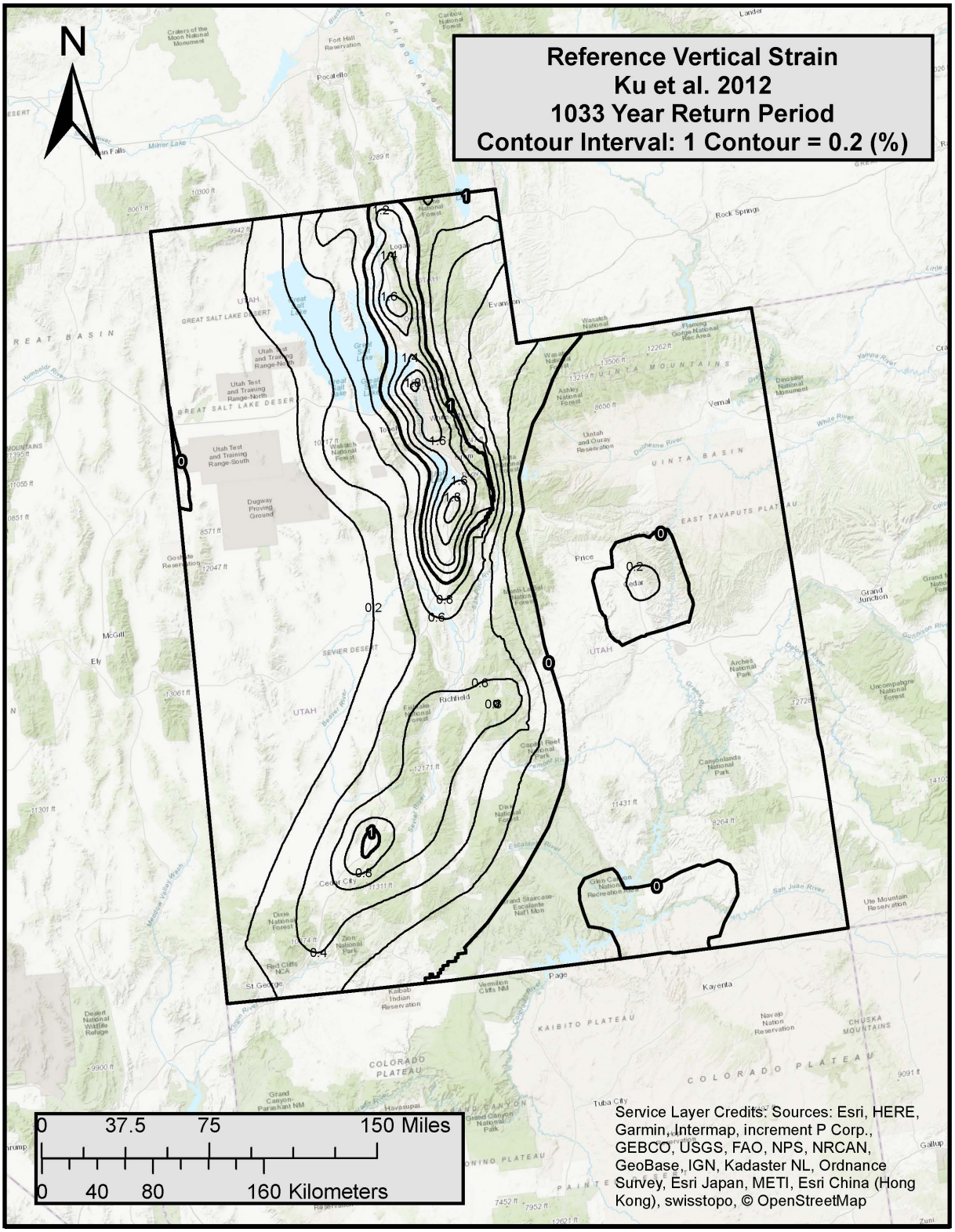

Figure A-22: Ku et al. (2012) Volumetric Strain Parameter Map for Utah (Tr = 1033).

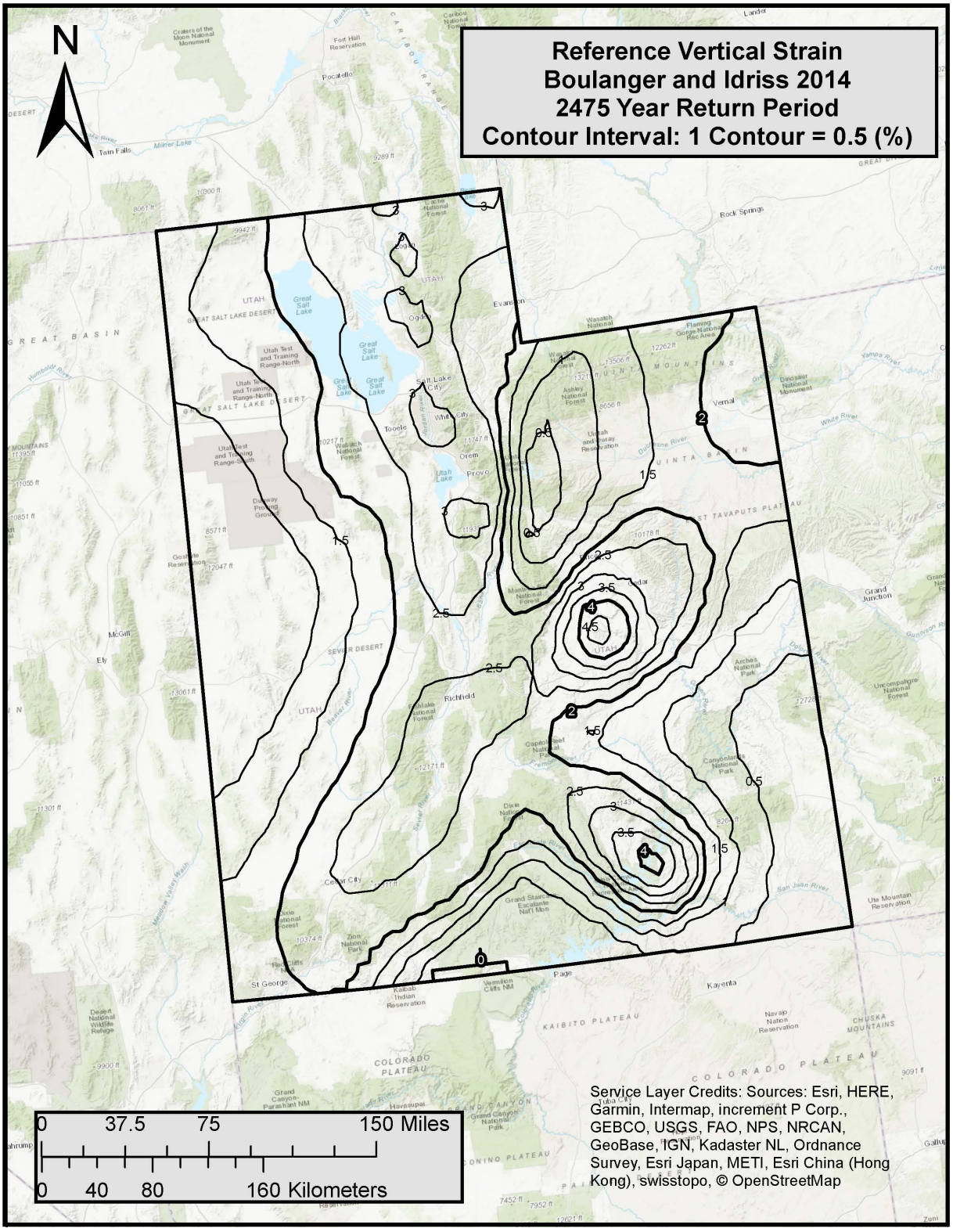

Figure A-23: Boulanger and Idriss (2014) Volumetric Strain Parameter Map for Utah (Tr = 2475).

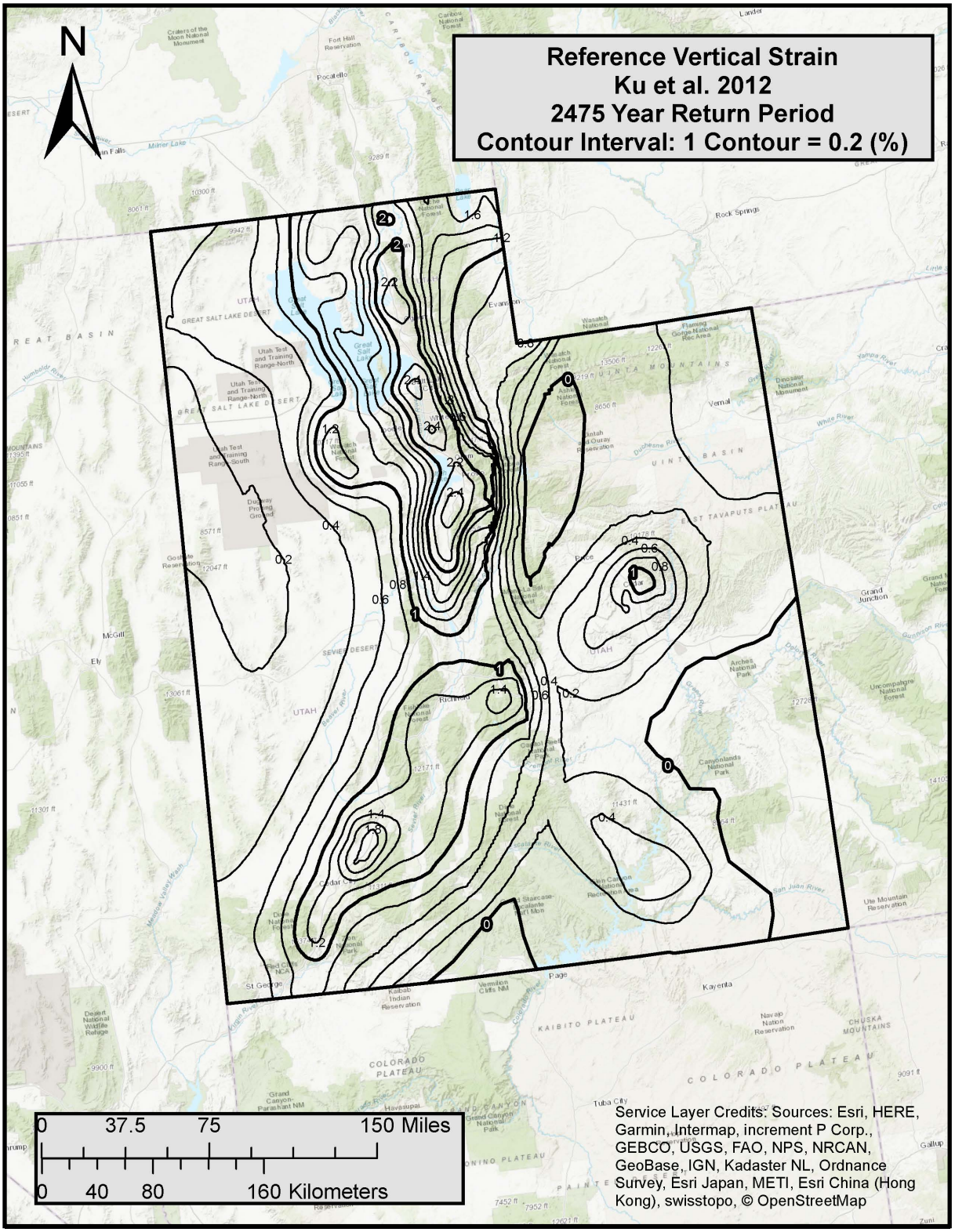

Figure A-24: Ku et al. (2012) Volumetric Strain Parameter Map for Utah (Tr = 2475).